FLORIDA STATE UNIVERSITY

COLLEGE OF ARTS AND SCIENCES

THE ROLE OF SEMICONDUCTING ELECTRONIC STRUCTURE ON STATIC AND TRANSIENT PLASMONIC PROPERTIES

By

JASON ERIC KUSZYNSKI

A Dissertation submitted to the
Department of Chemistry and Biochemistry
in partial fulfillment of the
requirements for the degree of
Doctor of Philosophy

2024

Jason Eric Kuszynski defended this dissertation on March 25, 2024.
The members of the supervisory committee were:

Geoffrey Strouse

Professor Directing Dissertation

Peng Xiong

University Representative

Lea Nienhaus

Committee Member

Kenneth Hanson

Committee Member

The Graduate School has verified and approved the above-named committee members, and certifies that the dissertation has been approved in accordance with university requirements.

This one goes out to the the 1987 Spectra-Physics Quanta-Ray DCR-3 Pulsed Nd:YAG laser. Thanks for lighting up my life.

...and to my mom of course. For many reasons (some obvious), I would not be here without her.

*"F***ing lasers, man."*

ACKNOWLEDGMENTS

I wouldn't have been able to make it to where I am today without support from the very beginning. So, naturally, I acknowledge those in my life who have been fundamental drivers to me pushing onwards and making it to one of the highest levels of education in the world. A remarkably special thanks to **Mom**, whose thoughtfulness, compassion, generosity, and stalwart person-hood supported me unconditionally throughout my life. I quite literally would not be here without her. I love you lots and owe you more than I could ever repay.

A special thank you to **Dr. Pampa Dutta**, who first got me excited about chemistry and the wondrous sense stoichiometry made to me in high school. It was with you I was first exposed to hosting a laboratory experiment and teaching my peers with a remarkable potassium dichromate experiment. I'll seriously never forget the memories made that day with you and the AP Chemistry class.

For my "pre-grad school" experience as an undergraduate at Texas A&M, a tremendous thank you to **Dr. Simon North** for accepting me into his group as a floundering freshman ever since his fantastic Chem 101 class— *"Straightforward, right?"* Without a lick of physical chemistry under my belt, I learned the skills and knowledge necessary to be successful not only as a future graduate student but also towards being a holistic, independent thinker. Your mentorship and group were profound on my decision to pursue grad school, and you truly modeled the group dynamic that I can only hope to mimic should I ever find myself running a research group of my own one day. To **Dr. Niclas "Nic" West**, I thank you for being an excellent mentor for my entrance into the world of spectroscopy, SolidWorks, and LabVIEW, as well as our shared love for Jin's Asian Cafe. I always fondly recall the late lab hours we would spend together whenever instrumentation started working in the basement lab. To **Dr. Zachary "Zach" Buen**, thank you for letting me pester and contribute to all things wind tunnel related, despite *starting the fire...* You are quite possibly the funniest person I have ever met, and you were a role model for how a senior grad student should be. To me, you are very much the older brother I never had. **Madeline "Maddie" Smotzer**, thank you for being a tremendous friend. I felt like we could talk about anything and everything, and it was always fun hanging out or doing science together. Our conversations together were so influential in helping me figure out what type of person I want to be as I continue growing up.

Thank you **Nicholas "Nic" Shuber** and **Dr. Megan Aardema** for all the wonderful boba tea walk n' talks and beach trip we all took together before I left for Tallahassee. You guys are the best. An overarching thanks to North Group alumni **Dr. Joshua Winner**, **Dr. Colin Wallace**, and **Dr. Carolyn Gunthardt**. I'm so thankful for all the support, group meetings, and group lunches we've shared. It was such a pleasure to get to know and grow alongside you all.

Thank you to **Dr. Andreas Ehnbom** from the Gladysz and Hall groups who introduced me to the world of computational chemistry. You have served as a guide for me in professional development in so many ways, and I've always appreciated the perspectives you've had to offer and our fruitful conversations.

A remarkable thank you to **Captain, Dr. Hannah Drake** from the Zhou Group. The conversations we have had over tea are like tea for the soul. I will always cherish our time together, in the past, present, and future. I'll be a captain too, soon enough!

To my best friend and future M.D., **Alexis Harris**, who has been my lab spouse from junior year of undergrad onwards, thank you. Thank you for putting up with me and keeping in touch despite my aloofness. Without you, I may have simply gone insane. With you, at least we can be insane together.

To my brother from another mother, **Noah Boyd**, thank you. You truly brought me out of my shell unlike anyone else. I love you and the crazy adventures we've had together. I know we'll always have each other's back no matter what happens.

Thank you to **Nick Chiriboga** for sticking with me through thick and thin. It's been a wild journey. I appreciate the fact we can always pick things up like we never left them. I love you man.

Thank you to **Alex Terry** for being the best dive partner for life and crazy enough to skydive with me. There's no one I'd rather be 60 ft under than with you.

To one of the best organizations I've ever known and been lucky to be a part of, the Texas A&M Student Counseling HelpLine. Thank you, **Susan Vavra**, for being my second mother. You are a force to be reckoned with, and I aspire to be like you every day. Thank you, **Amy Prescott**, for being the realest friend I could ask for through thick and thin. You've been instrumental in my journey of self-discovery, and I thank you for helping me grow as my bisexual self. Thank you, **Kaitlin Mooney**, for the eternally wise and deep conversations we always seem to strike ourselves into no matter how long it's been. To **Catherine "Cat" Kuykendall**, thank you for all the

wonderful drinks and laughs we've had together. I feel like we can talk about literally anything and always support each other. To the whole chosen family I made while working the line: **Nicole Chu**, **Vinicius "Vini" Goecks**, **Alexandra McCammon**, **Josh Philip**, **Helen Sanchez**, **Lauren Slusher**, **Sydney Stevens**, and so many others, I love you all oh so very much. There aren't enough words to describe how much I love and care for you all.

For the mentors and friends I've met at AFRL in Albuquerque, NM. Thank you, **Dr. Greg Pitz**, for trusting in me and being a fantastic mentor for both of my summers there. I can't go without my Christmas chilies because of you. Thank you to **2d Lt. Quincy Zawadzky** for the Arctic Circle bonding and wonderful conversations we had over life, society, and how horrible everything is. You're going to go on to do great things soon. Thank you to **Stephen Shock** for just being an awesome friend and mentor while giving me a taste of what LabVIEW godhood looks like. Thank you for **Daniel "Dan" Parra** for the shared *Pollito con Papas*, the *God bless*'es, and the fun we had together. A gracious thank you to **Dr. David "Tony" Hostutler**, **Landon Schmuker**, **Donald "Don" Stalknaker**, and for all just being fantastic people and an absolute pleasure to work with. Seriously–I miss you guys.

Thank you to members and recent alumni of the Strouse Group. You've all held special places in my heart. To **Dr. Carl Conti III**, for challenging me to be better, introducing me to Airplane, and helping me answer *the* age-old question. To **Dr. Edward "Eddie" Nguyen**, for the reassurance that things get better and the mutual rant sessions we had together. To **Raul Ortega**, for making me laugh the most, helping me with all my synthesis woes, and being the truest of all kings. To **Isabella "Bella" Bertini**, for being my friend through thick and thin, helping me with dumb questions, and putting up with me as a four-year roommate. To **Catherine "Cat" Fabiano**, for being an incredibly bright, awesome mentee and friend, and for sharing departmental tea with me. To **Sarah Bennett**, for her unwavering excitement in the lab, generosity, and determination to push through. To **Emily "Emi" Cook** and **Ali Pazoki** for being awesome first years–I'm excited to see what you both do next. To the undergrads I've had the pleasure of mentoring or knowing: **Jonathan Rider**, **Alex Trbovic**, **Anoushka Ahuja**, **Jason King**, and **Samantha Bell**.

Thank you to those in the Chemistry & Biochemistry department who I couldn't be without. To **Brianna "Coia" Coia**, for the mutual struggles and growing up from wee first years to grumpy senior students. I'll always appreciate your cheese etiquette and sparging techniques. You've

unironically kept me grounded in so many ways. To **Erica Knorr**, for all the wonderful crying and laughing moments we've shared. There's no one better to watch pining shows with. Oh, and thank you for our mutual love of memes of course. To **Zachary "Zach" Barton**, **Hayley Drozdick**, **James "Dirty Jimmy" Kimball**, **Courtney Leo**, **Grace "Gracie" Macleod**, **Nadia "Zana" Singleton**, **Colette Sullivan**, and too many others to keep listing–I always love hanging with you guys.

Over at the MagLab, a sincere thank you to **Dr. Stephen "Steve" McGill**. You've taught me practically everything I know about voltage, current, and instrumental electronics which has been so useful for troubleshooting and understanding home-built spectroscopy systems. I've always enjoyed our conversations during magnet cooldowns and truly appreciate the endless insights and stories you have at your disposal.

Thank you to the **baristas** of Lucky Goat and **cold brew**. Their cold brew is unparalleled and I will continue to survive through life with their bean flavors no matter where I go.

Thank you to my committee members. **Dr. Lea Nienhaus**, you are incredibly intelligent and I always learn something new from you. I admire your productivity and your ability to push forward no matter how tough the going gets. It's been a pleasure collaborating over the years. **Dr. Kenneth "Ken" Hanson**, I've always appreciated your candor when it comes to speaking with graduate students. You inspire me to do the same and to strive to give really, really good scientific presentations as you do. **Dr. Peng Xiong**, I appreciate your ability to ask simple, direct questions during the physics group meetings we had. You were always straight to the point. I admire that and hope I can adopt some of that attitude in my scientific career moving forward.

Although not presently on my committee, I also thank **Dr. Hanwei Gao** for serving on my committee up until December 2023. It is unfortunate that you were in the UK during Spring, but I sincerely always appreciated your questions and desire to learn more about my research, especially in my early PhD years. I'm very glad you were a part of my growth as a scientist.

Last, but certainly not least, a special thanks to my graduate advisor, **Dr. Geoffrey "Geoff" Strouse**. It's certainly been a journey. Thank you for your insights and genuine desire to do not good science, but great science. I still remember the recruitment talk you gave to my cohort when I was a first-year. You have a passion for science that I think mirrors my own, and it's always fun to get excited about cool, new science together.

If I have missed a crucial or pivotal person in the journey to obtain this degree, please know you are not forgotten. In fact, please feel free to fill in the following as you see fit:

Thank you to _____ *for all of your* _____*, your* _____ _____*, and your* _____ _____ _____*. I've always appreciated your* _____*. You truly were the* _____ *of all time.*

I hold no apologies for the length of these acknowledgments, and I thank *you*, yes, *you*, the reader, for taking the time to read them. Stay shiny kings and queens.

TABLE OF CONTENTS

LIST OF TABLES

LIST OF FIGURES

LIST OF SYMBOLS

$E_{\mathrm{g,opt}}$	optical band gap
m^*	carrier effective mass
$\mathbf{D}$	electric displacement field
$\mathbf{H}$	magnetic field magnitude
ε_0	vacuum electric permittivity, $8.854\,187\,812\,8(13) \times 10^{-12}\ \frac{s^4 \cdot A^2}{m^3 \cdot kg}$
$\mathbf{E}$	electric field magnitude
$\mathbf{P}$	polarization density
q	electric charge
r	nanocrystal radius
$\vec{\mu}$	dipole moment
χ_e	electric susceptibility
ε	molar absorptivity or extinction coefficient
e	elementary charge, $1.602\,176\,634 \times 10^{-19}\ C$
ε_1	real component of the dielectric function
ε_2	imaginary component of the dielectric function
n_{r}	refractive index
k_{e}	extinction coefficient
C_{abs}	absorption cross section
C_{ext}	extinction cross section
C_{sca}	scattering cross section
ω_{p}	plasma frequency
n	carrier density
m_{e}	electron invariant mass, $9.109\,383\,701\,5(28) \times 10^{-31}\ kg$
E_{F}	Fermi energy level
μ	charge carrier mobility
$\bar{\tau}$	carrier scattering constant
σ	conductivity
$\hbar$	reduced Planck constant, $6.582\,119\,569\ldots \times 10^{-16}\ eV \cdot s$
k_{B}	Boltzmann constant, $1.380\,649 \times 10^{-23}\ \frac{J}{K}$ or $8.617\,333\,262 \times 10^{-5}\ \frac{eV}{K}$
T	temperature
Γ	plasmon damping
Γ_{H}	high frequency damping constant
Γ_{L}	low frequency damping constant
Γ_{W}	crossover frequency width
Γ_{X}	crossover frequency
E_{Z}	Zeeman splitting energy

g	g-factor
μ_{B}	Bohr magneton, $5.788\,381\,806\,0(17) \times 10^{-5}\ \frac{eV}{T}$
M_{J}	rotational angular momentum quantum number
$\vec{\mathbf{B}}$	total magnetic flux vector
ΔA	differential absorption
ω_{c}	cyclotron resonance frequency
h	Planck constant, $4.135\,667\,696\ldots \times 10^{-15}\ eV \cdot Hz^{-1}$
$\mathbf{k}$	momentum wavevector
E_{g}	electronic band gap
I	intensity of transmitted light
I_0	intensity of incident light
A	absorbance
A_1	magnetic field-induced excited state splitting
B_0	magnetic field-induced zero-field excited and ground state mixing
C_0	field-induced, temperature-dependent, paramagnetic ground state splitting
ΔE	zero-field state separation magnitude
V_{AC}	alternating current voltage
V_{DC}	direct current voltage
$\mathbf{F}$	Fock matrix
$\mathbf{C}$	molecular orbital coefficient matrix
$\mathbf{S_{AO}}$	atomic orbital overlap matrix
$\mathbf{E^F}$	diagonal matrix of eigenenergies
$\mathrm{V_O}$	oxygen vacancy
G	carrier-phonon coupling constant
τ_0	carrier-phonon decay rate at zero fluence
T_{N}	Néel Temperature
M_{sat}	saturated magnetization
K_{eff}	effective magnetic anisotropy
T_{b}	blocking temperature
Γ_{abs}	absorption linewidth
B	applied magnetic field
c	the speed of light, $299\,792\,458\ \frac{m}{s}$
S	spin quantum number

ABSTRACT

The field of plasmonics as a whole is gathering widespread interest due to their wide range of applications and new technology advancements because of their enhancement of light-matter interactions. Although scientists have largely used noble metals plasmonic metals such as gold, silver, or aluminum, the growing field of plasmonic semiconductor nanocrystals (PSNCs) still require extensive research towards how the semiconducting electronic structure impacts relevant properties such as charge carrier mobility, conductivity, and near field enhancement. This work focuses on how the host nanocrystal density of states directly impacts and modifies the plasmonic properties of interest in both the static and ultrafast transient time regimes. Chapter 1 introduces the concept of plasmons starting from the simple harmonic oscillator model leading to the free electron model's critical relationship for plasmon frequency, carrier density, and carrier effective mass. From there, the concept of band theory is introduced, and the interactions of charge carrier quasiparticles with the semiconducting electronic structure are outlined and discussed. Chapter 2 introduces the intermediate band semiconductor, Cu_5FeS_4, where magnetic circular dichroism is used to analyze the carrier effective mass as a function of applied magnetic field. Chapter 3 introduces one of the highest energy PSNCs in literature to date, WO_{3-x}, where transient absorption relaxation dynamics are deconvoluted for plasmon and optical band gap excited regimes. Chapter 4 turns to Cu_xFeS_4 (x=3,5,7), where the ratio of Cu:Fe is shown to modulate the *hole-phonon* and *phonon-phonon* transient absorption relaxation rates correlated with carrier effective mass and plasmon damping frequency respectively. Overall, this thesis showcases that static plasmon properties correlate well with transient plasmonic properties, where experiments such as magnetic circular dichroism and transient absorption are effective tools for developing the correlations needed for predicting desired plasmonic properties when designing novel PSNCs for future applications.

CHAPTER 1

INTRODUCTION

Sir William Crookes is attributed as one of the first scientists to experimentally produce the fourth state of matter in 1879.[1] In his publication, Crookes recalls even further back in time to when the legendary Michael Faraday in 1816 surmised the existence of a fourth state of matter he coined, *radiant matter*. However, it was not until Irving Langmuir first introduced the word, *plasma*, to describe a system of positive ions and free electrons with net zero charge undergoing oscillation in 1928.[2] Although both of their experiments were with free electron streams in vacuum tubes, it was through the same harmonic oscillator type mechanism that David Pines in 1956 would later encounter "collective energy losses in solids" rather than the typical plasma found in traditional vacuum tube experiments.[3] Ultimately, Pines is credited as the first to define the observed quanta of plasma oscillation as a *plasmon*. 68 years later, this graduate student takes a tiny step among tens of thousands towards increasing the amount of knowledge available in the field of plasmonics and how they can be understood when localized in semiconductor nanocrystals (NCs).

This introductory chapter walks the reader from how plasmons are treated phenomenologically and mathematical to arrive at the concept of a plasmon frequency and how they behave in semiconducting nanocrystals. First, the prerequisite light-matter interactions of plasmons and atomic-electronic interactions more generally are explored starting from the electric displacement field to a collection of free carriers localized on the NC surface. Next, relevant solid-state chemistry concepts such as band theory, quasiparticle interactions, and carrier relaxation will be discussed with a focus on plasmonic semiconductor nanocrystals (PSNCs).

1.1 Light-Matter Interactions

This introduction serves as a very cursory overview of the theoretical ideas and experimental techniques discussed throughout this dissertation. The more interested reader is referred to the excellent solid-state physics textbook by Kittel[4]. Additionally, the theses of Reed[5], Chang-Ming[6], and Hartstein[7] cover much of the groundwork that the introduction of this dissertation focuses

on while literature reviews by Agrawal et al.[8], Han et al.[9], and Diroll et al.[10] very thoroughly summarize much of the recent literature of PSNCs, magnetic circular dichroism of PSNCs, and ultrafast PSNC relaxation respectively which would be useful for future graduate students embarking on similar work to be familiar with.

1.1.1 From Dipole Moments to Plasmons

To understand how electromagnetism interacts with matter, Maxwell developed a series of macroscopic equations and derived a term for the electric displacement field, **D**, and magnetic field, **H**, which fundamentally describe the interactions of electromagnetic waves with physical materials, rather than in vacuum.[11] For the scope of this introduction, we will only focus on the electric displacement field, where **D** is defined as a function of vacuum permittivity, ε_0, the electric field intensity, **E**, and polarization density, **P**:

$$\mathbf{D} \equiv \varepsilon_0 \mathbf{E} + \mathbf{P} \tag{1.1}$$

from which it is possible to generally describe the sum of electric field behaviors that can occur within a material. Chemically, we are especially concerned with **P**, as polarizability changes dramatically depending on local atomic structure, material composition, and dielectric environment. These considerations are critical when investigating phenomena of interest to chemists, such as optical, electronic, and vibrational energy transitions that may occur in a system. These considerations pave the way to aid in understanding how plasmons originate and interact with matter.

Chemistry is fundamentally driven by Coulombic (i.e. electrostatic) forces, wherein electric charges can be either positive or negative, and neighboring ions either attract or repel depending on the organization of charge. When opposite charges interact in space, we quantify the interaction in vector form by relating the magnitude of the total charge, q, with the distance between charges, r, to obtain the dipole moment, $\vec{\mu}$. To first order, it is sufficient to equate the sum of i dipole moments to the polarization density, **P**, assuming that the electric field obeys the superposition principle:

$$\mathbf{P} \equiv \vec{\mu} = \sum_i q_i \vec{r_i} \tag{1.2}$$

where **P** can be also be understood as

$$\mathbf{P} = \sum_i \varepsilon_0 \chi_{e,i} \mathbf{E} \tag{1.3}$$

the product of vacuum permittivity, ε_0, electric susceptibility, χ_e, and the electric field intensity. With the understanding that dipole moments oscillate as a function of time, we can rewrite 1.3 in terms of a Fourier transform to transform the time domain equation into a frequency space (energy) variation of the equation, where solving for

$$\mathbf{P}(t) = \sum_i \varepsilon_0 \int_{-\infty}^{t} \chi_{e,i}(t - t')\mathbf{E}(t')dt' \tag{1.4}$$

results in

$$\mathbf{P}(\omega) = \varepsilon_0 \chi_e(\omega)\mathbf{E}(\omega) \tag{1.5}$$

where susceptibility is also known to be related to a material's relative permittivity, ε, by

$$\chi_e = \varepsilon - 1 \tag{1.6}$$

In summary, the above approach provides us with a first-principle understanding of how an oscillating electric field can be understood with respect to a "bulk" dipole response. The mathematical progression leads us to an understanding of a material's relative permittivity which will be expanded upon in the next section as to how we can experimentally probe permittivity and its relation to how a plasmon appears spectroscopically

1.1.2 Plasma Oscillation

The Lorentz Oscillator Model. Physical chemistry ingrains the concept of using harmonic oscillators to model charge motion within a medium. It was Henry A. Lorentz who first proposed describing atomic and electronic interactions with the classical spring-like force model,[12] now commonly referred to as the Lorentz oscillator model. Because the derivation from a damped harmonic oscillator to plasma response by Lorentz is not widely available in any publicly available textbooks to the author's knowledge, this section walks the reader through the derivation based on the lecture notes of Dr. John Colton[13] as it relates to the topics critical to this work. Colton illustrates that as

a sinusoidally oscillating electric field is applied to a point charge, so too does the charge oscillate in response to the electric field, as dictated by Newton's Second Law,

$$F_{total} = m\ddot{x} = m\frac{d^2x}{dt^2} \tag{1.7}$$

where F_{total} is the total force, m is mass, and $\ddot{x}$ is the second derivative of position with respect to time, *i.e.* acceleration. We start with the concept of a damped oscillator, where three forces are enacting on a point charge: the displacing force (E-field), the restoring force (Nuclear point charge), and the damping force (collisional relaxation) which sum to the product of mass and acceleration:[14]

$$F_{displacing} + F_{restoring} + F_{damping} = m\ddot{x} \tag{1.8}$$

Keeping in mind the sinusoidal nature of the applied electric field and oscillator response, we can further define our forces,

$$\ddot{x} + \gamma\dot{x} + \omega_0^2 x = \frac{e\mathbf{E}}{m}\cos(-\omega t) \tag{1.9}$$

where γ is the damping coefficient, $\omega_0 = \sqrt{k/m}$ is the undamped angular frequency equal to the square root of the spring constant (k) divided my its mass (m), e is the elementary charge, $\mathbf{E}\cos -\omega t$ is the displacing electric field represented by an oscillatory cosine function, and ω is the angular frequency of the displacing electric field. Knowing in advance that the response of a point charge to an oscillatory electric field is itself an oscillation with a proportional scalar, x_0, we can guess $x = x_0\cos(-\omega t)$ as a solution for Eqn. 1.9 and replace cosines with complex notation $x_0\cos(-\omega t) \Rightarrow x_0 e^{-i\omega t}$ using Euler's formula:

$$(-i\omega)^2 x_0 e^{-i\omega t} + \gamma(-i\omega)x_0 e^{-i\omega t} + \omega_0^2 x_0 e^{-i\omega t} = \frac{e\mathbf{E}}{m}e^{-i\omega t} \tag{1.10}$$

From here, we cancel out the shared $e^{-i\omega t}$ term and simplify.

$$(-i\omega)^2 x_0 + \gamma(-i\omega)x_0 + \omega_0^2 x_0 = \frac{e\mathbf{E}}{m} \tag{1.11}$$

$$x_0(\omega_0^2 - \omega^2 - i\gamma\omega) = \frac{e\mathbf{E}}{m} \tag{1.12}$$

$$x_0 = \frac{e\mathbf{E}}{m}\frac{1}{\omega_0^2 - \omega^2 - i\gamma\omega} \tag{1.13}$$

Essentially, we have derived the term x_0 which represents the response amplitude, or distance, of point charge oscillation after an oscillating electric field interacts with, say, an electron. Because of the inclusion of an imaginary number, the solution is phase dependent, meaning there is some phase offset between the interaction of the applied electric field and the point charge response. In fact, if we reintroduce our understanding of dipole moment and polarizability, we can further advance 1.13 by combining it with 1.2, substituting r_i for x_0,

$$\mathbf{P} = \frac{e^2\mathbf{E}}{m}\frac{1}{\omega_0^2 - \omega^2 - i\gamma\omega} \tag{1.14}$$

and then solving for the electric susceptibility using Eqn. 1.3,

$$\chi = \frac{ne^2}{\varepsilon_0 m}\frac{1}{\omega_0^2 - \omega^2 - i\gamma\omega} \tag{1.15}$$

we arrive at a new definition for susceptibility which will prove to be much more useful for understanding plasmons. Should we happen to take Eqn. 1.15 further, we can also incorporate the electric permittivity term by its relationship in Eqn. 1.6,

$$\varepsilon = 1 + \frac{ne^2}{\varepsilon_0 m}\frac{1}{\omega_0^2 - \omega^2 - i\gamma\omega} \tag{1.16}$$

to arrive at a complex permittivity, sometimes referred to as the dielectric function.

Complex Permittivity. Complex permittivity, as the name suggests, can be broken down into real (ε_1) and imaginary (ε_2) components that are optically observable in frequency space. Figure 1.1A highlights an example using the refractive index (n_r) and extinction coefficient (k_e) data of gold from 1972 collected by Johnson and Christy.[15] By using Eqn. 1.17,[16] ε_1 and ε_2 are calculated and plotted.

$$\varepsilon_1(\omega) = (n_\mathrm{r}^2 - k_\mathrm{e}^2), \;\; \varepsilon_2(\omega) = 2n_\mathrm{r}k_\mathrm{e} \tag{1.17}$$

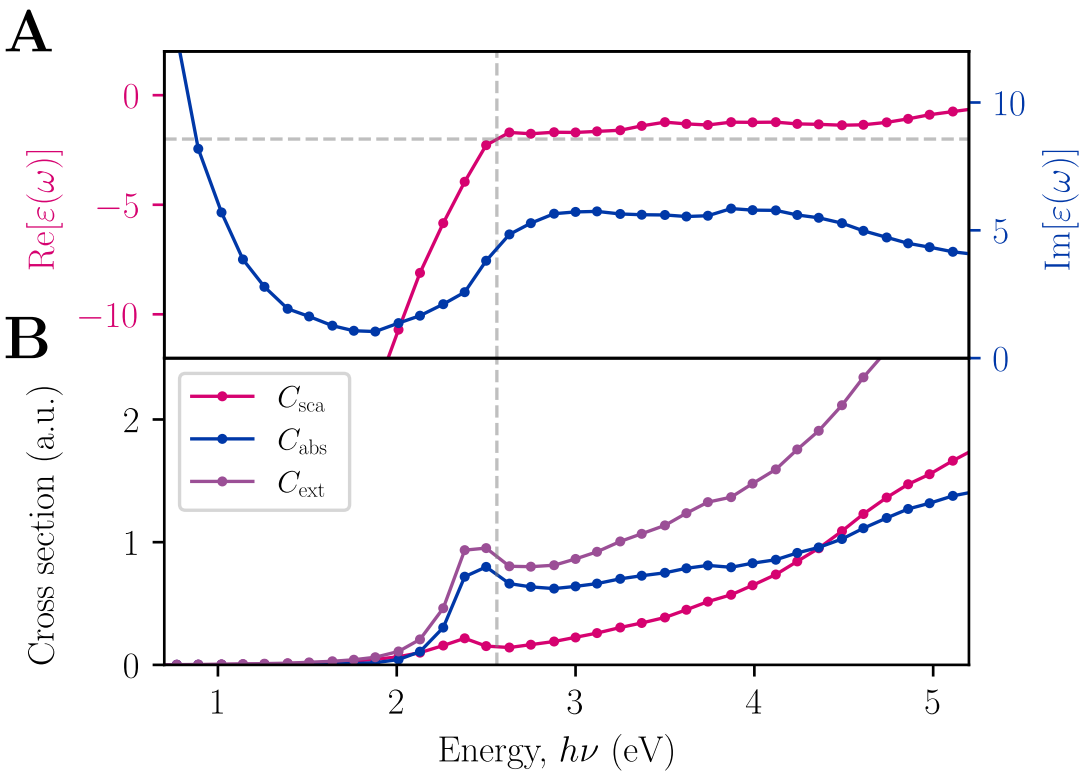

Figure 1.1: (**A**) Complex permittivity spectrum for Au calculated from the experimental n_r and k_e data from Johnson and Christy and (**B**) the resultant extinction, absorption, and scattering spectra

The real component of the complex permittivity can be thought of as the polarizability or Coulombic oscillator response typically observed as a derivative-like function, while the imaginary can be viewed as the absorptive term, mimicking the shape of typical Gaussian absorption features in spectroscopy. However, both components are necessary to describe optical absorption and scattering phenomena in materials.

For spherical particles smaller than a wavelength of light, if one were to assume that the electric field experienced by the particle is equivalent across the particle size (*i.e.* the quasi-static approximation), it is mathematically straightforward to understand how complex permittivity directly leads to a material's absorption and scattering cross sections,

$$C_{\text{sca}} = \frac{8\pi k^4 r^6}{3} \left| \frac{\varepsilon - \varepsilon_m}{\varepsilon + 2\varepsilon_m} \right|^2 \tag{1.18}$$

$$C_{\text{abs}} = 4\pi k r^3 \,\text{Im}\left\{\frac{\varepsilon - \varepsilon_m}{\varepsilon + 2\varepsilon_m}\right\} \tag{1.19}$$

where $k = 2\pi/\lambda$, r is the particle radius, ε is the complex permittivity $(\varepsilon_1 - i\varepsilon_2)$, and ε_m is the dielectric constant of the particle surrounding medium. Just as simply, a material's extinction will be the sum of cross sections:

$$C_{\text{ext}} = C_{\text{sca}} + C_{\text{abs}} \tag{1.20}$$

Figure 1.1B shows all cross sections as a function of energy in one plot for 40 nm Au nanoparticles in air ($\varepsilon_m = 1.00059$). Note that for nanoparticles $r \ll \lambda$, C_{abs} will contribute significantly greater to the total C_{ext} compared with C_{sca}.

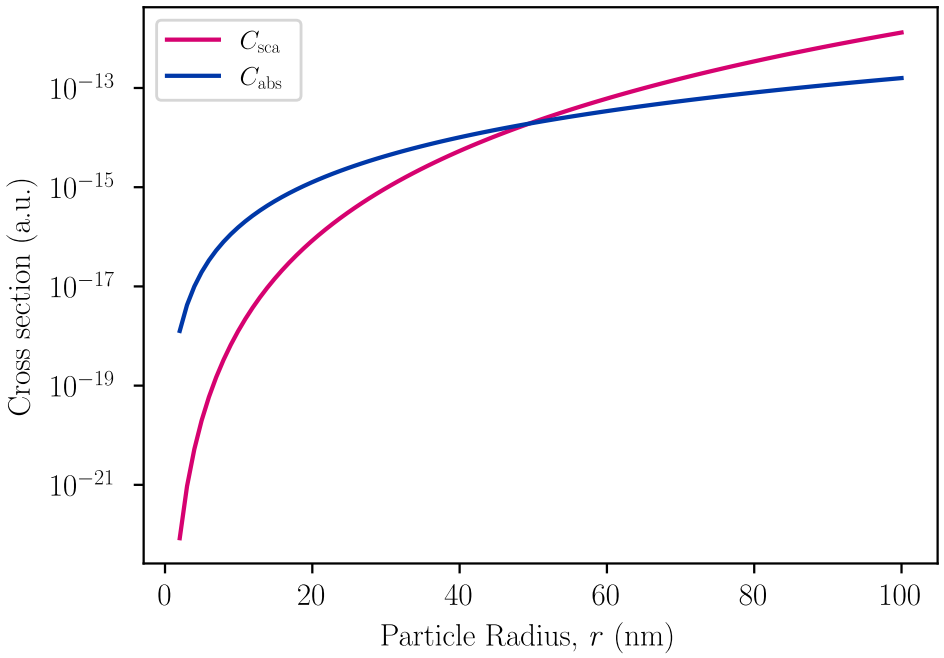

Figure 1.2: Scattering and absorption cross sections compared as a function of particle radius

Figure 1.2 shows the relative contribution of scattering versus absorption as a function of particle radius for one wavelength. Depending on the medium dielectric and complex permittivity at a given wavelength, the crossover from absorption dominating to scattering dominating cross section will shift.

Conveniently, the optical response of a dielectric material can be fully calculated once the complex permittivity is known, especially for a mono-metallic system such as Au or Ag using Eqns. 1.18 - 1.20. Inconveniently for materials scientists however, is that developing new materials which incorporate multiple elements to obtain new or improved properties typically leads to a nonlinear combination of frequency dependent permittivity, and thus representative simulation becomes more difficult. Programs such as COMSOL Multiphysics or MEEP can be useful for obtaining extinction spectra from permittivity data, but inevitably the quality of simulation is dictated by the availability of experimental data for the material of interest, usually obtained through careful ellipsometry. Alternatively, effective medium theories can be used to better approximate experimentally observed permittivity when knowing the fundamental dielectric properties of the individual components. Several theories exist that have been used to great effect, including the Maxwell-Garnett theory the Bruggeman medium theory, and extensions of the theories to fit experimental extinction data using only material property information.[17] Further discussion of these approximations can be found in other works.[18]

The Free Electron Model. Now that we have an understanding of how electric fields interact with charges and simple spherical geometries, we are now equipped with the tools to begin understanding what plasmons are and how we can quantitatively explore them. The Free Election Model refers to the combined Drude-Lorentz model, later extended by Sommerfeld and Bloch to include Fermi-Dirac statistics and implement the concept of electronic interactions in a periodic lattice.[12,19,20] As a whole, the Free Electron Model is a relatively simple semi-empirical model which has been shown to be very predictive for how mathematically straightforward it is. Electronic properties such as charge carrier density, effective mass, mobility, conductivity, scattering rate, mean free path, heat capacity, and others can all be extracted and understood by the Free Electron Model. The seminal work by Kittel[4] explores many of these relationships and the reader is directed there for a more thorough breakdown.

Returning to Eqn. 1.16, one should notice that the solution for complex permittivity can be separated into two components: a scaling factor dependent on properties of the electric charge ($\frac{ne^2}{\varepsilon_0 m}$) and the damped oscillator response itself ($\frac{1}{\omega_0^2-\omega^2-i\gamma\omega}$). The former represents the energy at which the oscillator strength is maximized, while the latter represents the oscillatory force in response to an electric field resonant with the electronic charges. In plasma physics, we define ω_p:

$$\omega_p^2 = \frac{ne^2}{\varepsilon_0 m^*} \tag{1.21}$$

as the plasma frequency. Eqn. 1.21 is squared because in Eqn. 1.16, where it originates, it is expressed in terms of frequency squared units. In effect, just as a tuning fork resonates at some particular frequency, so too do negative and positive electric charges resonate at the plasma frequency. ω_p is dependent on the charge carrier density, n, and the charge carrier *effective* mass, m^*. While electrons are measured to have a mass, m_e, of 9.11×10^{-31} kg in vacuum, various forces in solid-state systems may be acting upon the electron in such a way that they modify the mobility or mean free path, thereby equivalently changing the *effective* mass of the electron. Through the Free Electron Model, one also arrives at calculations for mobility, conductivity, and most importantly the Fermi energy, E_F, or Fermi level,

$$\mu = \frac{e\bar{\tau}}{m^*} \tag{1.22}$$

$$\sigma = ne\mu = \frac{ne^2\bar{\tau}}{m^*} \tag{1.23}$$

$$E_\mathrm{F} = \frac{\hbar^2}{2m^*}\left(3\pi^2 n\right)^{\frac{2}{3}} \tag{1.24}$$

where μ is carrier mobility, $\bar{\tau}$ is the scattering rate, σ is conductivity, and $\hbar$ is the reduced Planck constant. Here, we focus on the Fermi energy which represents the average chemical potential for a three-dimensional electron gas. At zero temperature, all electrons would theoretically have this energy, however at higher temperature electrons will instead follow the Fermi-Dirac distribution,

$$\frac{1}{1 + e^{(E - E_\mathrm{F})/(k_B T)}} \tag{1.25}$$

where E is energy in eV, k_B is the Boltzmann constant ($8.617\,333\,262 \times 10^{-5}$, and T is temperature in Kelvin. Fermi-Dirac statistics apply explicitly to fermions, or integer-half spin quasiparticles, and thus apply to both electrons and holes. In the limit of high temperature and low particle density, Fermi-Dirac statistics approach Maxwell-Boltzmann, however because the free carrier density of PSNCs are very high, the Fermi-Dirac distribution is more representative of experimentally observed PSNCs.[21]

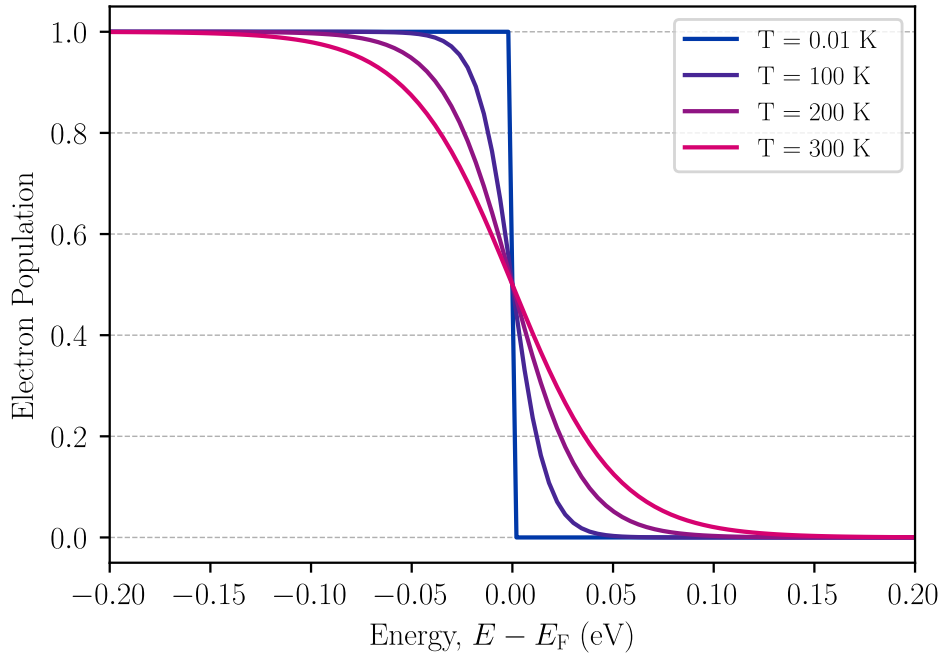

Figure 1.3: Fermi-Dirac energy distributions are plotted as a function of temperature in Kelvin, where the Fermi energy is centered at 0 eV

Figure 1.3 showcases how the Fermi-Dirac distribution evolves as a function of temperature, where a sharp discontinuity at the Fermi level (0 eV) for near zero temperature is observed, representing the energy level which nearly all electrons are at. As temperature increases, the distribution widens, where a gradient of electron population experiences energies that are slightly above and below the Fermi level. Near room temperature, electron energies vary by almost ± 0.15 eV from the Fermi energy due to the inherent thermal contributions of $k_B T$.

From Fermi-Dirac statistics, we are also introduced to the concept of *holes*, h^+. Holes are quasiparticles just as electrons are, and they are represented by the lack of an electron in a sea of electrons. Semiconductors, discussed more in depth in Section 1.2, are classified as n- or p-type which are determined by the majority charge carriers being electrons or holes respectively. In effect, the n-type semiconductor has electrons in the conduction band while p-type semiconductors lack an electron in the valence band. An even simpler picture at a molecular level is one can imagine these charges as a radical species generated by oxidation (h^+) or reduction (e^-) of the molecular species. Consequently, holes are typically observed to have smaller μ and higher m^*, which also happens to

be reflected in the electronic band structure of semiconductor materials discussed in greater depth in Section 1.2. Conveniently, holes are semi-empirically treated the same way as electrons are in the Free Electron Model, and also can be the dominant charge carrier species for plasmons.

1.1.3 Carrier Density and Effective Mass

For plasmonic NCs, values of n and m^* can range between $\times 10^{17} - \times 10^{23}$ cm^{-3} and $0.01 - 10$ times m_e respectively. Noble metal NCs such as Au are known to have an m^* of 0.99 with n on the order of $\times 10^{22}$ cm^{-3}.[15,22] Plasmonic *semiconductor* NCs (PSNCs) can have lower effective masses such as ZnO with 0.22 m^*, leading to greater carrier mobility, but at the cost of a lower n of 1.4×10^{20} cm^{-3}.[23] These trade-offs occur due to the inverse relationship of n and m^* with constant ω_p as defined in Eqn. 1.21. ω_p is also widely tunable for plasmonic NCs, ranging from near-ultraviolet to mid-infrared depending on NC composition, size, and morphology.[8,24–27]

There is currently a debate in literature as to the accuracy of particular methods of obtaining both n and m^*. Historically, carrier property measurements have been obtained on thin-film or bulk type materials through the Hall Effect.[28] However, in an assembly of NCs, problems arise with contact conductivity and the appearance of a metal-insulator transition of the assembly itself which depends on the degree of contact conductivity between NCs.[29–31] Unless a perfect single crystal material of some semiconductor can be synthesized, an applied current measurement for an assembly of NCs will either be significantly attenuated or non-transmissive due to the lack of a conductive path for electron current flow, resulting in an inaccurate n or m^*.

Chemical Titration for *n*. Chemical titration of n-type PSNCs with one-electron oxidants such as nitrosonium tetrafluoroborate ($NOBF_4$),[32,33] cerium ammonium nitrate (CAN),[34] or even decamethylferrocenium tetrakis[3,5-bis(trifluoromethyl)phenyl]borate ($[FeCp^*_2][BAr_F]$)[35,36] have been used for the past decade or more to quantitatively extract n for PSNCs. However, it is also known that with the introduction of strong oxidants such as $NOBF_4$, also a common ligand stripping agent,[37] the oxidative potential of the titrant may induce simultaneous ligand dissociation and a subsequent crashing out of NCs from solution due to their loss of their ligand shell, resulting in inaccurate n values.[34] Therefore, the oxidative potential of a titrant should be considered very carefully for n-type PSNCs. p-type PSNC chemical titration is much less explored, with cobaltocene (Cp_2Co) as the most popular choice.[38] Considering that the only source of h^+ for Cp_2Co

to populate originates from LSPR free carriers, there should be no side reduction events occurring for p-type PSNCs, the same for which cannot be said of n-type PSNCs. In either case, one relates the quantitative addition of the titrant of choice into a solution of PSNCs, where an extinction spectrum is measured at each titration amount added. From there, a plot of LSPR frequency or peak area versus electron equivalents can be plotted and extrapolated to zero, where n can be calculated using a known NC size obtained either from transmission electron microscopy (TEM) or powder x-ray diffraction (pXRD) size analysis.

Analytical Drude Approximations for *n*. Another method of quantifying n for PSNCs is by taking advantage of the LSPR extinction spectrum without any experimental modification. Thanks to the free electron model, the simple Drude approximation (SDA) was first developed by Milliron and coworkers to analytically extract plasmon properties simply by performing a nonlinear regression on the plasmon extinction feature in MATLAB.[39] Simply, the volume fraction (V), plasmon frequency(ω_{p}), and damping constant (Γ) are the three floating parameters needed to perform the nonlinear fit on a Gaussian-like LSPR extinction spectrum, solving for Eqn. 1.19 where the imaginary complex permittivity is replaced with an effective dielectric constant based on a convolution of the NC, solvent, and ligand dielectric constants using effective medium approximation theory. Conveniently, the SDA can be used to also fit LSPRs that are multimodal due to the introduction of morphology, such as for rods, cubes, or octahedrons.

In the event of an asymmetrical LSPR feature, the simple, extended Drude approximation (SXDA) can be utilized which further expands the damping term using high frequency (Γ_{H}), low frequency (Γ_{L}), frequency width (Γ_{W}), and crossover frequency (Γ_{X}) parameters, where Γ is defined by Eqn. 1.26:[40,41]

$$\Gamma(\omega) = \Gamma_{\mathrm{L}} - \frac{\Gamma_{\mathrm{L}} - \Gamma_{\mathrm{H}}}{\pi}\left[\tan^{-1}\left(\frac{\Gamma_{\mathrm{X}}}{\Gamma_{\mathrm{W}}}\right) + \frac{\pi}{2}\right] \tag{1.26}$$

The relative differences between Γ_{H} and Γ_{L} give information on the degree of NC depletion and ionized impurity contribution. For example an LSPR with higher Γ_{L} than Γ_{H} is indicative of uniform carrier activation throughout an NC, while spectrally symmetrical LSPR features which have nearly identical Γ_{L} and Γ_{H} are thought to have carrier activation segregated more at the surface of the NC.[41]

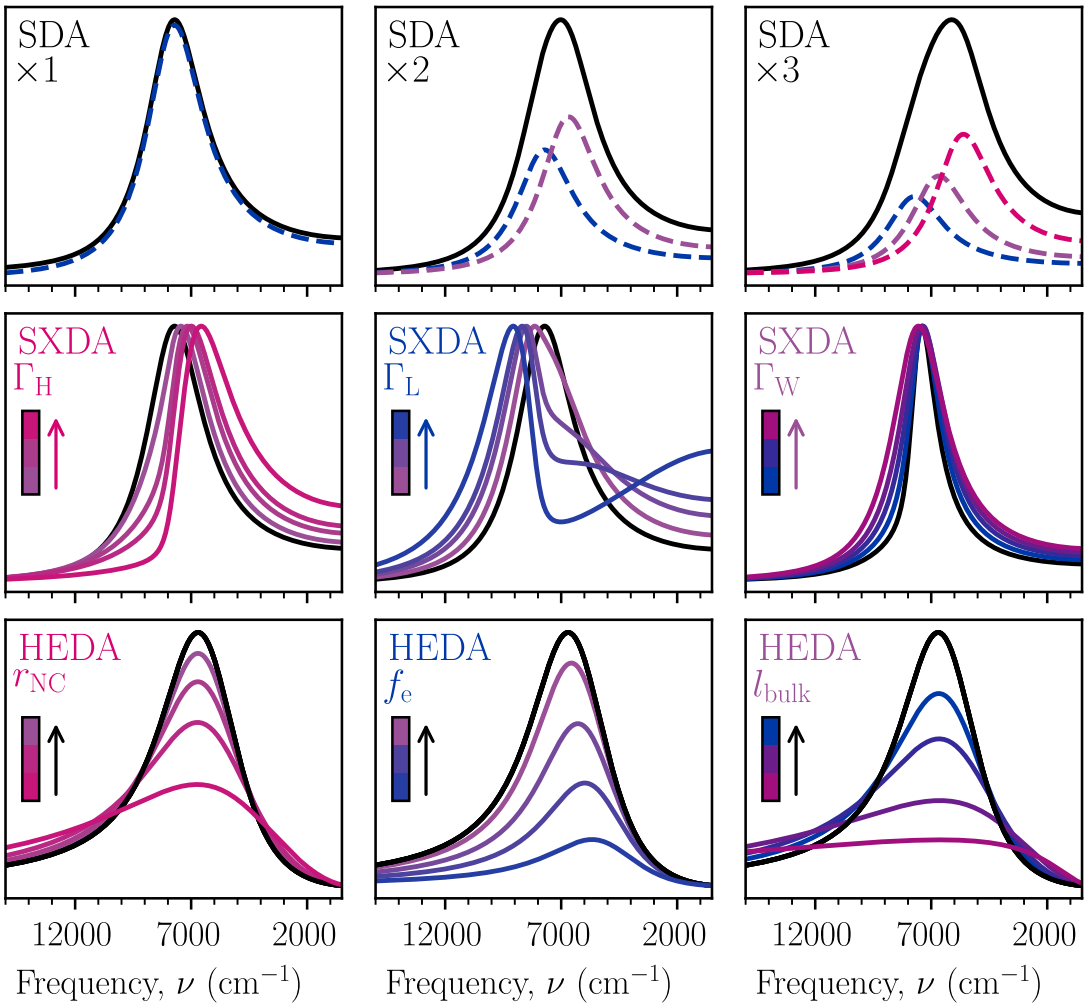

Figure 1.4: Comparison of SDA, SXDA, and HEDA models with changing parameters.

The penultimate Drude based analytical approximation is currently the heterogeneous ensemble Drude approximation (HEDA) which accounts for the heterogeneity of an ensemble of NCs which have some standard deviation representing their size distribution.[42] In this most recent model, The fitting parameters are instead n, standard deviation of n, electron-accessible volume fraction (f_e), and the bulk mean free path ($l_{\mathbf{bulk}}$) with static input parameters of volume fraction, NC radius (r_{NC}), standard deviation, and m^*. As different NC sizes correlate to differences in LSPR frequency and Γ, the approximation simulates a binned distribution of different sizes using the input NC radius and standard deviation with an experimentally determined volume fraction which

can be calculated from the NC size and mass obtained from thermal gravimetric analysis. For polydisperse PSNCs, this method has also shown to be very effective at extracting useful optical parameters such as C_{ext}, μ, and σ.[42,43]

Figure 1.4 highlights the immediate differences for SDA, SXDA, and HEDA models with shared parameters except for a single parameter specified in each specific subplot. From left to right, SDA is used to illustrate how adding LSPR peaks contributes to the overall LSPR extinction feature, mimicking the evolution of LSPR modes as an NC progresses from sphere, rod, to an octahedron, where the relative intensities are representative of faceted plasmonic nanocrystals observed or simulated in literature.[44,45] To highlight possible changes in frequency-dependent damping, SXDA parameters Γ_{H}, Γ_{L}, and Γ_{W} are isolated from Eqn. 1.26, where each parameter is increased sequentially ($\Gamma_{\text{H}}, \Gamma_{\text{L}}$: 3000 $\rightarrow$ 15000 cm^{-1}; Γ_{W}: 500 $\rightarrow$ 5000 cm^{-1}) while all other parameters are held constant. To illustrate the effect on critical HEDA parameters, r_{NC}, f_{e}, and r_{NC} are decreased sequentially (r_{NC}: 5 $\rightarrow$ 1 nm; f_{e}: 100 $\rightarrow$ 20 %; r_{NC}: 5 $\rightarrow$ 0.5 nm), showing how all these parameters directly contribute to the LSPR damping and energy to some degree. For any given approximation, it is critical to carefully evaluate the results obtained, especially for HEDA which has several parameters which change the whole LSPR feature in tandem.

Magnetic Circular Dichroism for m^*. For plasmonic semiconductor NCs, magnetic circular dichroism (MCD) has been the technique of choice to directly measure m^*, as there is no need to consider sample contact geometry or interference from ligands from this indirect, magneto-optical technique.[9,22,46,47] m^* has often been neglected in previous literature, with the assumption that it remains constant relative to changes in n. However, when dealing with non-parabolic bands such as is the case with InN or In:CdO,[48,49] m^* changes as n changes, as the quadratic slope of the band changes depth, so too does m^*.

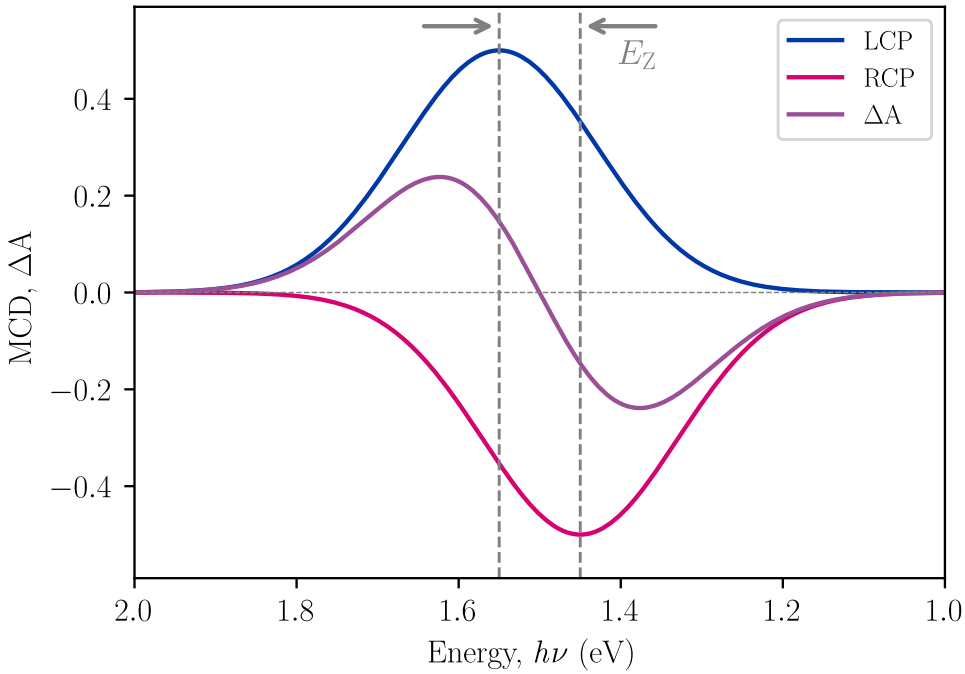

Figure 1.5: Difference between LCP and RCP extinction spectra results in a ΔA MCD spectrum dictated by the E_Z used as a fitting parameter to calculate m^* for plasmon features

Conveniently, the application of a magnetic field induces cyclotron motion of free electrons and holes which introduces Landau levels that can be excited by left and right circularly polarized (LCP,RCP) light. These Landau levels are separated by some energy dictated by the Zeeman effect, represented mathematically in Eqn. 1.27,

$$E_Z = g u_B M_J \vec{B} \tag{1.27}$$

where the difference between Landau levels, E_Z, is referred to as the Zeeman splitting energy, g is the g-factor, μ_B is the Bohr magneton, M_J is the total angular momentum, and $\vec{\mathbf{B}}$ is the externally applied magnetic field vector. E_Z is fundamental to magneto-optical science and allows for the examination of electronic interactions that would otherwise be impossible for traditional optical techniques. MCD takes advantage of Zeeman splitting by utilizing circularly polarized light, where LCP is selective for $\Delta M_J = +1$ while RCP is selective for $\Delta M_J = -1$. These selection rules allow for energy shifting in the LCP and RCP absorption spectra. When the difference between LCP and

RCP is taken to produce a difference spectrum (ΔA), assuming the rigid-shift approximation,[50] a simple derivative like-shape is observed, as illustrated in Figure 1.5. Specifically, the ΔA is induced by the Zeeman effect, contingent on the degree of Landau level splitting proportional to magnetic field strength, rather than originating from a property intrinsic to the material itself such as chirality for circular dichroism.

Assuming that that the ΔA spectrum purely represents excited state splitting of LSPR free carriers, the spectrum can be fit to the difference between LCP and RCP energy shifted extinction spectra, where the difference in energy between LCP and RCP spectra equates to E_{Z}. Understanding that the signal is due to the cyclotron motion of free carriers, we can use our extracted E_{Z} to solve for m^* using the equation for cyclotron resonance frequency, ω_{c}, Eqn. 1.28,

$$m^* = \frac{e\vec{B}}{2\pi\omega_c m_e};\ \omega_c = \frac{E_Z}{\frac{h}{2\pi}} \tag{1.28}$$

where h is the Planck constant in eV/Hz.

1.2 Solid State Chemistry

In solid-state chemistry, one starts with Schrödinger equation for a single electron, where the effective potential is observed to have a periodicity in a repeating solid unit cell, $U(\vec{r}+\vec{R}) = U(\vec{r})$ corresponding to every Bravais lattice vector, $\vec{R}$. The Schrödinger equation, Eqn. 1.29, can be solved by either the free electron model or the tight-binding model.

$$\left[-\frac{\hbar^2}{2m_{\mathrm{e}}}\nabla^2 + U(\vec{r})\right]\psi = \varepsilon\psi \tag{1.29}$$

The free electron model represents a collection of free electrons (not unlike a plasmon) that are only weakly perturbed by nuclear inclusions throughout the lattice. When looking at valence shell transitions (UV energy or less), this approximation is valid due to electron shielding effects from core shell orbitals that minimize interactions with the nucleus. The tight-binding model assumes that electronic interactions are fundamentally tied to the atomic wavefunctions, relying on a modification (electron addition) of the nuclear potential to describe electronic interactions. Tight-binding model electrons are therefore extremely sensitive to the interatomic spacing of atoms, broadening in energy as a function of smaller interatomic distance. Quoting Drs. Rothman and

Boughn, "physics is composed of a collection of models that are brought to bear in explaining physical phenomena, but that these models have limited domains of applicability and as often as not are inconsistent".[51] While there does not exist a combined model to fully predict all states of electronic and light-matter interactions, we can take full advantage of the models which are predictive in the regimes they are applicable for.

To describe the tight-binding model in greater detail, a periodic form of the Schrödinger equation must be discussed, Eqn. 1.30, referred to as a Bloch function.[4]

$$\psi_k(\mathbf{r}) = u_k(\mathbf{r})e^{i\mathbf{k}\cdot\mathbf{r}} \tag{1.30}$$

Bloch states can also be transformed into Wannier functions which are used for effectively modeling the Schrödinger equation for DFT of periodic systems, such as in Quantum ESPRESSO, VASP, and other computational packages discussed later in Section 1.3.4. The Bloch function is designed to represent a single electron which can be observed as a decomposition of traveling waves that migrate across a repeating, periodic potential. For a given $\mathbf{k}$, or momentum wavevector, there are multiple solutions to the Schrödinger where the eigenvalues form the upper and lower bounds of possible energy states for orbitals to be occupied by electrons. Where there exists no solution, gaps between orbitals exist wherein electron population is forbidden, and filling of electrons for the bands which do exist is largely dictated by the atomic identity and arrangement of a given periodic lattice. It is in this regime that traditional electron orbital models such as molecular orbital theory begin to break down in effectiveness.

1.2.1 Band Theory

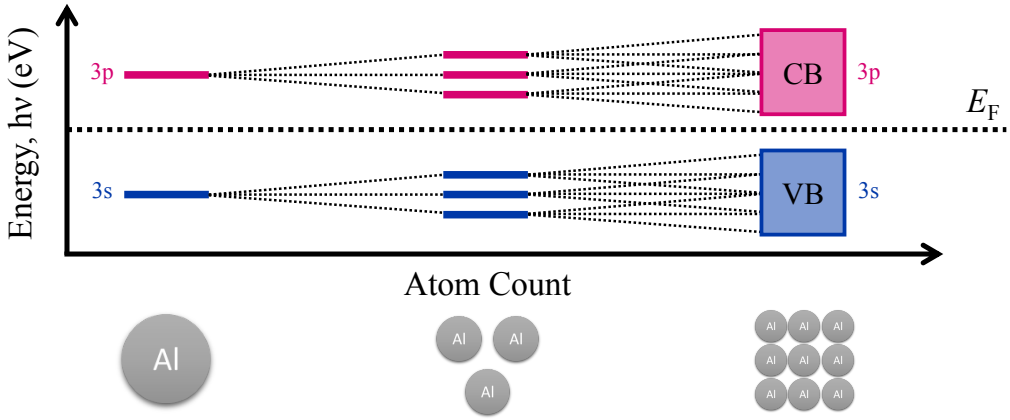

Figure 1.6: An illustration of how molecular orbitals develop into electronic bands as a function of atom count

While molecular orbital theory is an excellent picture for individual molecules as the name suggests, it is limited in describing the electronic interactions of extended solid-state systems. Figure 1.6 provides a simplified illustration for how a molecular orbital picture for aluminium evolves as atom count is increased. With every additional aluminium, a new set of orbitals are added, and because they are all nearly degenerate with one another (prevented from being actually degenerate thanks to Pauli's exclusion principle), solid-state materials which can possess hundreds of thousands of Avogadro's number worth of atoms have orbital energy spacings as small as $\times 10^{-22}$ eV.[52] Because of the degree of energetic overlap, band theory was developed as a result of the tight-binding model to still effectively describe how electronic orbitals and light-matter interactions behave for extended solid-state systems.

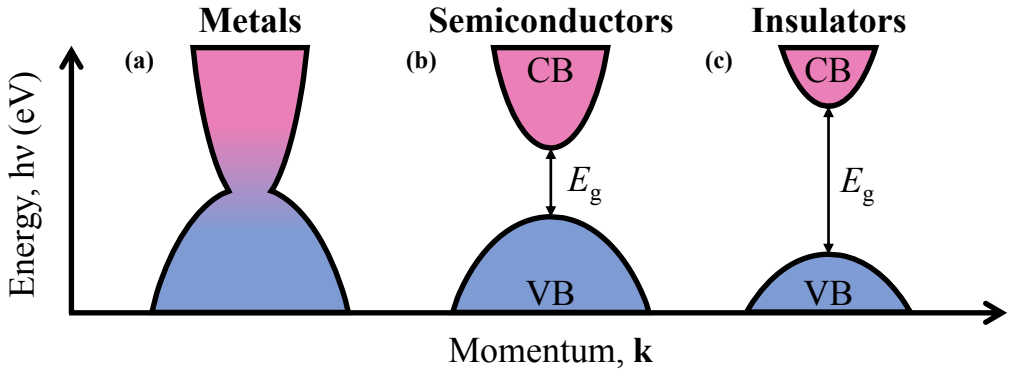

Figure 1.7: Energy band diagrams of metals, semiconductors, and insulators

While plasmons can behave as metallic-like quasiparticles due to their high density of free carriers, the work performed in this thesis focuses on plasmons which are localized on semiconducting NCs. Figure 1.7 showcases representative band diagrams for metals, semiconductors, and insulators from left to right. Metallic systems are highly conductive with high carrier mobility due to the continuous overlap of density of states near the Fermi level E_F. Metals (Figure 1.7.a) such as Au, Ag, and Cu are well known and used for applications where high thermal or electrical conductivity is required, as they offer very lower resistance due to their band structure. In other materials such as Si, or GaAs, an electronic band gap (E_g) can be observed between the highest energy occupied ground state and lowest energy unoccupied excited state, termed the valence (VB) and conduction band (CB) edges respectively for the semiconducting case (Figure 1.7.b). Borrowing from molecular orbital theory, these VB and CB bands can be thought of as analogous to the highest occupied molecular orbital and lowest unoccupied molecular orbital respectively. E_g represents an energy threshold for conduction to occur in the material which can be accomplished either by applying a voltage to overcome E_g, or optically pumping the transition with a photon matching the energy gap. Within Eg, there are no atomic orbitals for the electron to occupy. If E_g becomes large ($\sim >4$ eV), such as in SiO_2 or Al_2O_3, the material is classified as an insulator (Figure 1.7.c), as the voltage or photon energy necessary to overcome the gap is very high relative to the energies typically used for photovoltaic applications.

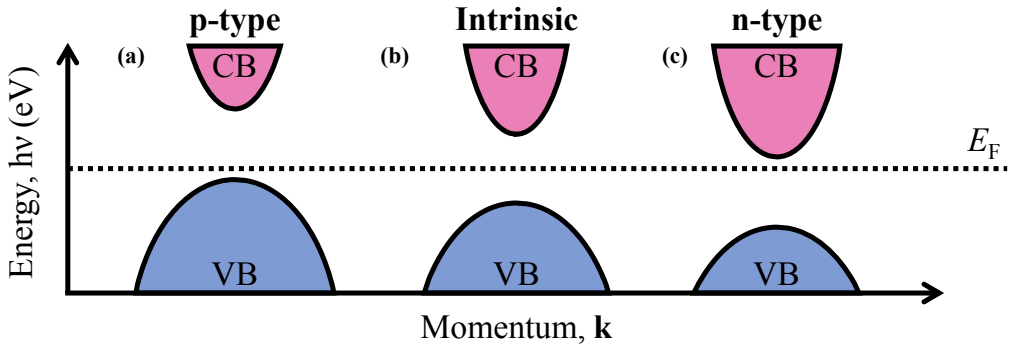

Figure 1.8: Energy band diagrams of p-type, intrinsic, and n-type semiconductors

In the case of semiconductors, carrier concentration, and carrier effective mass are readily tunable via doping. Doping can be performed either intrinsically by creating atomic defects to alter the stoichiometry of a semiconductor (e.g. WO_{3-x}, Cu_xFeS_4, $Cd_{2-x}Sn_{x+1}O_4$) or extrinsically

by introducing a new element (e.g. Gd:WO_3, Al:ZnO). Figure 1.8 shows the cases for positively doped (p-type), intrinsic, and negatively doped (n-type) band structures, where the CB and VB are concomitantly shifted to higher or lower energy with respect to E_F. p-Type semiconductors (Figure 1.8a) such as $Cu_{2-x}O$ exist due to Cu(II) vacancy sites[53] which contribute free holes into the Fermi sea as well as shift the VB and CB higher in energy. Intrinsic semiconductors (Figure 1.8b) are quite poor conductors, so much so that they become insulating near absolute zero. Additionally, they only occur in pure, undoped forms of materials such as Si or GaAs. n-Type semiconductors (Figure 1.8c) such as $Cd_{2-x}Sn_{x+1}O_4$ utilize electrons as the majority charge carrier from Sn(IV) substituting Cd(II) tetrahedral coordination sites (Sn_{Cd} antisites), shifting VB and CB down in energy relative to E_F. Eqn. 1.32 and 1.31 formally shows how holes and electrons are generated from the different doping schemes for $Cu_{2-x}O$ and $Cd_{2-x}Sn_{x+1}O_4$ respectively in Kröger-Vink notation as examples.

$$Cu_{Cu}^{x} \rightleftharpoons v_{Cu}^{''} + 2h^{\cdot} \tag{1.31}$$

$$Cd_{Cd}^{x} \rightleftharpoons Sn_{Cd}^{\cdot\cdot} + 2e^{''} \tag{1.32}$$

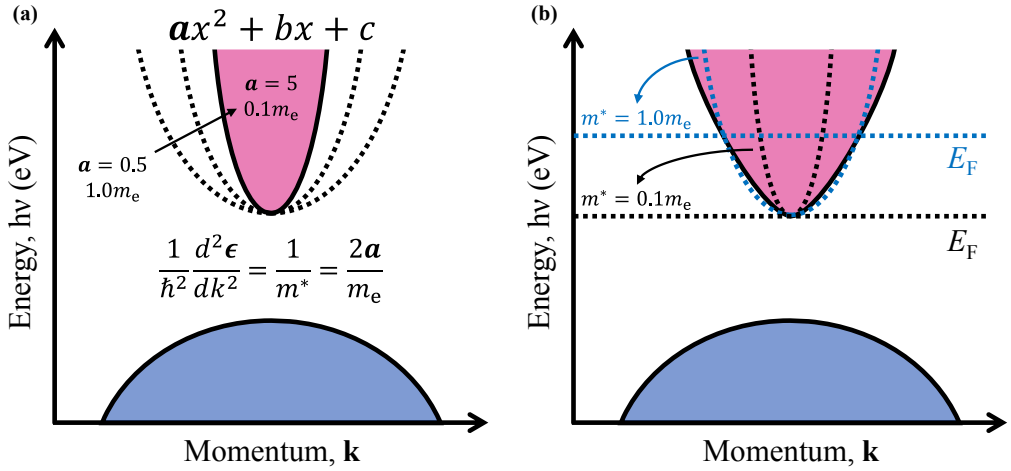

Figure 1.9: Energy band diagrams of parabolic and nonparabolic semiconductors

For all semiconductor types, as the carrier contributing dopant concentration is increased, the carrier density and overall mobility will subsequently increase. Usually, there is a trade-off between

maximizing semiconductor mobility and dopant concentration that is material dependent, such as in the case of Al:ZnO where 12% Al doping results in a 28% lattice mismatch,[33] while a linear response of optical properties with minimal impact on lattice mismatch is observed up to 7.2% for Sn:In_2O_3, resulting in increased carrier damping.[32] Additionally, when designing doping schemes, it is important to analyze the ionic radius of the dopant ion versus the ion being replaced, as a greater mismatch of ionic radius will result in greater lattice distortion and vice versa. For an in-depth analysis and discussion of doping, works by Agrawal et al.[26] and Conti III[54] are excellent reads.

1.2.2 Quasiparticle Interactions

When quasiparticles such as holes or electrons interact with an electronic band structure, there are additional quasiparticles which are critical to describing and understanding solid-state phenomena. Excitons are electron-hole pairs which form as the result of photon absorption promoting an electron to a higher energy electronic orbital. In the previous position of an electron, a hole forms, creating the electron-hole pair quasiparticle. Although the electron and hole of the exciton can be energetically distant by several eV, they may be formed spatially close, within an interatomic distance, to one another, resulting in a Frenkel exciton with high binding energy (0.1 - 1 eV).[55] However, Wannier excitons are also possible which are delocalized across several times an interatomic distance with low binding energies (1 - 100 meV).[56]

Some free carriers can have a greater coupling to particular nuclei in a solid-state lattice, resulting in an increase in m^*. Referred to as polarons, these charge carriers are no longer considered free, resulting in polarons exhibiting higher m^* than observed for semiconductors and higher energies compared to their LSPR counterparts.[57] Materials such as WO_{3-x} have been long discussed for either their plasmonic or polaronic properties, which can give rise to a high level of tunability in changing the energy of the characteristic extinction feature.[58–60]

In order for solid-state lattices to transfer energy and heat throughout, phonon quasiparticles are responsible for electronic and thermal relaxation of thermally hot charge carriers. Phonons transfer energy through the activation of quantized lattice vibrations that can also resonate at some frequency typically in the mid- to far-infrared spectrum. Plasmonic free carriers and phonons can also couple together in semiconductor structures, where the Coulombic motion of free carriers can couple to lattice vibrations on the order of single meV.[61]

1.2.3 Relaxation Pathways in PSNCs

PSNCs have the advantage that nearly all application based phenomena can be achieved through light excitation. Depending on the charge carrier formed and its electronic environment, it can undergo various relaxation processes throughout the NC electronic density of states until it inevitably re-establishes thermodynamic equilibrium. Figure 1.10 illustrates the variety of pathways that excited charge carriers can undergo.

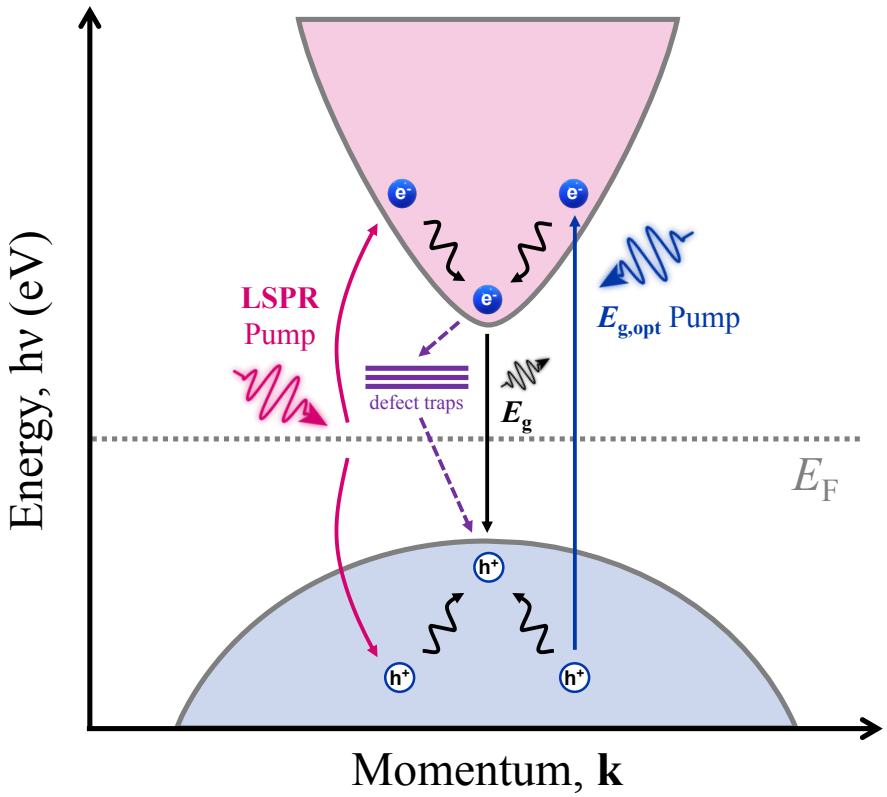

Figure 1.10: Relaxation dynamics of LSPR (pink) and $E_{g,opt}$ (blue) Pumped PSNCs which can all undergo radiative and nonradiative recombination events

In the simplest case, photons ($h\nu$) with enough energy to overcome the PSNC E_g undergo exciton formation where a thermodynamically "hot" electron and hole pair are formed (Figure 1.10, blue line), temporarily disrupting Fermi-Dirac statistics, massively increasing carrier temperature up to thousands of Kelvin for a short time.[10] Because of their large potential difference, they are unable to recombine instantaneously without some energy relaxation process. Consequently, the hot carriers attempt to reach equilibrium by all available pathways possible, where the efficiency of

different pathways is dictated by the relaxation rate. Hot electrons will decrease in energy while hot holes will increase in energy by processes such as auger recombination, trion (three quasiparticle) recombination, or electron-phonon relaxation.[62–65]

Alternatively, for PSNCs, excitation of the plasmon (Figure 1.10, pink line) leads to Landau damping, which is the near instantaneous formation of hot electrons and holes from carrier-carrier scattering.[66,67] The same relaxation pathways are broadly available, just as in the greater than E_{g} case, however the recombination rates will differ depending on the nature of charge carrier generation, such as the case with LSPR formed hot carriers which are not necessarily spatially localized near one another as in the $E_{\mathrm{g,opt}}$ exciton case, one factor for preventing radiative recombination of LSPR generated hot carriers. $E_{\mathrm{g,opt}}$ exciton recombination across the energy gap can result in radiative recombination, provided there is direct band alignment between the CBM and VBM. If there is no direct band alignment, there is an additional $\mathbf{k}$ energy transfer required for recombination to occur, thereby making radiative recombination a forbidden (*i.e* statistically unlikely) process. For electrons, hopping or energy transfer can also occur from the CBM to defect trap acceptor states or intermediate bands nearby, while hole hopping can occur from the VBM to trap donor states.

Several factors can impact the various relaxation rate observed along the pathways mentioned. Higher n in PSNCs lead to greater Coulombic forces, leading to a decreased mean free path and increased scattering rate. Higher m^*, usually caused by the introduction of atomic defects or decrease in band parabolicity, results in faster carrier trapping, leading to faster relaxation and a shorter scattering lifetime (*i.e.* $\tau \propto n \propto \frac{1}{m^*}$). Additionally, depending on where in the energy landscape hot carriers form, they may energetically prefer different pathways. Because of Fermi-Dirac statistics discussed earlier in Section 1.1.2, the same electronic transition can occur over a range of energies, leading to the broad, Gaussian-like features observed in energy resolved transient spectroscopies in the ps regime.[49,65,68]

The following is a useful analogy for hot carrier relaxation after LSPR excitation. Take your hand and aggressively splash it into a still surface of water. Immediately after moment of impact, water droplets in the air and bubbles underwater will rapidly move away from the surface, or the boundary between water and air (equilibrium, E_{F}), representing Landau damping. The droplets and bubbles represent our electrons and holes, respectively. Quickly afterwards, water droplets

in the air begin falling back to the surface, while bubbles rise back to the surface, representing electronic relaxation. As droplets and bubbles begin to recombine with the surface, ripples will be seen throughout as vibrations from collision and recombination occur, ultimately representing the lattice vibrations of thermalization.

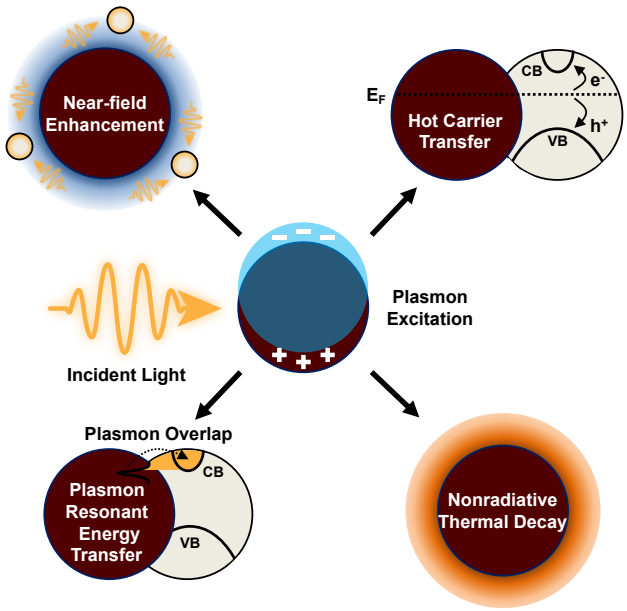

Figure 1.11: Several phenomena can occur from plasmon excitation with light on resonance with the LSPR frequency

From plasmon excitation, a variety of light-matter enhancing phenomena can be observed and manipulated. For example, when incident light interacts with an LSPR such as in Figure 1.11, phenomena such as near-field enhancement,[44,69,70] hot carrier transfer,[71–73] plasmon resonant energy transfer,[74] and nonradiative thermal decay[75–79] are all possible. For example, in the case of wanting to improve hot carrier transfer or plasmon resonant energy transfer, improving n and increasing carrier mobility (decreasing m^*) can increase the likelihood and population of energy transfer.[80]

1.3 Instrumental Techniques

1.3.1 Extinction Spectroscopy

Extinction is mathematically defined as the sum of absorption and scattering light-matter interactions, where the extinction cross section, C_{ext}, is defined by

$$C_{ext} = C_{abs} + C_{sca} \tag{1.33}$$

where C_{abs} and C_{sca} are the wavelength dependent absorption and scattering cross sections respectively.

The only way to measure extinction is by observing the loss of light passing through a material of interest, referred to as transmittance, $T = \frac{I}{I_0}$, where I is the intensity of light transmitted through the sample and I_0 is the intensity of incident light before sample interaction. For chemists, it is easier data-analysis-wise to observe the positive absorbance of something rather than the negative transmittance, and so typically we examine transmittance in terms of absorbance, A, where

$$A = -\log(T) = -\log\left(\frac{I}{I_0}\right) = \varepsilon c l \tag{1.34}$$

Figure 1.12 illustrates a typical linear absorption spectrometer. First, a polychromatic light source such as a xenon arc or tungsten halogen lamp is passed through a linear polarizer, filtered through a monochromator using a diffraction grating to select for monochromatic light, passed through a sample, and diagnosed using a photodetector. Light is oriented to pass through and interact with the sample of interest, where the detector is opposite of the incident photons. This setup is typically referred to as absorption spectroscopy.

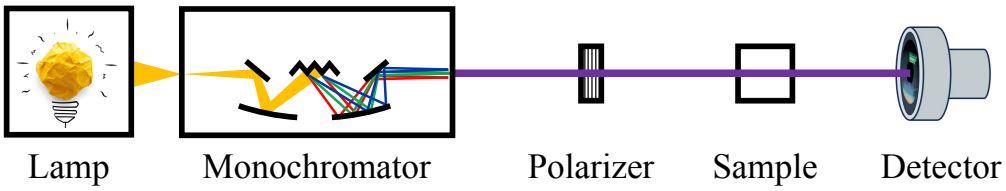

Figure 1.12: Schematic of a typical linear absorption spectrometer

Absorption units (A.U.) and optical density (O.D.) will be used interchangeably in this text, although there are small differences beyond the scope of this text. Both are expressed with log dependence and follow Beer-Lambert law behavior.

Notably, the equation for C_{sca} has an r^6 size dependence, while C_{abs} has an r^3 dependence. These dependencies lead to the observation that C_{abs} dominates the extinction spectrum when $r \ll \lambda$. In the case of PSNCs analyzed in this work (r <30 nm), it may be valid to assume that the spectrum collected in typical UV-vis-NIR-SWIR spectrometers are true absorption spectra due to a negligible C_{sca} contribution. However, for the sake of completeness, spectra collected in a linear absorption configuration will still be considered 'extinction spectra' due to the dual scattering and absorbing nature of LSPRs discussed earlier in section 1.1.2.

Disciplines such as organic or inorganic chemistry primarily focus on C_{abs}, assuming that molecular complexes have negligible scattering contribution when light interacts with those type of samples. However, for PSNCs, contributions from both C_{abs} and C_{sca} cannot be decoupled *via* a linear absorption spectrometer, therefore we refer to the change in intensity observed as extinction.

1.3.2 Magnetic Circular Dichroism

For plasmonic semiconductor NCs, magnetic circular dichroism (MCD) is selected to directly measure m^* without needing to consider sample contact geometry or interference from ligands. In a bulk semiconductor, transport measurements would be traditionally performed to analyze carrier mobility. However, in an assembly of NCs, problems arise with contact conductivity and the appearance of a metal-insulator transition of the assembly itself which depends on the degree of contact conductivity between NCs.[29–31] Therefore, indirect techniques are required to obtain information on the Mott transition of the NCs themselves, thereby avoiding the convolution of resistivity between individual PSNCs in the ensemble. MCD is one such technique which provides a way to indirectly interrogate the mobility of free carriers in LSPR constrained to semiconducting NCs.

MCD experiments can be used as a probe for quantifying energy transitions that may otherwise be convoluted in transitional absorption spectroscopy. MCD has its origins with magnetic optical rotation, otherwise known as the Faraday effect, in which a plane of polarized light was observed to rotate by different amounts due to magnetically induced birefringence as well as differences in the absorption of LCP and RCP.[50] Pinedier et al. observed an opposite asymmetrical A-term LSPR in MCD spectra, denoting an onset of neighboring electronic interband transitions, leading to a sharp variation in the local, imaginary dielectric function, ε_2, contributing to both an asymmetric absorption feature and MCD feature which matched well to MCD simulation.[46] Additionally,

Gamelin and coworkers observed a similar MCD spectral shape up to 6T for a comparable material, $Cu_{2-x}Se$, citing the possibility of LO and TO LSPR contributions due to the shape of their NCs, resulting in the asymmetrical A term and eliminating the possibility of C term contribution after observing minor intensity differences at 1.6 and 30 K.[22]

MCD is also popularly used to elucidate fine structure that may appear in optical features such as band gap absorption edges in semiconductors, charge transfer phenomena, LSPRs, and others. Assuming Born-Oppenheimer, Franck-Condon, and Rigid-Shift (RS) approximations, the ΔA spectrum can be deconvoluted into three constituent shapes classified as A_1, B_0, and C_0 terms:[50]

$$A_1 = \frac{1}{\Gamma}; B_0 = \frac{1}{\Delta E}; C_0 = \frac{1}{kT} \tag{1.35}$$

where Γ is the absorption feature linewidth magnitude, ΔE is the zero-field state separation magnitude, $\mathbf{k}$ is the Boltzmann constant, and T is temperature.[50] The A_1 term originates from the lifting of degeneracy in the nearest excited state as a result of Zeeman splitting directly proportional to the magnetic field applied onto the sample. A_1 term effects are largely identifiable from their derivative shaped curve, where both a positive and negative feature will be present in the differential spectrum. A_1 terms are extremely useful for determining the precise energy level of an electronic orbital at zero field by examining where inflection points appear for the derivative shaped curve. The B_0 term is unique in that it arises from the population mixing of neighboring, nondegenerate excited states at zero-field. As a magnetic field is applied, the change in mixing of populated states accounts for changes observed in a B_0 term feature. C_0 term effects could be considered an opposite process relative to the A_1 term, as nondegeneracy is formed in the ground state of an electronic transition under an applied magnetic field. However, C_0 term contributions are limited to paramagnetic samples and low temperature environments (onset of behavior is typically <50 K).[50] More complicated spectra may have a convolution of terms, and due to the fact that all these possible features are Gaussian in nature, B_0 terms in particular may happen to appear as what are called "pseudo" A and C terms.[81] If the energy difference between two excited states is very small, then it is possible to observe two overlapping B_0 terms of opposite sign, giving the appearance of a pseudo A term. Likewise, if the difference between the ground state and nearest excited state is small, a pseudo C term would be observed without a characteristic temperature

dependence. These term assignments and mixing of electronic states allow for a high-resolution probe into the electronic band structure of any given plasmonic semiconductor NC material. Safin et al. performed work on modeling an absorption spectrum from the measured and term identified MCD spectrum of CdSe/CdS Quantum Dot-in-Rods with good experimental agreement.[82]

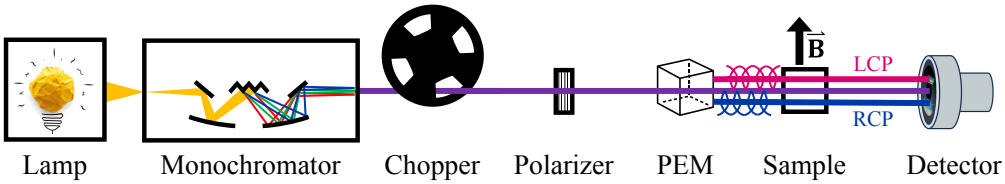

Figure 1.13: Schematic of a typical magnetic circular dichroism spectrometer

For any MCD experiment, a monochromatic photon source, linear polarizer, circular polarizer (photoelastic modulator, PEM), magnetic field source, and detector are fundamentally required, as shown in Figure 1.13. At the NHMFL, a 10 T capable Oxford-Instruments cryostat is used to apply a localized magnetic field onto a probe mounted quartz substrate. The probe provides physical access to a vacuumed sample space, where there are four optical ports by which light can enter, interact with the sample, and exit. Temperature is monitored and controlled through a Kek-Clamp fiber cable routed through the sample probe and mounted adjacent to the sample substrate. The cryostat temperature can be varied from a range of 1.8 to 150 K by combining flow adjustment of liquid He into the sample space in combination with a wired heating controller. The current experimental setup utilizes two SRS 830 lock-in controllers synced to 47 kHz for the PEM vibration frequency and the 211 Hz frequency of the optical chopper. The lock-in amplifiers are utilized to provide both the removal of any background signal or noise not at the reference frequency of the low frequency optical chopper or high frequency PEM that may be present during an experiment run. Conceptually, an MCD signal is obtained by taking the division of the high frequency AC signal (V_{AC}) by the low frequency DC signal (V_{DC}), both measured on the same detector, shown in Eqn. 1.36:

$$\Delta A * k = \frac{V_{\mathrm{AC}}}{V_{\mathrm{DC}}} \tag{1.36}$$

where k is a proportionality constant, and ΔA is the MCD signal.

Samples are prepared by drop-casting a colloidal NC solution onto a quartz or sapphire substrate. Concentration is controlled and monitored by checking the sample substrate using a 3D printed sample holder in a Cary Bio 50 UV-Vis spectrometer or Lambda 950 UV-Vis-NIR spectrometer until an optimal absorbance of approximately 1.0 absorbance unit is obtained. Optionally, if the solvent for a given nanocrystal solution does not bind well to the substrate, poly(lauryl) methacrylate (PLMA) is added as a binder, however this subsequently limits characterization of the sample in the UV spectral window due to the presence of its own absorption feature onset at 400 nm.

In terms of data analysis, an MCD experiment is comprised of an entire set of field strengths separated by some integer interval, starting at the highest strength and decreasing as the experiment progresses (e.g. 10, 8, 6, 4, 2, 0 T). A second set is subsequently taken for the negative field pairs so that each integer interval will have a corresponding opposite field value. Every field integer can subsequently be treated as its own "experiment", and a custom Python code is used to individually fit the simulated MCD spectrum for each field, allowing for the direct measurement of E_Z and m^* for every field, thereby increasing the accuracy and robustness of MCD measurements.[i] The acquisition of m^* through MCD itself is not novel, however the acquisition through comparison by RS approximation of a corresponding absorption spectrum is non-trivial.[22] The novelty originates from the spectral range and standardization of data analysis, which allows for multiple collections of m^* from only one experimental MCD run which sweeps through various magnetic field strengths.

1.3.3 Transient Absorption

Transient absorption (TA) requires two temporally narrow pulses of light, one for "pumping" and one for "probing". The pump pulse can be used either to excite electrons from the ground-state of a material to an excited-state of interest (*e.g.* an $E_{g,opt}$) or to resonantly excite a state of interest (*e.g.* an LSPR). Immediately (on order of fs) afterwards, a probe pulse comprised of polychromatic light is used to stimulate transitions of electrons which can bring electrons to higher excited states, force electrons back to the ground state, or some combination. Formally, we can deconvolute the possibilities by assigning three general phenomena as a photoinduced absorption (PIA), ground state bleach (GSB), or stimulated emission (SE).

[i] https://github.com/strouselabgithub/strouselab

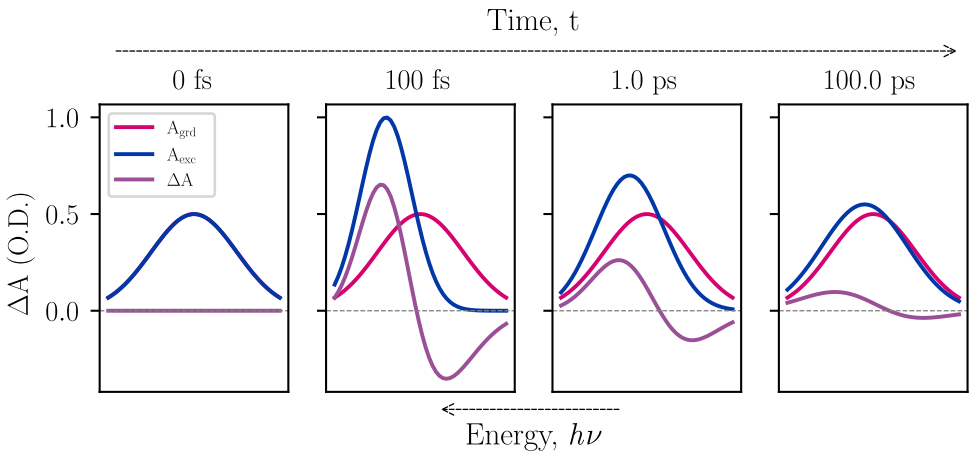

Figure 1.14: Evolution of transient absorption spectra as a function of time

Figure 1.14 illustrates all three assignments occurring concomitantly as a function of time in a ΔA, or difference, spectrum where the photon detectors are designed to observe the difference between excited and ground state absorption spectra ($\Delta A = A_{\text{excited}} - A_{\text{ground}}$). Is important to note, TA spectroscopy only observes signal for the *difference* between electronic states, not the absolute energy of states. As an example, just as in traditional absorption spectroscopy, TA can show the transition of excited state electrons from VB to CB, but give no information on the absolute energy of either state. Therefore, it is necessary to pair TA experiments with additional information such as density of states calculations or ultraviolet photoelectron spectroscopy to properly assign identities to the transitions observed.

As TA monitors excited state processes, the features observed all have finite lifetimes which are dependent on the nature of the phenomenon. Hot carrier relaxation after LSPR excitation is expected to decay with bi-exponential kinetics, where electronic (el-ph) relaxation occurs first on the order of 100 fs - 600 fs, and thermalization (ph-ph) follows on the order of 1 - 100 ps. Auger recombination and carrier trapping is typically observed in the fs - ps regime, while fluorescence and phosphorescence can be seen in the ns to μs regime respectively. In TA, one can even track the transition from carrier trapping at an oxygen vacancy, observed as PIA, to later fluorescence, observed as SE, in a single TA measurement.

1.3.4 Quantum ESPRESSO

For this section, Quantum ESPRESSO[83] (QE) is considered an instrument in the sense that it requires careful, thoughtful user input *via* a collection of processors to obtain results that require interpretation to be scientifically useful. Just as an experimentalist must set up the laser sources and align mirrors to obtain signal, the computationalist must write the code and tune parameters to obtain results.

QE is an open-source density functional theory (DFT) based suite designed to perform electronic structure calculations on solid-state crystal structures. Broadly, this is performed by utilizing various plane waves (PWs) and pseudopotentials (PPs) that are selected and optimized based on unit cell complexity (computational cost), wavefunction accuracy (computational time), and atomic orbitals of interest (frontier vs. core). While DFT through QE is generally designed for ground-state calculations, there are packages included that can perform some simple excited-state (*i.e.* spectroscopic) calculations (*e.g.* dielectric spectra, electron energy-loss spectra), but are rather limited compared to other software explicitly designed for many-body excited-state calculations (*i.e.* BerkeleyGW[84]). Good resources for getting started with QE include the 2021 Materials for MaX Online School GitLab[ii] and a GitHub blog by Pranab Das,[iii] a researcher at the Singapore Synchrotron Light Source.

From first principles, the Schrödinger equation must be solved to make electronic structure predictions for a given material. However, solving the equation exactly is extremely computationally expensive, and so several simplifications are made. First, because we are only concerned with ground-state calculations, the time independent Schrödinger equation can be isolated from the time dependent component. Second, we can isolate only the electronic component, $E = \langle \Psi_0 | \hat{H} | \Psi_0 \rangle$, through Hartree-Fock theory which serves to approximate the wavefunction of interest by using Slater determinants comprised of one spin orbital per electron.[85] Simply stated, DFT uses Hartree-Fock theory as an approximation to minimize the ground-state energy of the wavefunction. The wavefunction eigenenergies are solved *via* self-consistent field (SCF) methods for the equation $\mathbf{FC} = \mathbf{SCE^F}$ where $\mathbf{F}$ is the Fock matrix, $\mathbf{C}$ is the molecular orbital coefficient matrix, $\mathbf{S_{AO}}$ is the atomic orbital overlap matrix, and $\mathbf{E^F}$ is the diagonal matrix of eigenenergies.[85] The name, self-consistency,

[ii] https://gitlab.com/QEF/materials-for-max-qe2021-online-school
[iii] https://pranabdas.github.io/espresso/

originates from the method of starting with an initial guess for **C** and iterating on guesses until the equation is equal on both sides (to an error dictated by user input, typically $\times 10^{-8}$).

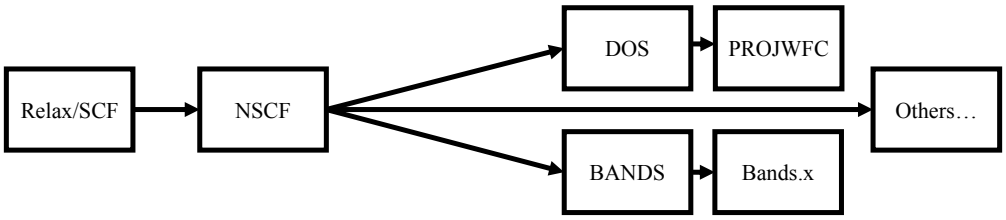

Figure 1.15: Diagram of fundamental QE workflow

As we are interested in solid-state lattices, QE SCF calculations are also designed to sample a user-specified amount of points in **k**-space along various crystallographic axes, solving the KS equation at each **k**-point. Kohn-Sham SCF is the foundation for QE calculations, as obtaining self-consistently accurate ground state energy of a material is the prerequisite to obtaining useful energy and **k**-resolved density of states.[iv] After an SCF calculation, typically we increase the sampling by increasing the number of k-points through a non-self-consistent field (NSCF) calculation, using the atomic charge density and wavefunction solutions from the first SCF step. From the higher resolution NSCF, the atomic and electron orbital projected density of states can be extracted. To obtain **k**-space resolved band diagrams, an additional step must be taken, where instead of evenly sampling across **k**-space, one specifies the crystallographic reciprocal space along particular **k**-points such as the Γ or X points. SeeK-Path[v] is a useful tool to obtain a starting point, where the desired unit cell is symmetrized to its primitive unit cell and a recommended **k**-point path is given. This overall workflow is diagrammed in Figure 1.15 based on the QE environment.

[iv] https://www.materialscloud.org/work/tools/qeinputgenerator is an excellent starting point for obtaining reasonable starting SCF parameters for QE calculation

[v] https://www.materialscloud.org/work/tools/seekpath

CHAPTER 2

PLASMON-INDUCED HOT-CARRIER EXCITED-STATE DYNAMICS IN PLASMONIC SEMICONDUCTOR NANOCRYSTALS

2.1 Abstract

The variance of carrier relaxation pathways for WO_{3-x} plasmonic semiconductor nanocrystals (PSNCs) is monitored by transient absorption spectroscopy following excitation of the localized surface plasmon resonance (LSPR) versus the optical band gap ($E_{g,opt}$). Excitation of the LSPR leads to efficient hot carrier population above the Fermi level in WO_{3-x} via Landau damping, in analogy to noble metal LSPR relaxation mechanisms. Hot carrier depopulation occurs on the femtosecond timescale, observed as the concomitant recovery of an LSPR bleach with the appearance of discrete inter- and intraband photoinduced absorption features. By comparison, direct excitation of $E_{g,opt}$ results in trion recombination at donor-acceptor sites within the WO_{3-x} nanocrystal, consistent with exciton decay dynamics observed for typical wide band gap semiconductor nanocrystals. From analysis of pump power dependency data, a hot carrier electron-phonon coupling constant of 1.47x10^{11} J K^{-1} s^{-1} cm^{-3} is extracted. The direct comparison of the decay dynamics following $E_{g,opt}$ versus LSPR excitation confirms that the observed plasmon in TOPO passivated, spherical WO_{3-x} is a resonance state in which hot carriers are generated only from excitation on resonance with the LSPR frequency. This study on WO_{3-x} PSNCs provides a toolset which can be used to evaluate the role of hot carriers following LSPR excitation of n-type, plasmonic transparent conducting oxide nanocrystals, where enhancement of photocatalysis, photovoltaic performance, and optical enhancement has been reported.

2.2 Introduction

A goal in plasmonic materials research is the coupling of plasmonic, electronic, and photonic properties in materials at the nanoscale to enhance device performance.[86] In noble metal and wide band gap plasmonic semiconductor nanocrystals (PSNCs), excitation into the localized surface plasmon (LSPR) is observed to enhance catalytic properties at the nanocrystal surface.[87,88] While noble metal nanocrystal photocatalysts are common in the literature, the use of PSNCs would be advantageous due to their lower costs, high carrier concentrations, ease of plasmon frequency tunability, and lack of visible light absorption.[8,26,89–92] In general, the LSPR in wide band gap metal oxides is attributed to oxygen vacancies (V_O), resulting in a highly tunable plasmon frequency.[93] Despite discrepancies, there is considerable agreement that a collection of mobile charge carriers (free or constrained, plasmonic[87,94,95] or polaronic[96–98]) is responsible for the extinction feature in question and its subsequent material enhancement capabilities. The role of LSPR excitation on catalyst improvement has been attributed to near field enhancement, hot carrier formation at the nanocrystal surface, and carrier trapping at surface bound donor-sites.[99,100] Hot carriers were observed experimentally and reported to occur through Landau damping by electron-electron scattering in the Fermi sea of electrons.[66] Whether hot carriers are formed following LSPR excitation in metal oxide PSNCs is not fully evaluated, as the presence of surface trap sites may play a pivotal role in LSPR relaxation pathways. The role of hot carriers versus surface trap sites in wide band gap metal oxide PSNCs can be evaluated by direct comparison of the dynamics for plasmon relaxation following excitation of the localized surface plasmon resonance (LSPR) versus the optical band gap ($E_{g,opt}$). The hot carrier relaxation dynamics can be directly probed using femtosecond transient absorption (fsTA) to observe simultaneous ground state bleaching of the plasmon along with relaxation through the semiconducting electronic structure of the metal oxide.

In this manuscript, the relaxation dynamics leading to formation of hot carriers following excitation of the LSPR of tri-octyl phosphine oxide (TOPO) passivated, spherical WO_{3-x} (2.4 ± 0.3 nm) is evaluated through transient absorption. The WO_{3-x} nanoparticles have a plasmon extinction feature centered at 1.65 eV with Drude calculated carrier densities of $2x10^{21}$ cm^{-3}. Carrier densities are validated with chemical titration and fitting to Drude model analyses.[32,38,42] Upon directly exciting the LSPR in WO_{3-x}, hot carrier relaxation originating from <100 fs Landau damping is observed in the transient absorption spectra as spectrally distinct populations of inter- and

intra-band transitions concomitant with the recovery of the LSPR. On the contrary, when $E_{g,opt}$ is excited, donor-acceptor (V_d-V_a) trion recombination is experimentally observed. The experimental data support a model where plasmon relaxation in PSNCs generates hot carriers through Landau damping, followed by relaxation through the electronic structure of the PSNC. The lack of inter- and intraband absorptions when $E_{g,opt}$ is directly excited further supports that the LSPR is a resonant state which is not directly coupled to the band structure of the PSNC, consistent with observations in noble metal nanocrystals. To date, exploration of hot carrier formation in wide band gap plasmonic metal oxides (F,In:CdO; WO_{3-x}) has only recently been explored using indirect measures including femtosecond electron transfer to a dye as an indirect probe of the presence of hot carriers[91] or intraband relaxation for the p-type case ($Cu_{2-x}S/Se$)[90]. The full UV-vis-NIR hot carrier spectra are typically not reported in literature for n-type metal oxide plasmonic semiconductors and instead focus on individual features in the spectra instead.[91] To the authors' knowledge, there has been no complete femtosecond UV-vis-NIR spectral analysis of hot carrier relaxation pathways in a PSNC thus far. The confirmation of hot carriers in WO_{3-x} that behave analogously to noble metals would allow implementation of cheaper and more controllable materials for applications where hot carriers can enhance the efficiency of photovoltaic, photocatalytic, opto-electronic, and thermoelectric technologies.[80,101–104]

2.3 Materials and Methods

Materials. Tungsten (IV) chloride (WCl_4, 95%), Nitrosyl tetrafluoroborate ($NOBF_4$, 95%), Toluene (≥99.5%) were purchased from Sigma-Aldrich. Trioctylphosphine Oxide (TOPO, 98%) was obtained from Alfa Aesar. Oleic acid (OA, technical grade, 90%), and Acetonitrile (MeCN) were obtained from VWR.

Microwave Synthesis. In a 10 mL microwave vial (CEM), 30 mg (92.1 μmol) of WCl_4 and 400 μL (1.27 mmol) of OA were combined and transferred for reaction in a microwave reactor (CEM). After insertion, the precursors underwent constant microwave irradiation at 300 W with the vial un-capped for 5 min. After the reaction was complete, vials were immediately removed, quenched with toluene, and the resulting NC suspension was transferred to a gel-permeation chromatography column to clean and remove excess ligand. After cleaning, 1 mg of TOPO was added

to the $WO_{2.76}$ suspension and heated to 65 ℃ while stirring to ligand exchange the native OA for TOPO to improve stability.

Extinction Spectroscopy. $WO_{2.76}$ NCs were suspended in toluene and diluted until an LSPR of between 0.8 – 1.0 absorbance units was obtained under inert (N_2) atmosphere. The suspension was prepared in a 1 mm spectrophotometer cell (Starna Cells, Inc.) on a Varian Cary Bio 50 UV-vis spectrophotometer. A baseline correction was performed with neat toluene.

Photoluminescence (PL) with PL Excitation (PLE). $WO_{2.76}$ NCs were prepared similarly to the methods for extinction spectroscopy. The suspension was prepared in a sub-micro fluorometer cell (Starna Cells, Inc.) where PL and PLE spectra were collected on a Varian Cary Eclipse Fluorescence Spectrophotometer.

Chemical Titration. After preparation and weighing of pristine TOPO-WO_{3-x}, samples were dissolved in dry toluene in an inert atmosphere glovebox. A known concentration of $NOBF_4$ dissolved in MeCN was titrated into the nanocrystal suspension and left to react for 30 minutes. The LSPR of the oxidized sample was then measured by the same instrument as described in the extinction spectroscopy section above. This procedure was repeated until the LSPR showed no decrease in extinction after oxidation.

Powder X-ray Diffraction (pXRD). X-ray powder patterns were collected at room temperature on a Rigaku Miniflex powder diffractometer (Cu Kα source). Samples were dried out, ground to a fine powder, and loaded onto a zero-background micropowder plate. Scans were collected from 10 to 80° 2θ at a rate of 5°/min and a 0.1° step size. Whole pattern fitting was completed using Rigaku SmartLab Studio Software.

High Resolution Transmission Electron Microscopy (HRTEM). Size, size dispersity, morphology, and lattice fringe analysis were conducted by transmission electron microscopy (TEM). TEM images were collected on a Tecnai Osiris TEM/STEM operating at 200 kV. High resolution microstructure characterization was performed using an aberration corrected JEOL ARM 200 F TEM operated at 200 kV. A WO_{3-x} sample was prepared by dispersing the nanocrystals in toluene and octadecylamine (10:1 v:v), heated in an oil bath at 50℃ for 12 hours, sonicated in a 40℃ heated bath for 2 minutes, and ran through a gel permeation chromatography column to remove excess ligand and aggregated solid.[105] The solution was drop-cast onto a carbon-coated 200 mesh gold

TEM grid (Ted Pella 01840G), excess solvent wicked away with a kimwipe 2 sec after deposition, and dried in a vacuum oven at 80℃ for 12h.

X-ray Photoelectron Spectroscopy (XPS). WO_{3-x} nanocrystals were dropcast onto carbon tape in an Ar drybox before transfer into before insertion into a PHI 5100 X-ray photoelectron spectrometer. The XPS has an excitation source of Al Kα, with a pass energy of 22.36 eV to minimize linewidth. All samples were calibrated to the aliphatic carbon assignment (C1s 284.8 eV)

Transient Absorption (TA). Sample preparation for WO_{3-x} NCs was performed the same as the methods previously discussed for extinction spectroscopy. Femtosecond (fs)TA was performed at the Center for Nanoscale Materials (CNM), where measurements of LSPR and optical band gap pumping were performed. A Ti:sapphire amplifier with 2 kHz repetition rate and 35 fs pulse width was used, where pump pulses at 325 nm were generated by directing a portion of the 800 nm laser output to an optical parametric amplifier (OPA). A small portion of the 800 nm Ti:sapphire output was focused into a sapphire crystal to produce white light probe pulses. Probe pulses were mechanically time delayed using a translation stage and retroflector and. Transient absorption spectra for all time points were averaged over 2 s, and three reproducible, separate scans were then averaged together. Background subtraction and probe chirp correction were conducted for all raw spectra before data analysis. All measurements were performed at room temperature and in ambient conditions. For $E_{g,opt}$ pumped experiments at long time scales (Figure S11, bottom), fsTA measurements were performed at Florida State University (FSU) using a commercial HELIOS Fire instrument with a 1024 pixel CMOS sensor and expected probe pulse width of $\tilde{2}$00 fs with the same averaging, background subtraction, and probe chirp correction methods used.

2.4 Results and Discussion

2.4.1 Optical and Structural Characterization of WO_{3-x} NCs.

TOPO-WO_{3-x} nanocrystals (2.4 ± 0.3 nm) were prepared by microwave assisted thermal decomposition of WCl_4 in oleic acid in a 2.45 GHz single mode cavity of the microwave (5 min, 300 W). Synthetic details are provided in the Experimental Section. Size and crystal structure were confirmed by particle distribution and d-spacing analysis. In HRTEM imaging (Figure 2.2, supporting Figure 2.3), the d-spacing is 3.797 Å and can be assigned to the (010) reflection based on the monoclinic $W_{17}O_{47}$ crystal structure (*P12/m1*, ICSD 65084). Confirmation of the crystal

structure assignment for the WO_{3-x} is provided by comparing the experimental diffractogram to simulated 2 nm WO_{3-x} pXRD patterns (Figure 2.4, Table 2.1). The stoichiometry is assigned as $WO_{2.76}$ (x=0.24) based on the ratio of the W 4f to O 2p orbitals in X-ray photoelectron spectra (Figure 2.1). The plasmon feature for isolated TOPO-$WO_{2.76}$ nanocrystals is stable in air for $>$ 40 hr with a decay rate for the plasmon extinction of 2.22 x 10^{-2} hr^{-1} (Figure 2.5).

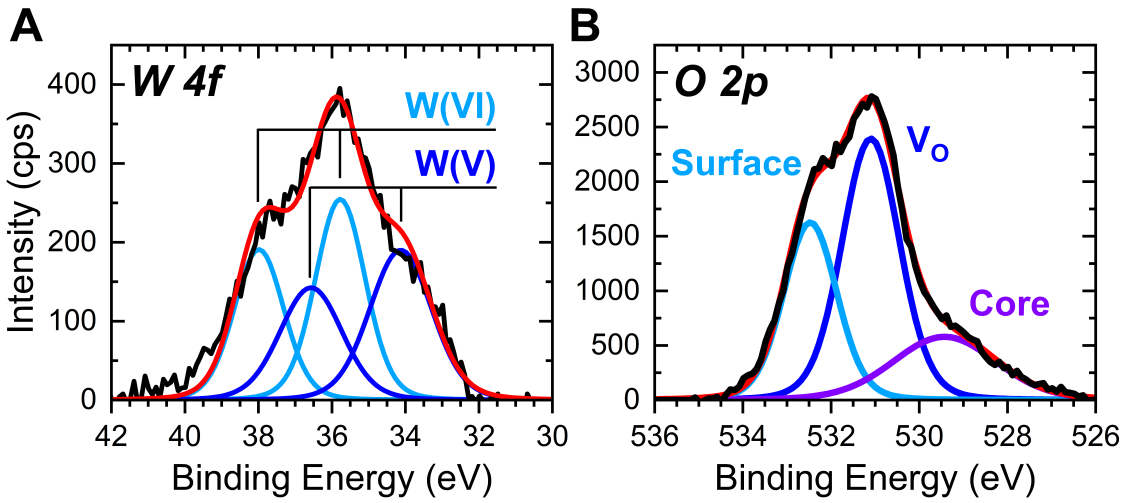

Figure 2.1: XPS for WO_{3-x} Stoichiometry

(**A**) XPS on the W 4f is performed to deconvolute contribution of W(V) from W(VI), where the ratio of W(V):W(VI) was found to be 48:52. (**B**) O 2p XPS of WO_{3-x} NCs was also performed, where three features were deconvoluted as core, V_O, and surface oxygen sites.

XPS is the technique of choice to determine tungstate stoichiometry as has been previously used in literature utilizing Eqn. 2.1.

$$W(V)\% \times 2.5 + W(VI)\% \times 3 = 3 - x \tag{2.1}$$

XPS was performed on dropcast WO_{3-x} nanocrystals on the W 4f and O 2p edges to explore the ratio of W(V):W(VI) and identify oxygen vacancy content respectively (Figure 2.2D). Deconvolution of the tungsten features was performed by fitting W(V) and W(VI) in tandem to the 7/2 and 5/2 4f states to obtain a full spectral fit. The W(V):W(VI) ratio was calculated to be 48%, which when plugged into Eqn. 2.1 identifies the tungsten oxide stoichiometry as $WO_{2.76}$, equivalent to $W_{17}O_{47}$. This assignment is further supported by the large degree of V_O identified from the O

2p XPS spectrum. While the lack of an oxygen atom cannot produce photoelectrons, oxygen neighboring a defect site will have a higher binding energy compared with a typical fully coordinated oxygen and a lower binding energy compared with an oxygen on the surface of a nanocrystal.2 From the fitting deconvolution, the ratio of V_O, core, and surface contributions are xx, xx, and xx % respectively. The stoichiometry is obtained due to rapid nucleation of nanoparticles which depletes precursors instantly, resulting in a metastable state.

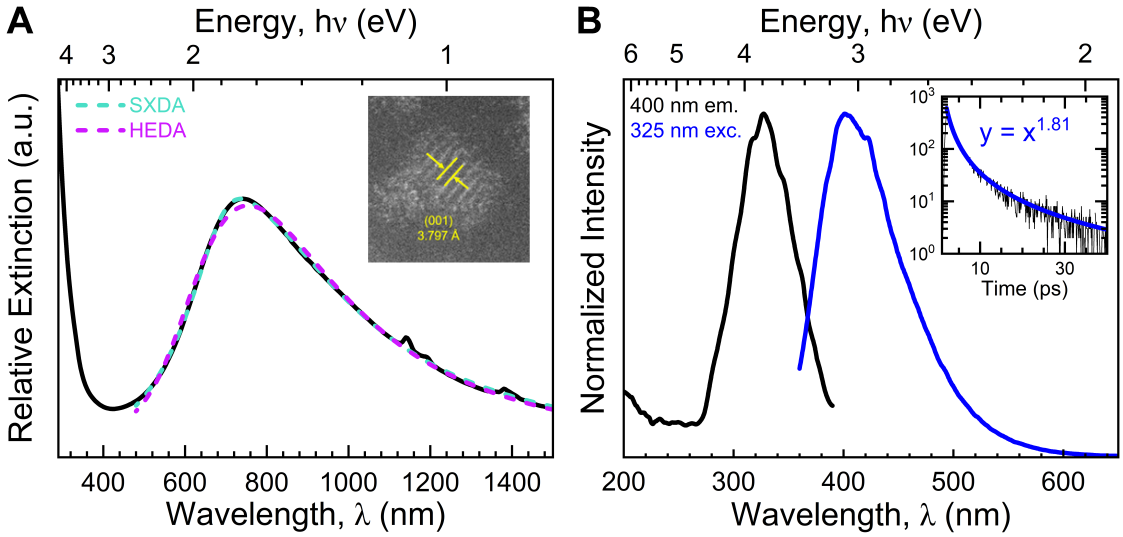

Figure 2.2: Structural and optical investigation of $WO_{2.76}$.

(**A**) An extinction spectrum is taken of 2.4 ± 0.3 nm $WO_{2.76}$ where the plasmon frequency is visible at 1.65 eV. The simplified, extended Drude approximation (SXDA) along with the heterogeneous extended Drude approximation (HEDA) are fit to the extinction feature, with slightly better agreement from SXDA. HRTEM illustrates a representative $WO_{2.76}$ nanocrystal with a (010) lattice spacing of 3.797 Å visible (inset). (**B**) PL and PLE are performed on the band gap of $WO_{2.76}$ which showcases a 3.80 eV optical band gap and subsequent emission peak at 3.10 eV with power law emission dynamics (inset). The emission feature is assigned to a V_O^{2+} to V_O^0 oxygen defect transition.

In Figure 2.2A, the extinction spectrum is shown, where the LSPR is observed at 1.65 eV (760 nm) with an optical band gap ($E_{g,opt}$) at 3.80 eV (325 nm). The optical band gap is attained by fitting the optical spectra via a Tauc plot (Figure 2.6). The carrier density is evaluated by fitting the LSPR feature using the frequency dependent, simplified extended Drude approximation (SXDA) model and compared to the heterogeneous extended Drude approximation (HEDA) model, a model which accounts for a distribution of particle sizes.[42] From the fits, assuming a carrier effective

mass of 1.4 m^*/m_e previously reported in literature,[94] the carrier densities obtained are 2.80x10^{22} (SXDA) and 2.49x10^{22} cm^{-3} (HEDA). The SXDA model provides a slightly better fit than the HEDA model for these samples, likely reflecting the degree of uniformity in the WO_{3-x} samples when prepared via a MW assisted nucleation synthesis.[106] Since PSNCs can exhibit compensation centers, the carrier density obtained by fitting is compared to chemical titration by $NOBF_4$ as a 1-electron oxidant (Figure 2.7). The chemical titration yields a value of 1.80x10^{22} cm^{-3}, which is in good agreement with the values obtained from SXDA and HEDA modeling, suggesting carrier compensation is minimal in WO_{3-x}. The observed agreement in carrier density suggests $NOBF_4$ is an appropriate titrant for WO_{3-x}, which has been observed to not be the case for Sn:IN_2O3.[34] Such an observation may reflect the enhanced stability due to TOPO passivation, removing interfacial compensation centers, as previously suggested by the Milliron[34] and Strouse[32], groups as reasons for the lack of agreement between modeling and chemical titrations.

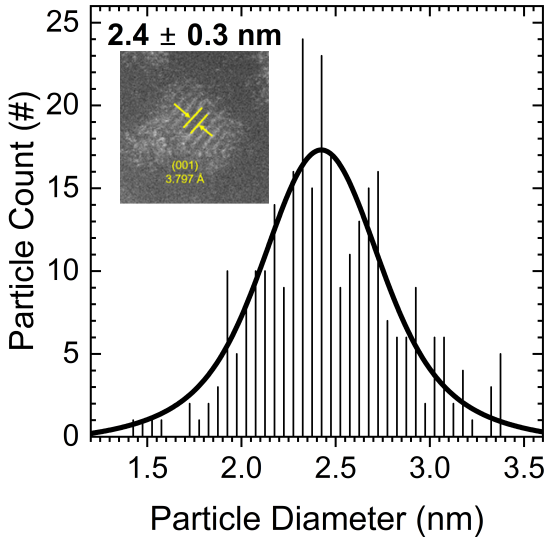

Figure 2.3: HAADF-STEM Nanocrystal Size Analysis.

A nanocrystal size analysis from HAADF-STEM was performed and a Voigt histogram was obtained where the mean size of WO_{3-x} was determined to be 2.4 ± 0.3 nm. Inset shows a representative image of a single TOPO-WO_{3-x} nanocrystal where a spacing of 3.797 Å is observed and assigned to the (010) lattice plane.

As shown in Figure 2.2B, direct excitation of $E_{g,opt}$ (3.80 eV, 325 nm) results in an observed emission at 3.10 eV (400 nm) with an absolute quantum yield of 5%. Excitation of the LSPR (1.65

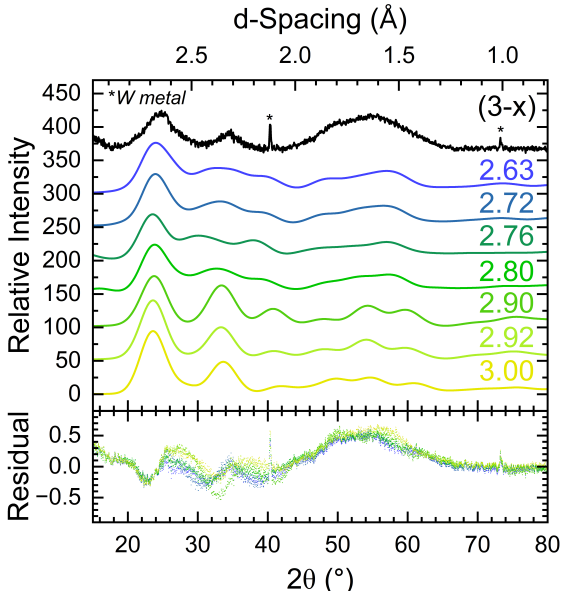

Figure 2.4: pXRD Simulations of 2 nm WO_{3-x} Compared with Experimental pXRD.

Simulated pXRD for 2 nm WO_{3-x}. Simulated pXRD patterns of 2 nm WO_{3-x} with various stoichiometries are compared with the experimentally formed WO_{3-x} plasmonic NC. The asterisks denote small tungsten metal impurities present in the final powder. Qualitatively, the experimental diffractogram compares best with 3-x values below 2.80 and could be fit reasonably well to any of those patterns. Residuals are calculated by subtracting the [0,1] normalized experimental pXRD from the [0,1] normalized simulated diffractograms, where 2.63 and 2.76 have the lowest sum residuals, as illustrated in Table 2.1. Ultimately, the comparison shows that crystal phase determination via pXRD alone is unreliable, as any phase could ultimately be used to fit and claim the observed stoichiometry. The references cards used to generate the simulated patterns were obtained from ICSD. Reference numbers from top to bottom are: 72544, 24731, 65084, 1509, 27705, 392, and 836.

eV, 750 nm) produces no observable PL. Photoluminescence excitation (PLE) monitored at 3.10 eV yields an absorbing feature at 3.80 eV. The observed emission is assigned to V_O^{2+} donor levels, as has been reported in literature for other nanocrystal tungstates.[107–110] The V_O^{2+} donor level emission decay is non-exponential but can be fit to a power law function ($I(x) = Ax^n$), yielding an exponent (n) of 1.81 (Figure 2.2B, inset). Power law behavior for V_O^{2+} emissive centers have been previously reported in defective ZnO and in Cd chalcogenide quantum dots.[111,112] The observation of emission in a plasmonic material is rare but allowable if no electronic interaction or scattering pathway exists to provide non-radiative coupling from the V_O^{2+} donor site to the ground state. Since the experimental measurements are performed on an ensemble, it is not clear if the emission is attributable to a single plasmonic nanocrystal possessing both plasmonic behavior and emissive

Table 2.1: Sum residuals of simulated pXRD patterns from Figure 2.4

3-x	Sum Residuals
2.63	62.09469
2.76	92.43156
2.90	116.7104
2.72	117.4797
2.80	135.9369
2.92	192.3924
3.00	207.6066

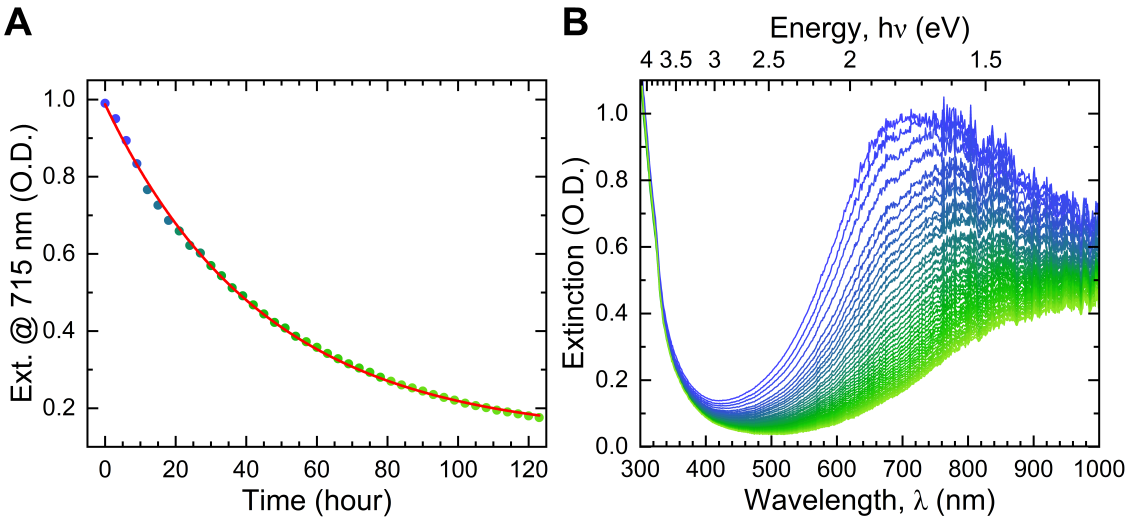

Figure 2.5: Decay Dynamics of TOPO-WO_{3-x} LSPR in Air

(**A**) Ambient air decay of the TOPO-WO_{3-x} LSPR over time at 715 nm with (**B**) the raw extinction spectra showing the intensity and plasmon frequency shift over time.

V_O^{2+} donor states, or to two separate particles in the ensemble. It is worth noting that pristine WO_3 does not exhibit emission.

2.4.2 Femtosecond Hot Carrier Dynamics of WO_{3-x} NCs.

Excitation at 3.80 eV, resonant with the $E_{g,opt}$, or 1.65 eV, resonant with the LSPR, are anticipated to yield discrete optical relaxation behavior. Excitation of $E_{g,opt}$ should lead to exciton recombination via donor-acceptor pair recombination arising at Vd-Va pairs formed to compensate for VO sites in $WO_{2.76}$, or recombine with free carriers present in the PSNC forming a trion

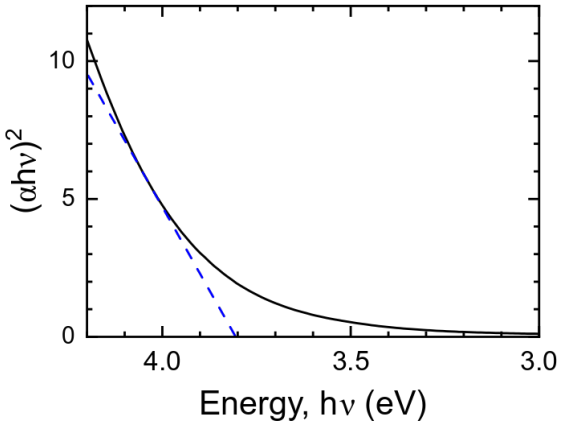

Figure 2.6: Tauc Plot Analysis of WO_{3-x} Optical Band gap $E_{g,opt}$

Tauc plot of the TOPO-WO_{3-x} optical band gap, assuming a direct band gap transition

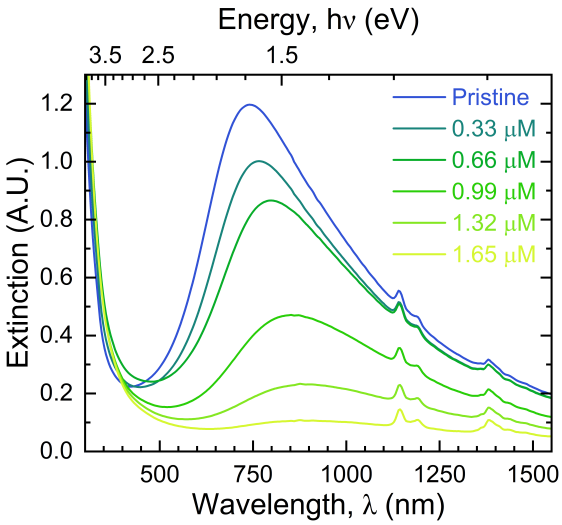

Figure 2.7: Chemical Titration of WO_{3-x} LSPR Monitored Through Extinction Spectroscopy

Extinction spectra of TOPO-WO_{3-x} chemical titrations with incremental additions $NOBF_4$.

(exciton-electron) following Auger processes. The LSPR excitation is anticipated to relax either non-radiatively through scattering processes or through Landau damping generating hot carriers within the conduction band with subsequent thermalization.

In Figure 2.8A, resonant excitation of the LSPR at 1.65 eV produces two prominent photoinduced absorption features (R1 and R2) along with a bleach feature (B1). The R1 and R2 absorption features are attributed to population of electronic levels associated with hot carrier inter- (R1) and

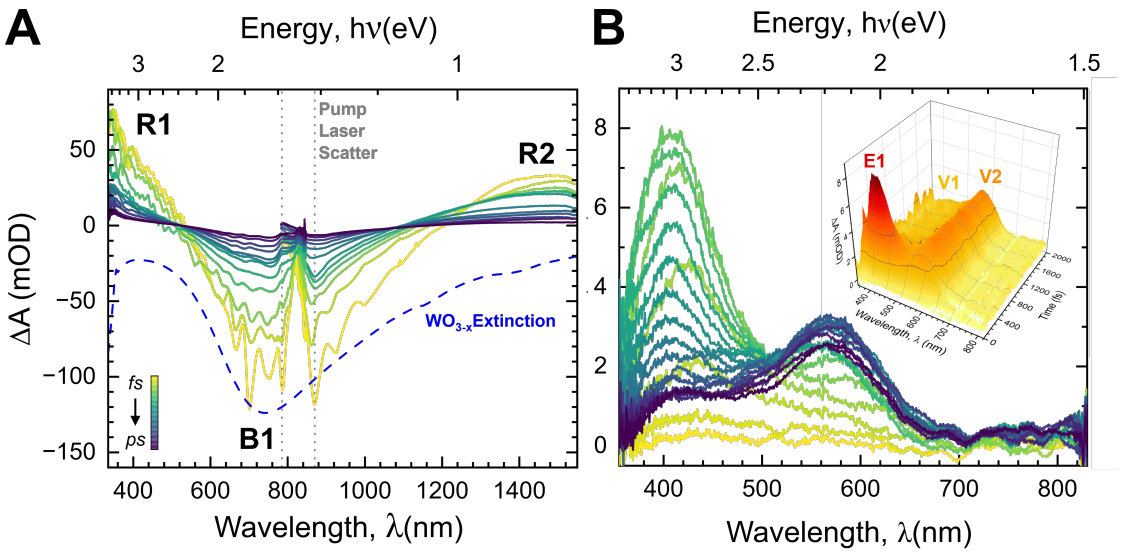

Figure 2.8: Femtosecond hot carrier equilibration dynamics of $WO_{2.76}$ pumped at 1.65 eV

(**A**) Femtosecond hot carrier equilibration dynamics of $WO_{2.76}$ pumped at 1.65 eV. UV-vis probe and NIR probe are performed to observe hot carrier relaxation dynamics. Combined, the spectrum reveals dynamics for both hot holes and electrons, where the ¿ 3.65 eV PIA, 1.65 eV GSB, and 1.20 eV PIA are attributed to interband transitions of hot electron to VB, plasmon ground state bleach, and intraband transitions of hot electrons to hot holes respectively as R1, B1, and R2. All features show rapid equilibration of hot carrier population after Landau damping (¡100 fs), leading to dominating electron-phonon, phonon-phonon relaxation pathways. (**B**) Femtosecond $E_{g,opt}$ dynamics for 3.8 eV pumped WO_{3-x} shows three features of interest. (E1) The shortest-lived, high-energy feature at near 3.0 eV is attributed to rapid exciton formation and trion recombination. (V1, V2) Two longer lived features which slowly grow in between 3.0 – 2.2 eV are attributed to excited state oxygen vacancy population before eventual emission. Inset shows the same data in a 3D plot for easier visualization.

intra- (R2) band population following Landau damping which generates a non-thermal distribution of carrier population in the CB.[67] The B1 bleach is attributed to depopulation of the ground state LSPR extinction. In Table 2.2, the decay kinetics for the three features are listed for the two relaxation dynamic regimes. The dynamics of the plasmon bleach (B1) and hot carrier states (R1 and R2) are fit to a biexponential attributed to contributions from electronic relaxation (electron-phonon, el-ph) and thermalization (phonon-phonon mediated energy dissipation, *ph-ph*) scattering processes, consistent with previous literature of temporal plasmon dynamics.[90,113] A 3D plot, temporally separated spectral data, and the white light continuum are available for viewing in Figure 2.9 and 2.10.

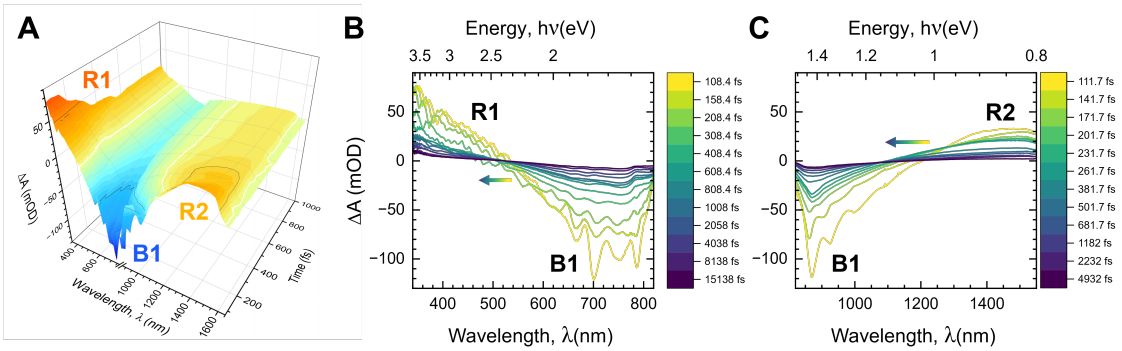

Figure 2.9: Additional Spectral Plots of LSPR Pumped fsTA Data

(**A**) Qualitative and (**B, C**) quantitative spectral plots of LSPR pumped fsTA data, where precise times of spectra are given per color and a general shift from low to high energy is observed between R1/B1 and B1/R2 features. The first $\tilde{3}00$ fs observed are attributed to instability of the white light probe spectrum interacting with the WO_{3-x} LSPR.

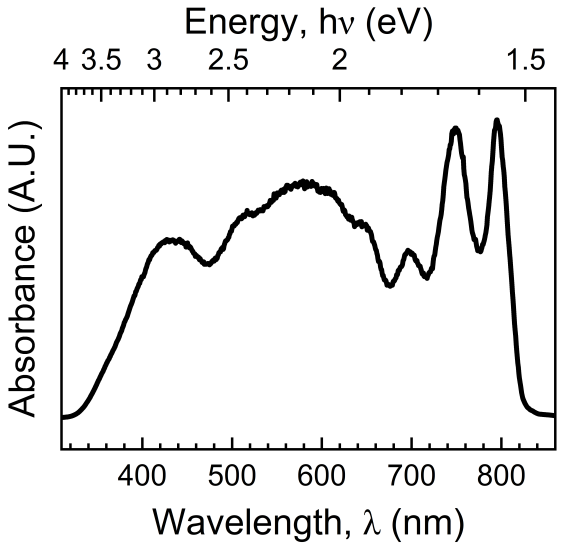

Figure 2.10: fsTA White Light Probe Spectrum

fsTA white light probe spectrum of the CNM system

In Figure 2.11, a proposed model delineating the carrier dynamics for $WO_{2.76}$ is shown for selectively exciting the LSPR and $E_{g,opt}$. As shown in Figure 2.11A, LSPR pumping results in hot carriers generated through Landau damping subsequently relaxing into interband (R1) and intraband (R2) levels coupled to LSPR (B1). Based on the intersection of R1 and B1 transitions, an electronic band gap of approximately 2.4 eV is assigned based on the 0 ΔA crossing at long time

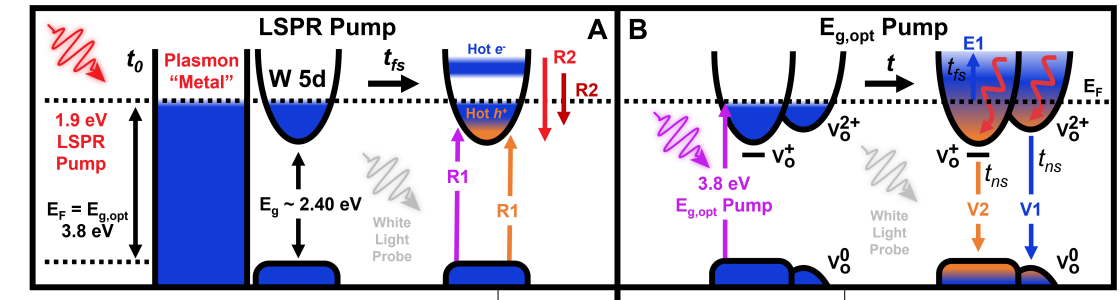

Feature, Identification	Energy (eV)
R1, Interband Relaxation	3.65 – 2.25
R2, Intraband Relaxation	1.10 – 0.80
B1, LSPR Ground State Bleach	1.65

Feature, Identification	Energy (eV)
E1, Excitonic Trion Recombination	3.00
V1, V_O^{2+} -> V_O^0 Relaxation	2.92
V2, V_O^+ -> V_O^0 Relaxation	2.20

Figure 2.11: Carrier Relaxation Pathways for $WO_{2.76}$ PSNCs

(**A**) Hot carriers generated by plasmon excitation relax through the $WO_{2.76}$ semiconducting electronic structure, observable through R1, R2, and B1. After Landau Damping, hot electrons and holes undergo various relaxation processes and pathways which range in energy dependent on the transition dipole probability of interband and intraband transitions. (**B**) After direct $E_{g,opt}$ excitation, no hot carriers are observed, and instead trion type exciton formation and relaxation occur through E1, while V_O trap recombination is expected for V1 and V2 terms. The range of R1 and R2 (3.65 and 0.80 eV respectively) are constrained by the detection limits of the instrument.

(4.8 ps), where the lowest energy interband transition is expected to occur during *ph-ph* relaxation. The maximum is above the limit of the detector (> 3.65 eV) limiting the assignment of the R1 energy maximum. The assigned electronic band gap energy is also in relative agreement with previous computational predictions for tungstate systems.[114] The boundary between B1 and R2 showcases a maximum interband transition of 1.10 eV, representing the maximum energy difference between the hot holes and electrons, while the smallest energy difference is less than 0.8 eV due to NIR detector limitations. Ultimately, these transition energy ranges support the assertion that the nanocrystal electronic band structure plays a critical role for hot carrier relaxation dynamics in plasmonic semiconductor nanocrystals.

In Figure 2.11B, the excited state relaxation processes following $E_{g,opt}$ excitation is dominated by exciton recombination events not involving plasmon induced hot carriers. Combining results from both PL and fsTA, the femtosecond excitonic feature precedes exciton trapping at Vd-Va levels

arising from V_O state. The V_O^{2+} (V1) is believed to be associated with the observed power-law type PL, while V_O+ (V2) relaxes non-radiatively.

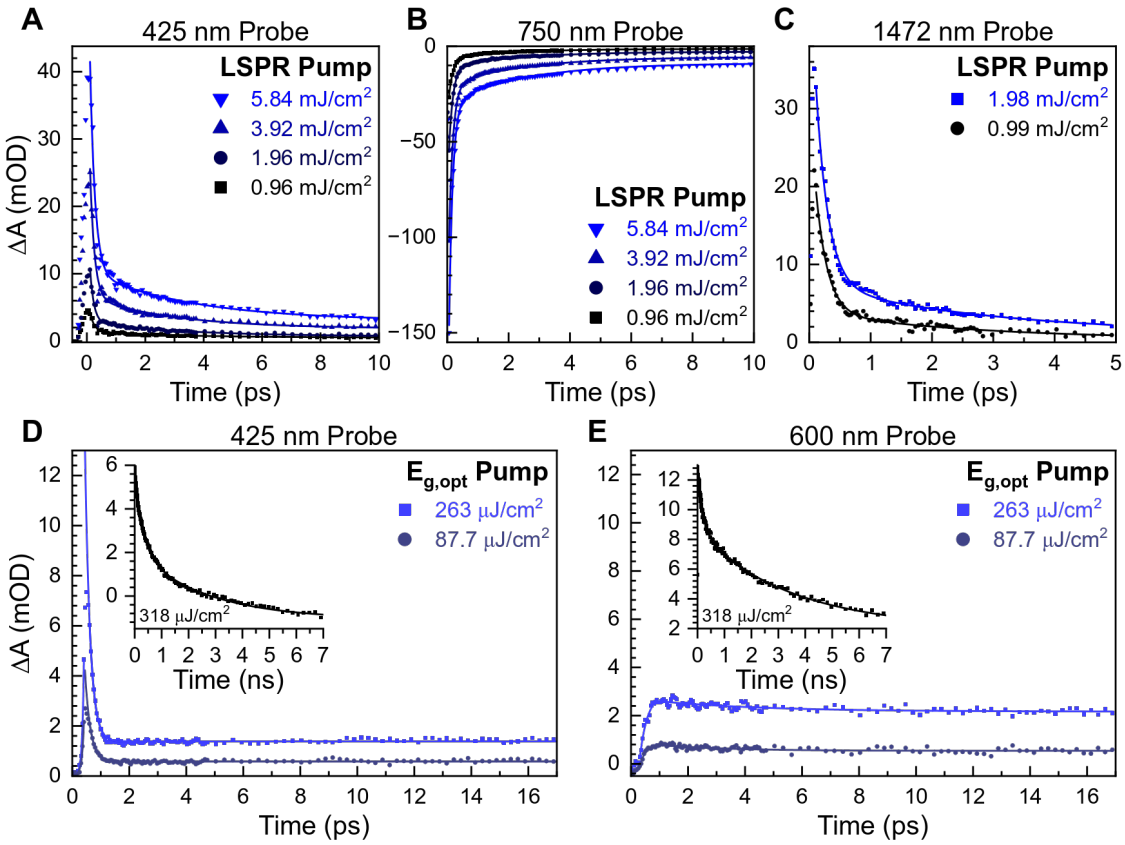

Figure 2.12: Kinetics of $WO_{2.76}$ fsTA spectral features

Time dependence of fsTA spectral features under 800 nm, LSPR pumping at (**A**) 425, (**B**) 750, and (**C**) 1472 nm probe wavelengths with bi-exponential fits. fsTA following excitation of the optical gap at 325 nm, $E_{g,opt}$ is also monitored at (**D**) 425 and (**E**) 600 nm probe wavelengths. The transient signal shows drastically different decay dynamics with long, ns time dynamics shown in the insets for both probe wavelengths.

Pump fluence dependent transient decay spectra for R1, R2, and B1 pumped on resonance with the LSPR frequency are presented in Figure 2.12A-C respectively while the extracted lifetimes are provided in Table 2.2 and plotted in Figure 2.13. Pump fluence is calculated according to the equation, fluence $= \frac{E}{A}$, where $E = \frac{\text{power (W)}}{\text{repetition rate (Hz)}}$ and A is the beam spot size in cm^2. Excitation power dependent TA results indicate only B1 is observed to be strongly fluence dependent, as the rate of bleach recovery for thermalization is known to increase with increasing fluence.[115]

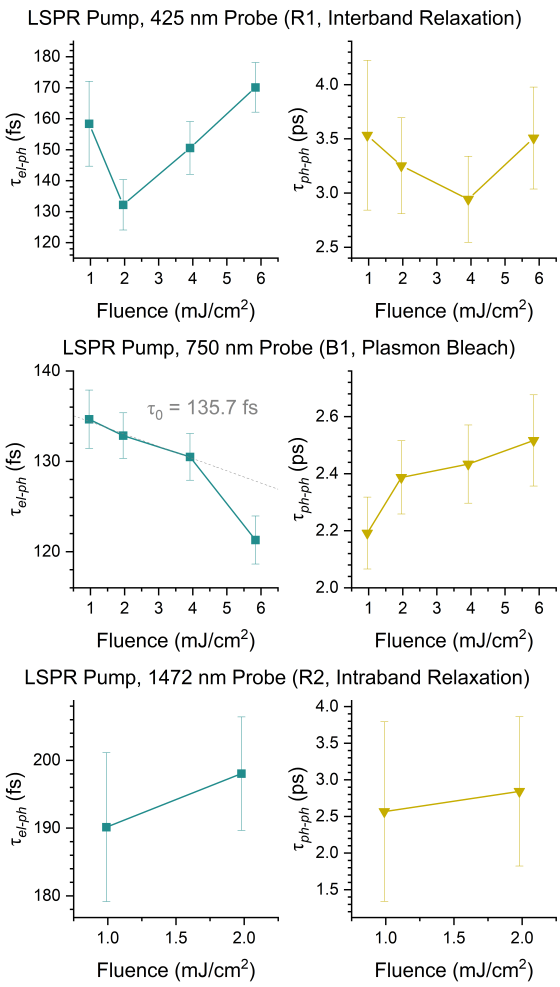

Figure 2.13: Lifetime Fluence Dependence of the LSPR Pumping regime for $WO_{2.76}$

Lifetime Fluence Dependence of the LSPR Pumping regime at 425, 750, and 1472 nm Probe Wavelengths for *el-ph* and *ph-ph* relaxation dynamics. The *el-ph* dynamics for B1 are used to extract the zero fluence lifetime parameter of 135.7 fs and used in the calculation of electron-phonon coupling constant, G.

B1 features the fastest recombination rates for both *el-ph* and *ph-ph* scattering processes, and this correlates with the recovery of the ground state extinction of the $WO_{2.76}$ LSPR. The feature assigned as R1 has the longest *ph-ph* lifetime and R2 has the longest *el-ph* lifetime. The observed bleach, B1, exhibits fluence dependence with an increase in the energy dissipation represented by the ps lifetimes as power increases, while the *el-ph* lifetime decreases with increasing power. It is hypothesized that the fluence dependent behavior is a result of increased hot carrier production

resulting in an overall decrease in the mean free path for *el-ph* scattering, and thus shortening the lifetime. However, as more energy is dumped into the lattice, *ph-ph* relaxation is expected to increase due to the increase of probability of energy transfer from thermalized carriers into the lattice. When holistically comparing R1 and R2 versus B1, the difference in lifetimes suggests there is a coupling parameter between the band structure and hot carriers as suggested previously,[98] otherwise R1 and R2 lifetimes would be nearly identical to B1.

Table 2.2: LSPR Pumped (800 nm) relaxation rates obtained at a fluence of 1.96 mJ/cm^2 for UV-Vis Probe Lifetimes.[i]

LSPR Pump Feature (Energy)	**electronic relaxation (τ_{el-ph}, fs)**	**thermalization (τ_{ph-ph}, fs)**
R1 (2.92 eV)	132.2 ± 8.1	3.25 ± 0.44
B1 (1.65 eV)	132.9 ± 2.5	2.39 ± 0.13
R2 (0.84 eV)	198.0 ± 8.4	2.84 ± 1.02

From the fluence dependence of B1, it is possible to extract the electron-phonon coupling constant, as reported in previously for WO_{3-x}.[116] When the LSPR is excited, a rapid transfer of energy from hot carriers to the lattice occurs due to their difference in electronic temperature, leading to a significant increase in temperature. Such values can be used for further analysis such as the two-temperature model which takes the differences in temperature to account and provides a way to calculate the thermal response of the material under light excitation. The electron-phonon coupling constant provides a measure of the thermalization behavior, which is important for applications susceptible to thermal damage.[117] Following from the work of Johns, *et al.*, the electron-phonon coupling constant, G, can be calculated using Eqn. 2.2 and Eqn. 2.3:

$$\tau_0 = \frac{\gamma T_0}{G} \tag{2.2}$$

$$\frac{\gamma_{\text{real},1}}{\gamma_{\text{real},2}} = \frac{m_1 \sqrt[3]{n_{\text{e},1}}}{m_2 \sqrt[3]{n_{\text{e},2}}} \tag{2.3}$$

From the fluence dependence for B1 (Figure 2.13), the parameter τ_0 (*el-ph* decay rate at zero fluence) is extracted using a linear regression of the three lowest fluences (grey dashed line), assuming a temperature of 298 K for the surroundings of the nanocrystal (T_0) and compared with

[i]For the NIR probe, R2 is pumped with a fluence of 1.98 mJ/cm^2

previous literature in Table 2.3. The results from Johns, *et al.* on WO_{3-x} are very comparable to this work, the primary difference likely due to the observation of a lower τ_0, either due to the lower pulse width capabilities of the fsTA resulting in a more accurate value, or to the much higher plasmon frequency for this WO_{3-x} sample resulting in higher carriers, and higher *el-ph* coupling.

Table 2.3: TTM Model parameters obtained from fluence dependence of B1

	γ **(J K^{-2} cm^{-3})**	G **(J K^{-1} s^{-1} cm^{-3})**
B1 (this work)	6.69×10^{-5}	1.47×10^{11}
Johns, *et al.*	5.50×10^{-5}	9.64×10^{10}

In Figure 2.8B, the TA results are shown for direct excitation of $E_{g,opt}$ (3.8 eV) at low fluence (263 μJ). Low power prevents ligand dissociation from the nanocrystal surface and two-photon effects. In the TA spectra, three distinct absorption features are observed and labelled E1, V1, and V2. The observed dynamics for E1, V1 and V2 are visualized in Figure 2.12D,E and compiled in Table 2.4. The long nanosecond lifetimes for V1 and V2 were obtained separately at a power of 318 μJ/cm^3 shown in the inset of Figure 2.12D,E.

The exciton Auger recombination is assigned as E1 at 3.02 eV nm. The E1 feature decays on the femtosecond timescale commensurate with the appearance of V1 and V2 at 2.92 and 2.19 eV respectively, which decay on the nanosecond domain. It is difficult to deconvolute E1 and V1 from each other due to energy overlap; however, the rapid growth and decay dynamics can be obtained from E1 while the longtime decay can be obtained for V1 at 2.92 reflecting the longer lifetime for V1. V2 is separately monitored at 2.07 eV for its growth and decay dynamics with minimal convolution from E1 and V1.

Table 2.4: $E_{g,opt}$ Pumped (3.8 eV) UV-Vis Probe Lifetimes

$E_{g,opt}$ **Pump Feature (Energy)**	**Growth** (τ_{growth}, **fs**)	**Decay** (τ_{decay}, **fs**)	**Decay** (τ_{decay}, **ns**)
E1 (2.92 eV)	58.6 ± 1.8	177.5 ± 4.1	
V1 (2.92 eV)			2.68 ± 0.19
V2 (2.07 eV)	273.5 ± 52.8		3.50 ± 0.26

Based on literature precedence for n-type semiconductor exciton recombination dynamics,[117] E1 is assigned to trion recombination between excitons and free electrons while V1 and V2 represent

the growth of two long-lived acceptor-donor state populations associated with trapping at V_O sites forming a trapped polaron, analogous to an f-center in oxides.[118] The energy of the V1 state is consistent with a transition from a V_O^{2+} acceptor level to V_O^0 donor level, as previously reported.[110] V_O^{2+} -¿ V_O^0 is a two electron process which requires either a W^{5+}-V_O^0-W^{5+} or W^{4+}-V_O^0-W6+ bonding configuration, and is likely to account for the 3.1 eV emission observed.[58] The nanosecond lifetime of V1 and V2 are similar in timescale to the observed power-law behavior in the PL emission in Figure 2.2B. The V2 state at 2.19 eV is attributed to the V_O^0 donor state to V_O+ trap center transition.[119] There is no PL observable for this V_O transition, likely due to Auger-type recombination due to the high electron density from the LSPR on resonance with the V_O+ -¿ V_O^0 transition energy near the Fermi level. When compared to the LSPR pumped series (R1, R2, and B1), the E1, V1 and V2 features are clearly distinct and do not display bi-exponential decay behavior.

2.5 Conclusions

Based on the TA dynamic studies and the proposed scheme for carrier relaxation, $E_{g,opt}$ pumped transitions originate from the electronic band structure of WO_{3-x} itself, without interaction of the visible LSPR. Our findings support that the LSPR is a resonance state which requires direct excitation to access, implying that plasmonic semiconductor oxides can be utilized for their semiconducting properties and plasmonic properties separately or in tandem. Exciting $E_{g,opt}$ directly allows access to the electronic band structure through pathways unique to the semiconductor band structure without hot carrier activation. Using femtosecond TA, this work thoroughly explores hot carrier dynamics in $WO_{2.76}$ plasmonic semiconductor nanocrystals as a model system for other n-type plasmonic transparent conducting oxide type systems. Hot carriers are observed to form only under LSPR pumping and observed to relax through both inter- and intraband pathways. Excitation of the optical band gap leads to trion recombination and emissive pathways due to donor and acceptor level transitions such as V_O's. This study shows Landau damping induced carrier formation following LSPR excitation leads to identifiable relaxation processes in WO_{3-x}. Defective tungstate, a plasmonic semiconductor, is observed to have a carrier density approaching noble metals such as gold, and hot carrier relaxation lifetimes are on similar timescales. The observation of hot carriers in WO_{3-x} suggests this may be a more economic material for application towards hot-carrier enhancement in integrated devices where gold is normally used to improve device ef-

ficiencies.[88] This work gleans into the possibility of future plasmonic semiconductor nanocrystals which could be engineered for dual excitonic/plasmonic based applications simply by changing the energy of incident photon energy.

CHAPTER 3

IRON INTERMEDIATE BAND GOVERNS RELAXATION KINETICS OF BORNITE PLASMONIC SEMICONDUCTOR NANOCRYSTALS

3.1 Abstract

Intermediate band (IB) plasmonic semiconductor nanocrystals of Cu_xFeS_4 (x=3,5,7) are investigated by femtosecond transient absorption (fsTA) to correlate the observed LSPR damping behavior with changes in the observed electron-phonon and phonon-phonon relaxation dynamics when excited at the localized surface plasmon resonance (LSPR) and optical band gap ($E_{g,opt}$). Changing the ratio of Cu:Fe results in a shifting of the Fe 3d IB consistent with an isosbestic shift seen for all fsTA data. While different relaxation pathways can be accessed, the Fe intermediate band is critical for both pump regimes, resulting in an increased hole-phonon (*ho-ph*) coupling constant as a function of increased carrier density and carrier effective mass (m^*). Additionally, evidence is provided for a correlation of LSPR m^* and damping versus *ho-ph* and *ph-ph* relaxation respectively by comparing fsTA data with two-temperature modelling which may be used to guide future development of high photothermal or photoacoustic conversion efficient plasmonic semiconductor nanomaterials.

3.2 Introduction

Interest in plasmonic materials are focused on the ability to enhance performance for epsilon-near-zero materials,[120–122] photothermal therapy,[78,123,124], electrochromic windows,[125] telecommu-

nications,[126] infrared neural stimulation,[77,127,128] surface enhanced Raman scattering,[69] refractometric sensing,[129] and photocatalysis[130] by resonantly exciting the LSPR mode. The interest in plasmonic nanomaterials, whether noble metals or semiconductors, reflects the presence of a localized surface plasmon resonance (LSPR) arising from the collective oscillation of free carriers, which results in enhancement of the electric field ($\vec{E}$) in the near field.[70] Noble metals are the quintessential standard for plasmonic nanocrystal research[70,103,131,132] but are typically limited to the visible region.[133] The LSPR of plasmonic semiconductor nanocrystals (PSNCs) are widely tunable across the visible to infrared (IR) spectral region through composition, size,[24,134] doping,[27] and morphology.[25] The strength of the near field enhancement at the surface of a PSNC is dependent on the scattering contributions (surface, phonon, electron, and vacancy scattering). In PSNCs, non-parabolicity of the bands and aliovalent ion incorporation lead to the formation of donor-acceptor states that influence carrier density (n), effective mass (m^*), and carrier mobility (μ) by modulating electron scattering pathways. The presence of donor-acceptor states in PSNCs affects LSPR relaxation dynamics, the electronic density of states, and the applicability of PSNCs as optical materials.

While n-type, direct gap metal oxides dominate the PSNC literature, the p-type Cu_xFeS_4 (x=3,5,7) bornite family, herein referred to as CFS-Cu:Fe (e.g. CFS-3:1), is an example of an intermediate band semiconductor (IBSC) that is plasmonic. IBSCs as a class of materials are increasingly being explored for their thermoelectric properties and are typically seen as indirect band gap materials, thought to make them useful towards applications in thermoelectrics and photovoltaics.[135–137] CFS PSNCs are attractive due to low elemental cost, low toxicity,[123,138] and having a biologically transmissive near-IR (NIR) plasmon frequency.[78] In CFS, the intermediate bands are composed of Fe d-orbitals that are empty due to hole doping. Manna and coworkers evaluated the relaxation processes in nanocrystal $CuFeS_2$, a related Cu-Fe-S phase having the chalcopyrite instead of the bornite structure, and observed significant photothermal heating is caused by the Fe IB.[139] Lee *et al.* were one of the first to illustrate the oxidative behavior of chalcopyrite to bornite where a high energy dielectric resonance (polaron-like) is observed to unpin and form an LSPR at low energy.[140] While they performed preliminary DFT studies of the electronic band structure for bornite as a function of Fe content, there are still questions as to how light interacts and relaxes through the density of states. While similar classes of IBSCs have been

explored such as Cu_3MCH_4 and $CuFeS_2$,[139,141,142] literature of bornite, Cu_5FeS_4, is still ongoing and has been described as "puzzling".[143] To date, the band structure of bornite is still under active research, where differences in synthetic conditions can modulate the band gap from 0.5 eV to 1.25 eV between valence band (VB) and IB.[144,145] Overall, the results from literature point in the direction that Fe content in the Cu-Fe-S system should directly influence the energy and population of IB states, leading to differences in relaxation dynamics.

In InN, it has been observed that simultaneous changes in m^* with n occurs, leading to the observation that LSPR frequency can remain the same even as n is reduced.[48] Furthermore, m^* is directly impacted by changes in the carrier-phonon interaction in a given material and can change with size as demonstrated in CdSe quantum dots.[146,147] Understanding how the value of n, m^*, and τ are influenced by PSNC composition is critical for tailoring the physical properties of PSNCs for future electronic and photonic applications. The LSPR frequency in CFS can be modeled using the simplified Drude model, wherein the plasma resonance frequency (ω_p) (Eqn. 3.1)

$$\omega_p = \sqrt{\frac{ne^2}{m^*\varepsilon_0}} \tag{3.1}$$

is assumed to be primarily dependent on both n and carrier effective mass m^*, in which e is the elementary charge of an electron and ε_0 is the vacuum permittivity constant.[39] The reported p-type CFS carrier densities are on the order of 10^{21} to 10^{22} carriers based on one-electron reductant chemical titration of the LSPR extinction centered at $\tilde{9}600$ cm^{-1}. The change in the LSPR with Cu:Fe ratio is caused by a simultaneous modulation of n and m^* validated by chemical titration comparison to Drude model fitting of the LSPR in the 3:1, 5:1, and 7:1 compositional series.[38] The modulation of m^* is consistent with the observation of Fe vacancy population changing with Cu:Fe ratio, as evidenced by repeated observations of Fe leeching.[38,140,148] The impact of Fe vacancies is hypothesized to lead to subsequent hole pinning and polaron type carrier coupling, thus increasing the overall m^* for CFS dependent on the degree of vacancy presence and strength of carrier coupling. The effect of m^* is not only impactful on the fitting of LSPR, but it also plays a critical role in carrier mobility, μ (Eqn. 3.2),

$$\mu = \frac{e\tau}{m^*} \tag{3.2}$$

where τ is scattering lifetime, which is impacted by carrier coupling, crystal structure defects, interstitial sites, and surface depletion effects for PSNCs.[27,149–151] While μ is difficult to measure directly in a nanocrystal, the change in LSPR relaxation dynamics provides an indirect assessment of changes in the carrier mobility with changes in Fe vacancy content. The ability to modulate the Cu:Fe ratio in CFS allows the evaluation of n, m^*, and μ in a single lattice structural type to be evaluated.

In this work, femtosecond transient absorption (fsTA) is used to explore the relationship between n, m^*, damping, and the relaxation kinetics of CFS-3:1, CFS-5:1, and CFS-7:1 in the bornite phase for optical band gap ($E_{g,opt}$, CB to VB) versus LSPR excited pathways. Phonon-phonon (*ph-ph*) relaxation of hot holes is shown to linearly depend on LSPR damping, while hole-phonon (*ho-ph*) relaxation is observed to correlate with changes in m^* which are validated with variable field magnetic circular dichroism measurements. Additionally, the fluence-dependent measurements shed light on the interplay between carrier mobility, carrier density, and relaxation lifetimes with respect to the hole-phonon coupling constant. The Fe intermediate band is shown to play a critical role in the availability of relaxation pathways for CFS agnostic of excitation energy and can be identified by noting similarities in relaxation kinetics between LSPR and $E_{g,opt}$ pump regimes. As Fe content decreases, n and m^* simultaneously increase, resulting in improved carrier mediated thermal conductivity which may be responsible for the enhanced performance of CFS in applications such as photoacoustic imaging and photothermal therapy.

3.3 Materials and Methods

Materials. 1-dodecanethiol (DDT, $\geq$ 98%), oleic acid (OA, technical grade, 90%), n-Hexanes ($\geq$ 98.5%), and oleylamine (OLA, technical grade, 70%) were purchased from Sigma-Aldrich.

Synthesis of CFS Nanocrystals. CFS is synthesized as specified in prior literature.[47] CFS PSNCs with various copper to iron ratios were synthesized by hot injection in a three-neck flask under inert atmosphere. Briefly, a total of 1.2 mmol of Cu(acac)2 and Fe(acac)3 were dissolved in 6.7 mL oleic acid. After heating to 180 ℃, 1.5 mL of dodecanethiol was injected, followed by a drip injection of sulfur in oleylamine (0.2 M, 15 mL) over 5 min, with a subsequent 5 minutes of annealing before cooling and pumping into a glovebox. From the glovebox, samples are redispersed in hexanes and centrifuged at 11267 rcf, 12 ℃for 8 minutes to remove insoluble byproduct. The

supernatant is preserved and transferred to a new test tube, where ethanol is added as an antisolvent to precipitate particles and centrifuged at 11267 rcf, 12 ℃for 20 min to ensure total separation of particles and remove excess ligand.

Extinction Spectroscopy. CFS PSNCs are dispersed in TCE and diluted to achieve an LSPR optical density of approximately 1.0. UV-vis-NIR measurements are conducted using a PerkinElmer Lambda 950 spectrophotometer equipped with a 1 mm NIR optical cell (Spectrocell). Acquired spectra are subjected to baseline correction using pure TCE and normalized to the band edge absorption of the PSNCs.

Femtosecond Transient Absorption. Sample preparation for CFS PSNCs is performed using the same methods previously discussed for extinction spectroscopy. fsTA is performed at the FSU MACLab, where measurements of LSPR and optical band gap pumping are performed. A commercial HELIOS Fire is used, equipped with a Ti:sapphire amplifier with a 1 kHz repetition rate and 100-150 fs pulse width. Pump pulses are generated through an optical parametric amplifier where various doubling crystals are used to obtain the desired wavelength output. A portion on the Ti:sapphire output is used as the probe light after focusing into either a sapphire or CaF_2 crystal to generate white or blue probe light respectively. Probe pulses are mechanically time-delayed using a translation stage and retroreflector. TA spectra are collected on a 1024 pixel CMOS sensor, where all time points are averaged over 1 s, and three reproducible scans are collected and averaged together. Background subtraction and probe chirp correction are conducted for all raw spectra before data analysis. All measurements are performed at room temperature and under ambient conditions.

Computational Details. DFT + U calculations were performed to simulate density of states and band diagrams for CFS-5:1 utilizing the open source QuantumESPRESSO repository version 7.2.[83] A high cubic bornite (Cu5FeS4, ICSD 24174) unit cell was initialized with lattice constants of 5.475 Å, consistent with prior literature.[152] Various plane augmented wave pseudopotentials were used in addition to unrestricted DFT + U, as was used previously for $CuFeS_2$.[139] Self-consistent field calculations were performed on a relaxed structure with a Monkhorst k-point mesh of 6 x 6 x 6 to maximize sampling across the dielectric field of the Brillouin zone.[153] This was followed by a non-self-consistent field calculation of 18 x 18 x 18 for the simulated density of states and band diagram.

Variable Field–Magnetic Circular Dichroism (VH-MCD). VH-MCD was prepared and performed as previously described in literature.[47] Briefly, CFS was prepared by dropcasting CFS in hexanes solution onto a quartz substrate. Poly(lauryl) methacrylate (PLMA) is added as a binder to assist with adhesion to the substrate. Afterwards, VGE-7031 varnish was used to adhere the substrate onto an optical probe for use in the cryostat. VH-MCD is performed on all three Cu:Fe ratios of CFS. An Oxford Instruments 10 T HelioxTL Superconducting Spectromag was utilized along with a Newport Quartz-Tungsten Halogen Lamp (Models 70050, 69931) with a monochromator (Oriel CS260) and optical chopper operating at a frequency of 211 Hz was used in combination with a ThorLabs Glan-Taylor linear polarizer (GLB-10) to linearly polarize incident light, followed by use of a HINDS Instruments photoelastic modulator (PEM-100) for subsequent circular polarization at 47 kHz. A Thorlabs Si Biased detector (DET10A) and InGaAs Biased detector (DET20C2) were used interchangeably to select for visible and NIR regimes respectively and amplified with a Femto current amplifier (LCA-200K-20M). Temperature is monitored and controlled through a Kek-Clamp fiber cable routed through the sample probe and mounted adjacent to the sample substrate. A positive and negative field sweep scan from 0 - 10 T was performed for the bornite samples at 40 K in 2 T intervals. Effective mass is extracted from VH-MCD data by a publically available Python code available at https://github.com/strouselabgithub/strouselab.

3.4 Results and Discussion

3.4.1 Optical and Structural Characterization of CFS PSNCs.

The spherical p-type CFS samples at 3:1, 5:1, and 7:1 copper to iron were prepared as previously reported.[38] The CFS nanocrystals are isolated as nanocrystals passivated by oleic acid and are cubic bornite crystal type. The LSPR frequency for all three samples is located between 1000 to 1100 nm, shifting to lower energy with increasing Cu:Fe ratio, shown in Figure 3.1. The observed composition dependent LSPR shift was previously attributed to a combined change of carrier density and carrier effective mass with CFS-7:1 having both the highest n and m^*, while CFS-3:1 has the lowest n and m^* based on simple Drude approximation (SDA) fitting.[38] The Fermi level (E_F) is observed to be within the valence band in agreement with p-type, hole based LSPR assignment. Additionally, the Fe intermediate bands are adjacent and slightly overlapping with the conduction band. The IB can be broken down into two regimes, IB-II and IB-I with higher and lower energies respectively.

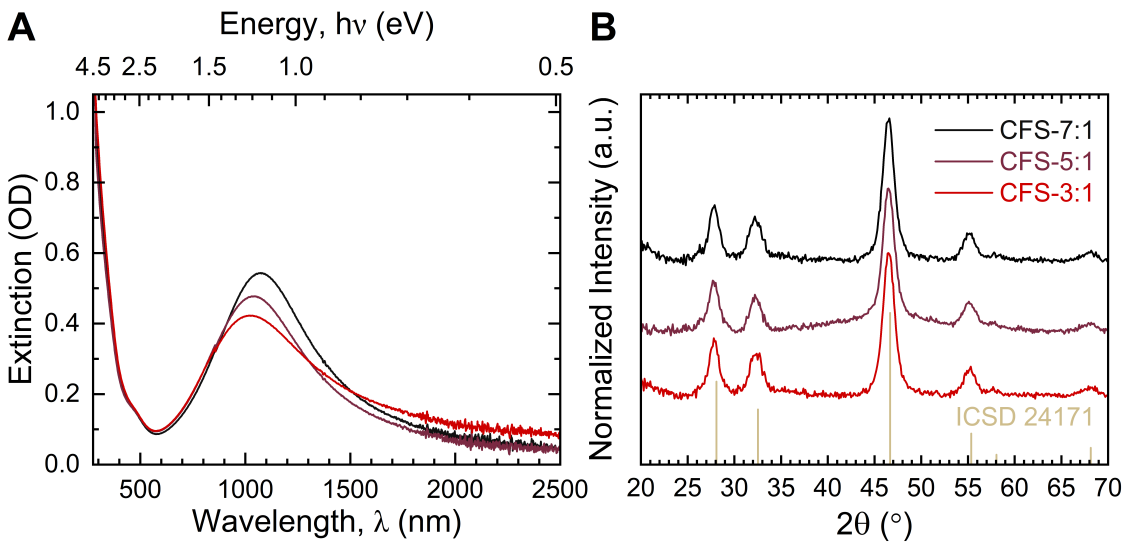

Figure 3.1: **Steady-state Optical and Structural Characterization of Cu_xFeS_4.** (**A**) Relaxation pathways of CFS dependent on pump energy and (**B**) a pictographic representation of how the Fe 3d intermediate band shifts as a function of Fe content. (**C**) Electronic band diagram with projected density of states of the paramagnetic CFS-5:1 unit cell for spin down electrons.

Due to the tetrahedrally coordinating Fe site in bornite, IB-II and IB-I are also assigned as the Fe t_{2g} and e_g levels respectively as previously reported.[47] While the crystallographic structure of the CFS family is identical (Figure 3.1) and each possess an identifiable LSPR, the relaxation dynamics from LSPR excitation are anticipated to differ due to changes in scattering contributions from hole-phonon (*ho-ph*) and phonon-phonon (*ph-ph*) processes, as well as compositionally induced changes to the density of states leading to modification of hot carrier relaxation pathways into the electronic manifold and lattice phonon bath.

The relaxation pathways for LSPR and optical band gap ($E_{g,opt}$) pumped CFS samples are schematically illustrated in Figure 3.2A. As the Fe content in CFS changes, it is expected that intermediate band Fe levels will decrease in energy with respect to E_F, as represented in Figure 3.2B. This also causes the VB to shift lower in energy, resulting in a decrease in hole carriers. The electronic band diagram with projected density of states for paramagnetic, spin down CFS-5:1 is shown for reference in Figure 3.2C with k-space dependence of the bornite IBSC arising from empty tetrahedrally coordinating Fe sites in bornite. The Fe t_{2g} and e_g levels that comprise the intermediate band are herein referred to as IB-II and IB-I respectively identified and assigned as

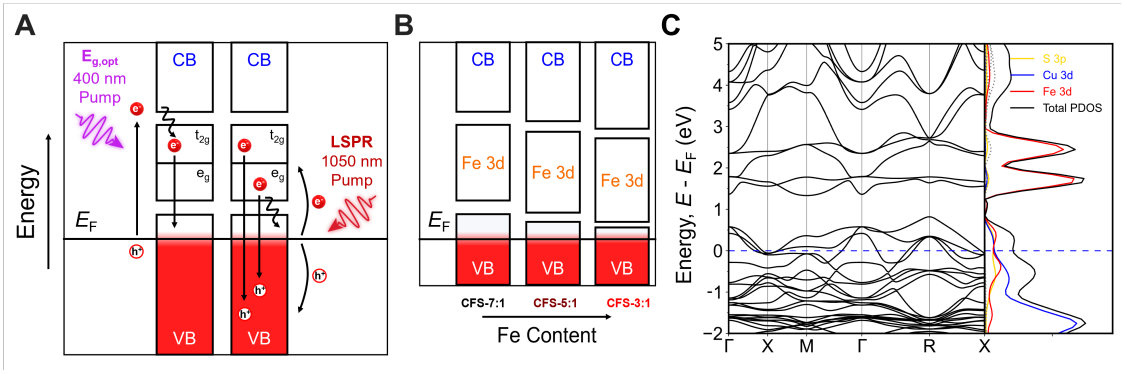

Figure 3.2: **Electronic Characterization of CFS Nanocrystals.** (**A**) Relaxation pathways of CFS dependent on pump energy and (**B**) a pictographic representation of how the Fe 3d intermediate band shifts as a function of Fe content. (**C**) Electronic band diagram with projected density of states of the paramagnetic CFS-5:1 unit cell for spin down electrons.

previously reported.[47,140] As observed in the computational band diagram, the Fe intermediate bands are predicted to be adjacent and slightly overlapping with the conduction band.

In Figure 3.3A-C a color contour plot overlapped with the LSPR extinction spectra for each CFS ratio is shown along with the femtosecond transient absorption spectral map for LSPR (1.18 eV, 1050 nm) and $E_{g,opt}$ (3.1 eV, 400 nm) pump regimes in Figure 3.3D,E. The ground state spectrum can be described by a NIR LSPR mode at $\tilde{1}$100 nm and UV-vis features attributed to optical band gap ($E_{g,opt}$), intermediate band, and ligand passivation layer absorption.

The LSPR pumped fsTA spectra (Figure 3.3D) for the three CFS samples can be deconvolved into three photoinduced absorptions (PIA) and one ground state bleach (GSB). The fsTA spectra are spectrally similar regardless of changing Cu:Fe ratio, but energy shifts observed for all features are consistent with the different shifts in the linear absorption spectra reflecting the shifting Fe IB and LSPR frequency. For all spectra, there is also a small hypsochromic shift occurring over long time, as observed in the TA data for WO_{3-x} PSNCs.[65] The LSPR pumped PIA transitions are assigned to intermediate band relaxation of LSPR generated hot holes from IB-II and IB-I to the ground state, labelled PR2 and PR1, respectively. The GSB is identified as the LSPR bleach due to its matching profile with steady-state extinction spectra and labelled PB. Inspection of the 2D plots show the expected shift in the energy for PR2 and PR1 based on the energy shift of Fe IBs as a function of Fe content, recalling Figure 3.2B. Likewise, PB and the low energy intraband PIA shift proportionally reflecting differences in n and m^*. To verify the assignment of hot hole

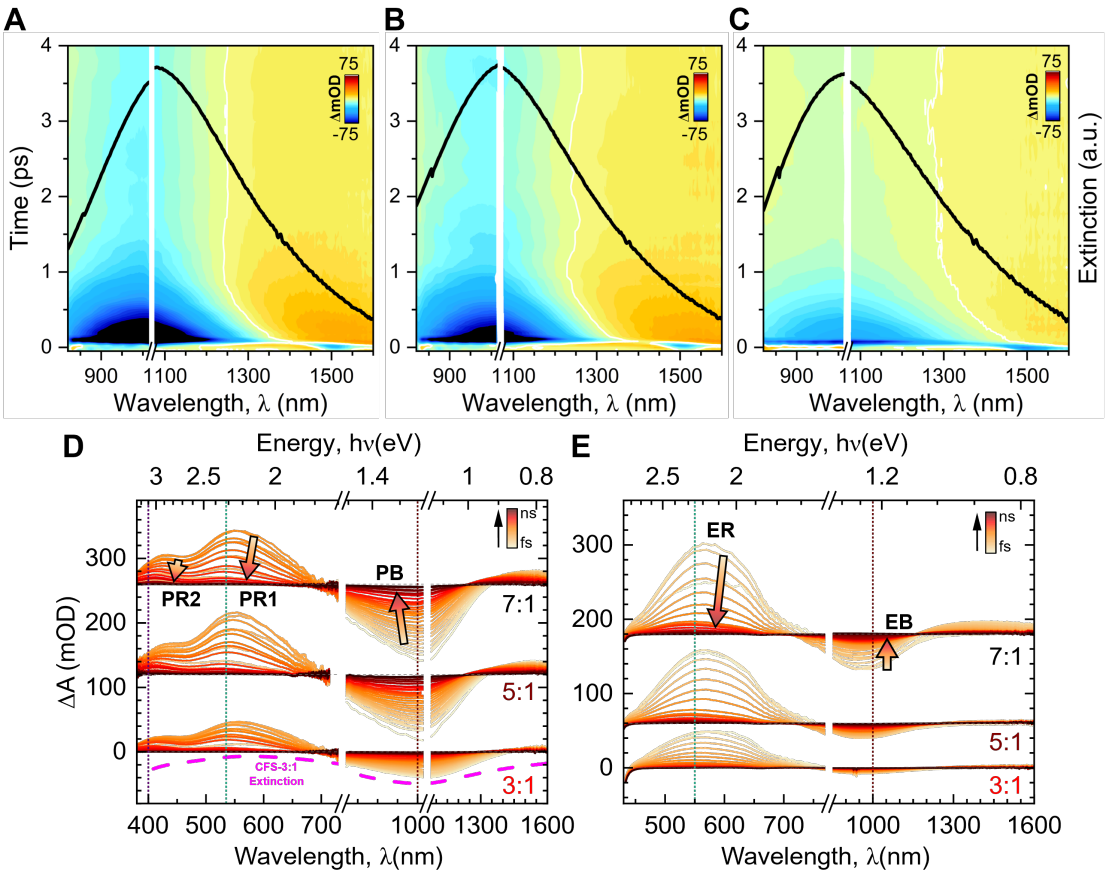

Figure 3.3: **Excited State Dynamics of LSPR and $E_{g,opt}$ Pumped CFS Nanocrystals.** Characteristic two-dimensional transient absorption maps of (**A**) CFS-7:1, (**B**) CFS-5:1, and (**C**) CFS-3:1 with the steady-state extinction spectrum overlayed on top in black and ΔmOD = 0 indicated by a white line. (**D**) LSPR pumped (1.18 eV, 1050 nm) fsTA spectra for Cu_xFeS_4 (x=3,5,7) are compared, all displaying two characteristic PIA features assigned to IB-II (PR2) and IB-I (PR1) relaxation transitions, where the first is observed near 2.9 eV and the second near 2.2 eV. When a near infrared (NIR) probe pulse is used, the LSPR bleach is observed (PB) centered near 1.1 eV, qualitatively matching the LSPR extinction spectrum (pink dotted line). Additionally, intraband PIA transitions are observed for all samples below 1.0 eV. (**E**) $E_{g,opt}$ pumped (3.1 eV, 400 nm) fsTA spectra for all CFS are also compared, all displaying one characteristic PIA feature assigned to a IB-II $\rightarrow$ VB relaxation transition (ER) centered near 2.2 eV. The NIR probe of $E_{g,opt}$ pumped fsTA showcases one GSB assigned to IB-I depopulation (EB) while the low energy PIA is attributed to intraband relaxation.

relaxation for PR2 and PR1, the change in spectral and temporal relaxation dynamics for the PIAs was measured following the addition of a sacrificial reductant, EtOH. The EtOH decay dynamics and kinetics of CFS-3:1 are shown in Figure 3.4. Upon addition of EtOH, a new, broad GSB

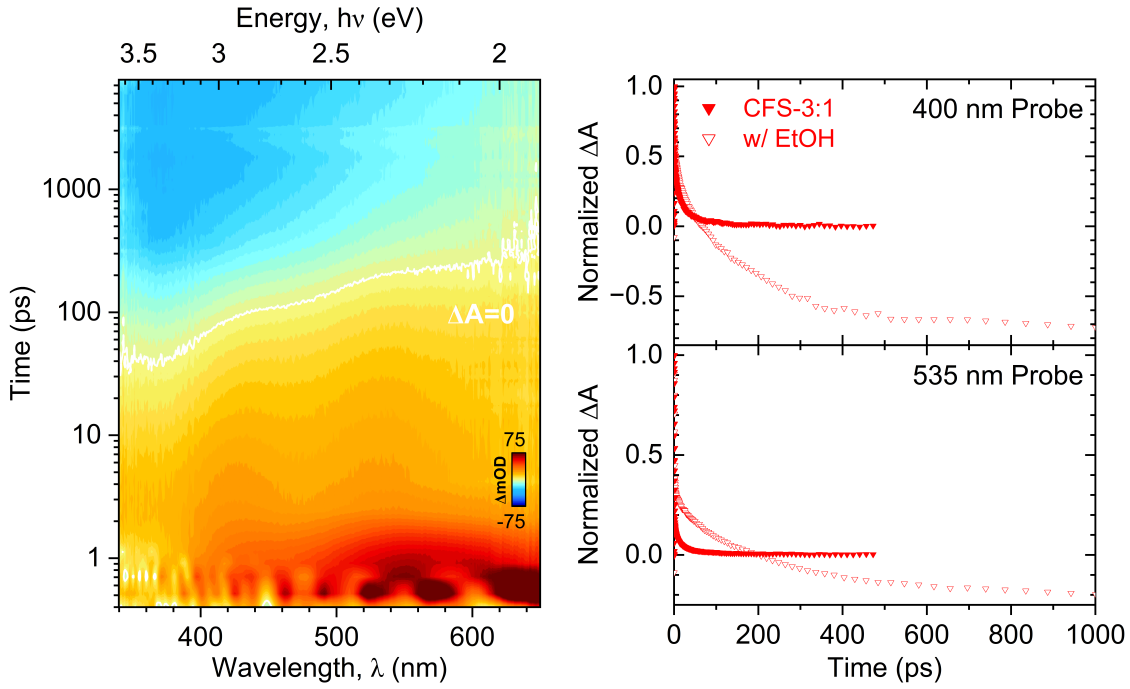

Figure 3.4: **LSPR Pump, UV-Vis Probe for CFS-3:1 with EtOH added.** The 1050 nm pump, UV-vis probe of CFS-3:1. When 25 μL ethanol is added, a long-time bleach is observed, attributed to EtOH scavenging the hot holes after LSPR excitation. All other fsTA features were probed using EtOH as a hole acceptor, and no significant changes in long- or short-time dynamics were observed with addition of EtOH.

growing at long time is assignable to the trapping of hot hole species by EtOH. Trapping of the hot hole prevents the ground state of CFS from fully recovering within 1 ns. The observed response to EtOH is consistent with behavior reported for CuS with the addition of alkanethiol as a hole acceptor, where a long time GSB was also observed at times longer than 20 ps.[154] The kinetics of all other identified features are invariant with the addition of EtOH, meaning that only PR2 and PR1 transitions possess hot enough holes to be captured by EtOH.

Bi-exponential kinetics for the LSPR pumped regime are tabulated in Table 1 while kinetic fits are shown in Figure 3.5A,B. Steady-state LSPR spectral features (plasmon damping (Γ), plasmon frequency (ω_{LSPR}), n, and m^*) are compiled in Table 3.2 based on a previous publication.[38] Observation of bi-exponential decays for LSPR pumped CFS is consistent with earlier fsTA data obtained for ICO, $Cu_{2-x}S$, and WO_{3-x}, where fsTA dynamics are typically identified by a three-step process which includes a $<$ 100 fs carrier-carrier formation called Landau damping, followed

Table 3.1: **LSPR Pumped fsTA Kinetics.** Bi-exponential lifetimes and populations for all identified LSPR Pumped fsTA Features.

1050 nm Pump		Material		
Probe Feature (nm)	**Lifetime**	**CFS-7:1**	**CFS-5:1**	**CFS-3:1**
(PR2) 400	τ_1 (fs)	568 ± 23 (84.2%)	573 ± 76 (79.9%)	641 ± 21 (89.9%)
	τ_2 (ps)	20.2 ± 0.5 (15.8%)	17.4 ± 1.1 (20.7%)	14.3 ± 0.4 (10.1%)
(PR1) 535	τ_1 (fs)	371 ± 6 (98.8%)	387 ± 5 (98.0%)	376 ± 7 (99.5%)
	τ_2 (ps)	20.9 ± 0.6 (1.2%)	19.6 ± 0.5 (2.0%)	13.8 ± 0.3 (0.5%)
(PB) 1000	τ_1 (fs)	434 ± 5.1 (91.7%)	472 ± 8.9 (90.8%)	499 ± 9.1 (93.7%)
	τ_2 (ps)	25.1 ± 1.9 (8.3%)	27.0 ± 3.3 (9.2%)	20.5 ± 3.3 (6.3%)

Table 3.2: **Steady-state LSPR parameters compared with MCD derived m^* data for each CFS.** The steady state measurements were previously reported by Kays *et al.*[38] Asterisk for CFS-5:1 m^* denotes that an interpolation is used assuming a linear relationship between Drude (chemical titration) derived m^* and MCD derived m^*.

Drude Parameters		**CFS-7:1**	**CFS-5:1**	**CFS-3:1**
LSPR Damping[38]	Γ (cm^{-1})	5051.31	5484.71	7490.16
LSPR Frequency[38]	ω_{LSPR} (cm^{-1})	9312	9616	9748
Carrier Density[38]	n (cm^{-3}) $\times 10^{21}$	12.6	10.6	8.51
Drude Effective Mass[38]	m^* ($1/m_e$)	1.63	1.28	1.03
MCD Effective Mass	m^* ($1/m_e$)	2.00	1.74*	1.56

by LSPR electronic relaxation via carrier-phonon scattering, followed by phonon-phonon thermalization undergone within the nanocrystal lattice.[49,65,67,90,154] As CFS features a hole (ho) majority LSPR, the decay dynamics are described as hole-phonon (*ho-ph*, τ_1) and phonon-phonon (*ph-ph*, τ_2) relaxation. Inspection of the lifetime data for the CFS samples in Table 1 reveals that overall, as Fe content increases, τ_1 is observed to increase in lifetime, while τ_2 tends to decrease. The increase in τ_1 is consistent with an overall decrease in both n and m^*, where less scattering centers leads to an increase in mean free path and carrier lifetime and a lower m^* represents less coupling of the carrier to external forces which could cause it to relax faster. PR2 and PR1 have τ_2 lifetimes that are comparable across the CFS series, while PR2 has nearly double the τ_1 lifetime when compared to PR1. In addition, the fractional population of PR2 τ_1 drops significantly (10 – 20%). As IB-I is on resonance with the LSPR, it is expected that free holes localized in IB-I experience an overall greater density of hole scatterers with the concomitant restoration of hole population for the LSPR immediately after excitation, resulting in a faster τ_1 for PR1 compared with PR2. The observed decay dynamics for PR1 τ_2 are strongly correlative with the steady-state LSPR damping (Γ) observed in extinction spectroscopy. The observation of a strong correlation is reasonable, as higher

Γ equates to higher carrier scattering in the PSNC dictated by a combination of bulk, surface, and chemical interface terms.50 Therefore, the observation of faster *ph-ph* relaxation serves as a proxy for γ. This association can also be attributed to the LSPR energy being on resonance with the IB-I intermediate band, and therefore it is likely the most sensitive to the lattice scattering that originates from Fe t_{2g}. While the PR2 transition τ_2 is also correlative, it does not have a strong linear relationship as observed for the PR1 transition.

In Figure 3.3E, the $E_{g,opt}$ fsTA spectra exhibit a similar spectral pattern, however with only 2 PIAs and one GSB. Most notably, there is no evidence of a higher energy PIA in the $E_{g,opt}$ spectra, and the GSB is blue-shifted, centered near 900 nm. The high energy PIA does undergo a long-time hypsochromic shift, however the GSB does not shift in energy, indicating that the transition is fundamentally different from the previously LSPR pumped GSB. The $E_{g,opt}$ pumped regime PIA and GSB are assigned to intermediate band relaxation of IB-II to VB and IB-I bleaching, labelled ER and EB respectively. Although the energy of ER is lower than PB2 by 0.7 eV, it is important to remember that fsTA monitors the energy differences that arise from transitions, and not an energy with respect to E_F or ground state. Because the LSPR generates hot holes and electrons deep within the VB and in the IB respectively, the energy difference that can be achieved between hot hole and electron recombination is much greater than the pump energy limited $E_{g,opt}$ excitation, as illustrated in Figure 3.2A. The 2.2 eV ER transition is the expected energy from E_F to IB-II in Figure 3.2C and is therefore assigned as the IB-II to VB transition.

Table 3.3: **$E_{g,opt}$ Pumped fsTA Kinetics.** Bi-exponential lifetimes and populations for all identified $E_{g,opt}$ Pumped fsTA Features.

400 nm Pump		**Material**		
Probe Feature (nm)	**Lifetime**	**CFS-7:1**	**CFS-5:1**	**CFS-3:1**
(ER) 550	τ_1 (fs)	656 ± 18 (93.0%)	690 ± 20 (92.0%)	747 ± 20 (88.5%)
	τ_2 (ps)	28.1 ± 6.4 (7.0%)	29.3 ± 6.5 (8.0%)	18.5 ± 2.3 (11.5%)
(EB) 1000	τ_1 (fs)	523 ± 20 (90.3%)	594 ± 24 (87.6%)	620 ± 30 (92.8%)
	τ_2 (ps)	24.8 ± 2.8 (9.7%)	36.9 ± 4.9 (12.4%)	15.1 ± 3.1 (7.2%)

The $E_{g,opt}$ pumped regime also exhibits bi-exponential decay kinetics, shown in Table 2 and plotted in Figure 3.5C,D. For the $E_{g,opt}$ pumped regime, the PIA at an energy near the IB-I to VB transition has distinctly different relaxation kinetics than observed in LSPR pumped. τ_1 is comparable to the PR2 transition, as carriers for both processes encounter the same Fe 3d t_{2g} orbital environment while encountering similar kinetic changes with changing Cu:Fe ratio. The IB-II to VB

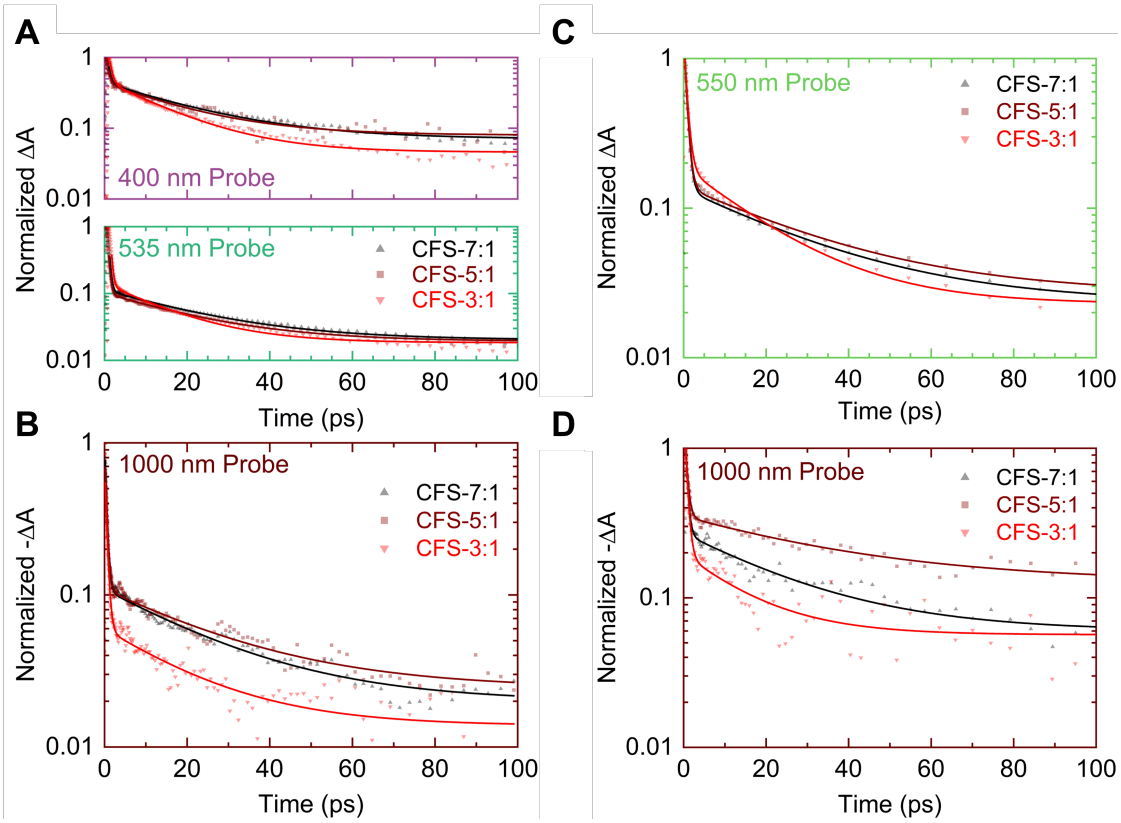

Figure 3.5: **Excited State Kinetics of LSPR and $E_{g,opt}$ Pumped CFS Nanocrystals.** (A) Normalized relaxation kinetics of IB-II (400 nm probe, top, purple), IB-I (535 nm probe, bottom, green), and (B) LSPR bleach (1000 nm probe, red) are examined, where bi-exponential fits are applied to all features for all CFS samples. (C) Normalized relaxation kinetics of IB-II to VB (550 nm probe) are examined, where bi-exponential fits are applied to all features for all CFS samples. (D) Bi-exponential kinetics are shown for the 1000 nm probe which are noticeably different from the LSPR pump regime, where LSPR pump lifetimes are mostly longer for both fast and slow time regimes when compared with the Eg,opt pumped regime.

assignment of ER is supported by noting the increasing isosbestic point as a function of increasing Cu:Fe ratio, where it is expected that the isosbestic energy of ER shifts to higher energy as Fe content decreases, shown in Figure 3.2B. The identity of EB is less straightforward. The observed offset of EB relative to PB in the fsTA data is suggestive of either a photodoping phenomenon previously observed for n-type plasmonic systems due to interband excitation [49,68,120,155] or could be depopulation of the underlying IB-I transitions that is otherwise dominated by the LSPR extinction feature. Considering that at long times the LSPR does not relax to the energy of the LSPR, photodoping seems unlikely in this case, and therefore the assignment of an IB-I bleach transition

is made for EB. ER and EB τ_1s show the same Fe content dependence as the LSPR pumped regime, where lifetime increases with greater Fe content, likely also due to n and m^* changes as discussed previously, as the presence of hole free carriers should still impact exciton recombination.

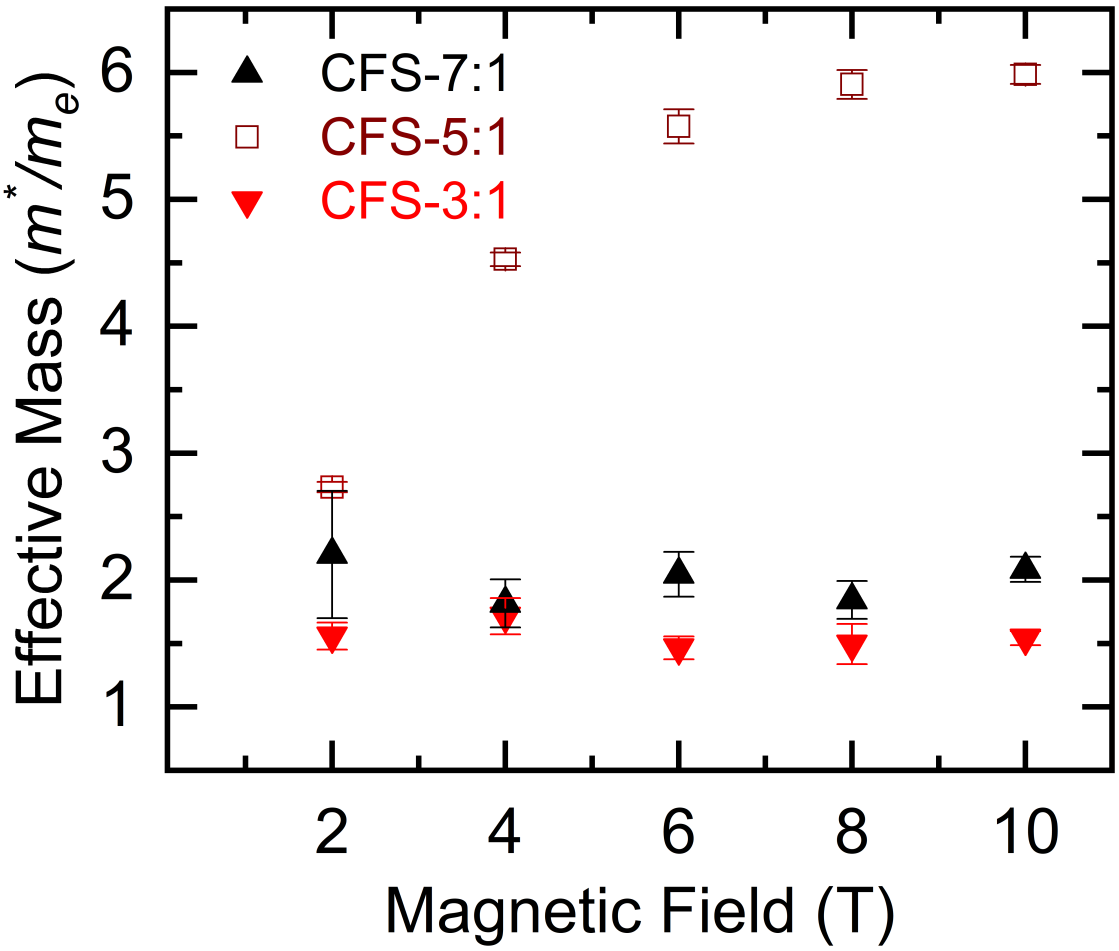

Figure 3.6: **VH-MCD for Experimental m^* Validation.** VH-MCD for all three bornite ratios (CFS-7:1, 5:1, 3:1 from top to bottom respectively) were fit with simulated MCD spectra to obtain a Zeeman splitting energy for all collected fields. CFS-3:1 and CFS-7:1 show no field-dependent m^* behavior and are thus averaged to obtain m^*/me values of 1.56 and 2.00 respectively. (CFS-5:1 data is reproduced with permission from ref.[47])

3.4.2 Evaluating the Correlation Between Static Plasmonic Properties and Transient Relaxation Kinetics.

It is not surprising that a strong correlation between relaxation dynamics and CFS composition is observed. The correlation is anticipated to extend to the m^* values and vide infra to the observed

LSPR damping constant (Γ). Variable field magnetic circular dichroism (VH-MCD) was performed on all CFS to optically probe m^* as a function of applied magnetic field. Details of the fitting procedure are discussed in other works and in the electronic supplemental information.[47]

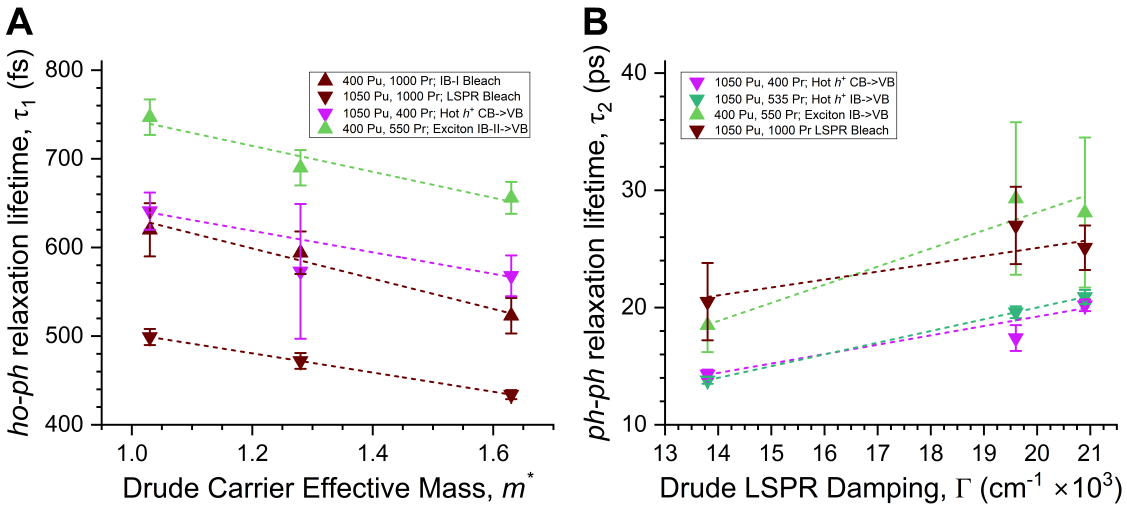

Figure 3.7: **Tracking Drude Properties with Relaxation Lifetimes.** (**A**) Ho-ph relaxation is plotted versus SDA effective carrier mass and (**B**) ph-ph relaxation is plotted versus SDA damping based on data from Kays *et al.*[38]

Figures 3.6 and 3.8 showcase the composition dependent m^* results and raw VH-MCD spectra respectively, where m^* for CFS-5:1 is reproduced from literature.[47] CFS-3:1 and CFS-7:1 display no magnetic field dependent m^* but can be averaged over magnetic field strengths to obtain m^*/me values of 1.56 ± 0.10 and 2.00 ± 0.16 respectively, shown in Figure 3.6. The VH-MCD m^* values track reasonably well with the SDA extracted values with a small scalar difference of 0.5. Table 3.1 compares the simple Drude approximation extracted m^* with MCD obtained m^*. Assuming the linear relationship between CFS samples from the Drude results is consistent with the MCD results, an interpolated m^* of 1.74 is extracted for CFS-5:1, as the magnetic field-dependence of CFS-5:1 prevents a reliable extraction of a zero-field m^* for comparison, but the deviation from experiment may explain why CFS-5:1 deviates the most from some of the linear correlations in Figure 3.7. Interestingly, the deviation in m^* is reminiscent of a previous report where p-type $Cu_{2-x}Se$ m^* from MCD versus bulk was measured to have a similar 0.5 m^*/m_e difference.[22] From these results, it would be worthwhile carefully examining why these copper based PSNCs are repeatedly observed to have some offset from bulk or Drude analyzed results.

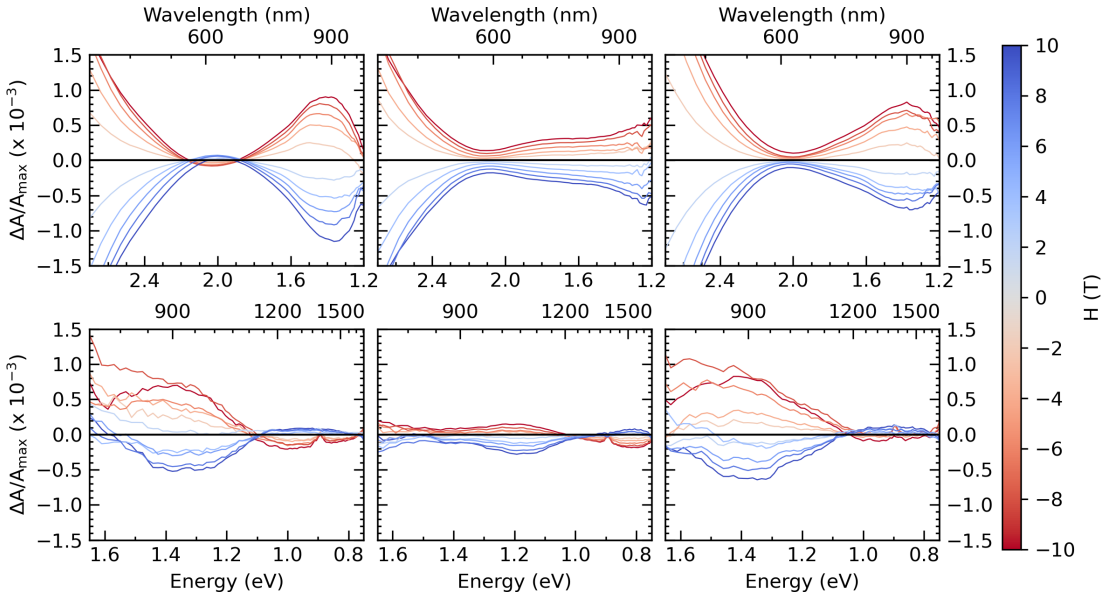

Figure 3.8: **Magnetic Circular Dichroism Measurements of all CFS.** VH-MCD performed for all CFS from left to right, 7:1, 5:1, and 3:1 for visible (**A**, top) and NIR (**B**, bottom) regimes. All MCD spectra are observed to have an asymmetrical A-term like feature between 1.1 – 1.0 eV. The spectral feature observed at 0.9 eV is attributed to a slight transmission dip in Spectrosil B windows.

The free carriers which constitute the LSPR are also descriptive of the electronic properties of the host nanocrystal as well. To this end, a comparison of LSPR m^* and γ can be analyzed relevant to the *ho-ph* and *ph-ph* relaxation lifetimes (Figure 3.7). Remarkably, there is a linear correlation observed for a majority of the relaxation pathways observed for both LSPR and $E_{g,opt}$ pumped regimes. *ho-ph* relaxation tracks with m^* as the mobility of free carriers are directly correlated with their lifetime, as shown previously in Eqn. 3.2. Considering that carrier scattering in this size regime has an up to 49% chemical interfacing damping component,[156] it is unsurprising that *ph-ph* relaxation tracks well with overall LSPR damping due to the coupling of host nanocrystal with surrounding passivating ligands and solvent medium thermalization.

The degree of hot carrier relaxation as a function of CFS composition can be evaluated using the PB fluence dependence. The bi-exponential fits are shown in Figure 3.10 for the power dependent response and lifetimes are plotted in Figure 3.9A. From the fluence dependence, a *ho-ph* relaxation rate at zero fluence (τ_0) can be extracted for all CFS which allows for the calculation of a hole-

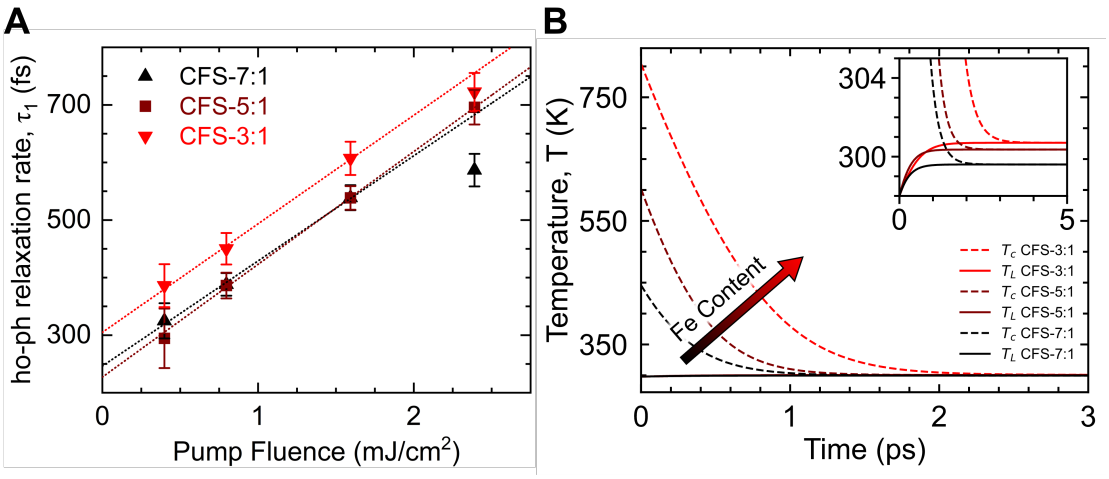

Figure 3.9: **Evaluating the hole-phonon coupling constant, G.** (**A**) Fluence dependent measurements are performed for all CFS samples, where τ_0s are obtained from linear fits of the three lowest fluences. The τ_0s obtained are 304, 227, and 246 fs for CFS-3:1, CFS-5:1, and CFS-7:1 respectively. Once the *ho-ph* coupling constant is calculated using τ_0, (**B**) the TTM is used to compare carrier and lattice temperature as a function of time using 100 μJ/cm^2 photon incidence for all CFS samples. From the model, a clear trend between Fe content and *ho-ph* relaxation is observed where CFS-3:1 is predicted to have the longest *ho-ph* relaxation and greatest lattice temperature increase of all samples.

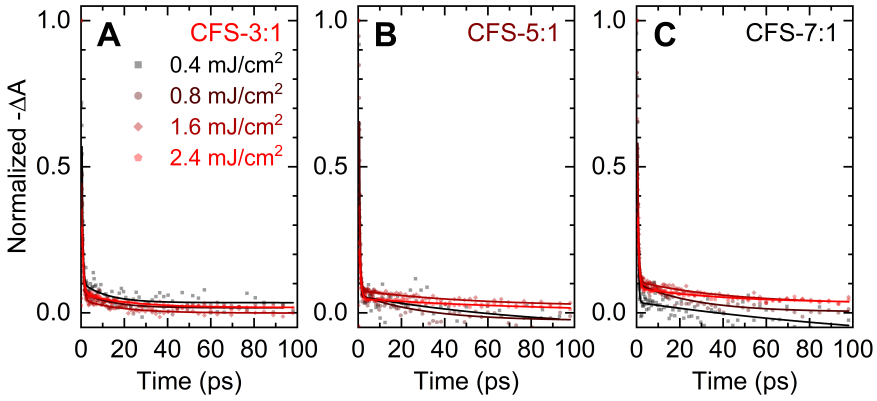

Figure 3.10: **Fluence Dependent Kinetics of LSPR Bleach for all CFS samples.** Fluence dependent fsTA is collected for 1050 nm pumped, 1000 nm monitored (**A**) CFS-3:1, (**B**) CFS-5:1, and (**C**) CFS-7:1 samples.

phonon coupling constant, G, analogous to the electron-coupling constant previously obtained by Milliron and coworkers for plasmonic systems.[116] Using Eqns. 3.3 and 3.4,

$$\frac{\gamma_{\text{real},1}}{\gamma_{\text{real},2}} = \frac{m_1\sqrt{n_{\text{e},1}}}{m_2\sqrt{n_{\text{e},2}}} \tag{3.3}$$

$$\tau_0 = \frac{\gamma T_0}{G} \tag{3.4}$$

G and γ, hole heat capacity, can be calculated by using the known n, m^*, and γ from other plasmonic systems, such as Au or Ag, and are used to calculate γ for CFS in comparison to gold nanoparticles (AuNPs).

Table 3.4: Hole-phonon coupling parameters for CFS samples compared with AuNPs from literature.

Parameter	**CFS-3:1**	**CFS-5:1**	**CFS-7:1**	**AuNPs**[113]
τ_0 (fs)	304	227	246	650
γ (J K^{-2} cm^{-3}) ($\times 10^5$)	3.21	4.29	5.79	5.88
G (J K^{-1} s^{-1} cm^{-3}) ($\times 10^{10}$)	3.14	5.63	7.01	2.70

For all CFS samples, G is observed to be higher than previously measured AuNPs,[113] which may partially contribute to the 5-times signal increase in photoacoustic imaging signal observed by CFS-5:1 compared to AuNPs.[79] Interestingly, as the Fe content decreases, a notable increase in G and γ is observed for the CFS system. This trend reflects the increase in n and m^* as Fe content decreases from CFS-3:1 to CFS-7:1. With greater n, a greater number of hot holes can be produced with LSPR excitation, and thus a greater amount of heat can be dissipated and relaxed through the lattice of CFS nanocrystals. Additionally, with greater m^*, the greater holes couple with the nanocrystal lattice, therefore they can more efficiently conduct heat. Applying the two-temperature model (TTM) to the experimental data provides further insight into the interaction of the CFS hot carriers and the lattice relaxation pathways as reports by carrier and lattice temperature (T_c, T_L). TTM is a popular approach to model plasmonic systems and is performed by solving for a pair of differential equations (Eqns. 3.5 and 3.6),[116,120,157]

$$\gamma T_c \frac{dT_e}{dt} = -G(T_c - T_L) \tag{3.5}$$

$$C_{\text{p}} = \frac{dT_L}{dt} = G(T_c - T_L) \tag{3.6}$$

where C_p is the material bulk heat capacity. For CFS, C_p is calculated by using the room temperature result of heat capacity from Robie *et al.*[158] and converting to units of J K^{-1} cm^{-3} using the density of bornite and the stoichiometric molar mass dependent of Fe content. The G and γ parameters are listed in Table 3.4. As Fe content increases for equal photon absorption and volume fraction, Figure 3.9B shows an increase in the lifetime of *ho-ph* relaxation, analogous to the trends observed in fsTA for τ_1 for all regimes. The long time T_L is shown to have a greater baseline as Fe increases as well, indicative of greater lattice heating, supporting claims by this work and others[139,140,159] indicating that the Fe IB indeed plays a critical role in the photothermal effects of CFS.

3.5 Conclusions

Excitation of the LSPR and $E_{g,opt}$ leads to discrete relaxation pathways as shown in Figure 3.2A. A study on p-type CuS observed a similar bimodal fsTA spectrum with opposite relative intensities.[154] In CuS, an isosbestic points at the edges of their fsTA spectra, and formation of new excited state species after 2 ps was observed. For the CFS materials, we observe no later speciation occurring, rather all excited states appear to decay concomitantly. Additionally, the isosbestic points in this work shift as a function of time from low to high energy, also indicative of hot carrier relaxation as observed previously in WO_{3-x}, shifting within several ps and stabilizing at long time.[65] These observations in CFS points to a different relaxation pathway rather than the S- or ligand-based hole trapping in a defect state lying between CB and VB, as suggested in CuS.[154] Rather, the concomitant decay across the entire spectrum implies that there are no new species formed (i.e. no trap sites), and instead the intermediate band serves as a carrier sink for electronic and thermal relaxation. Consistent with this, the experimental data supports a shift in the intermediate bands as a function of the Cu:Fe ratio, with the Fe 3d IB shifting to higher energy with respect to the CB and E_g.

For the first time, a plasmonic, p-type IBSC system has been investigated for its ultrafast relaxation pathways in the LSPR versus $E_{g,opt}$ pumping regimes. From this work, it is confirmed that the Fe IB plays a critical role in allowing both hot holes and excitonic carriers to relax back to the ground state. The hole-phonon coupling constants for CFS as a function of Fe content were calculated from fluence dependent measurements, where CFS-7:1 had the highest G due to

having the greatest carrier density and carrier effective mass. The TTM was performed from the calculated G and γ parameters, providing additional explanation as to why an increase in lifetime is concomitantly observed with increasing Fe content. Additionally for the first time, a correlation was made between LSPR m^* and damping with *ho-ph* and *ph-ph* relaxation respectively. This work paves the way for further investigation of p-type IBSC materials, where applications that require high m^* such as photoacoustic imaging and photothermal therapy may be further improved.

CHAPTER 4

EFFECTIVE MASS FOR HOLES IN PARAMAGNETIC, PLASMONIC Cu_5FeS_4 SEMICONDUCTOR NANOCRYSTALS

4.1 Abstract

The impact of a magneto-structural phase transition on the carrier effective mass in Cu_5FeS_4 plasmonic semiconductor nanocrystals was examined using magnetic circular dichroism (MCD). Through MCD, the sample was confirmed as p-type with variable-temperature studies from 1.8–75 K. Magnetic field-dependent behavior is observed, showing an asymptotic behavior at high field with an m^* value 5.98 m^*/m_e at 10 T and 2.73 m^*/m_e at 2 T. Experimentally obtained results are holistically compared to SQUID magnetization data and DFT calculations, highlighting a dependency on vacancy-driven polaronic coupling, magnetocrystalline anisotropy, and plasmon coupling of the magnetic field, all contributing to an overall decrease in the hole mean free path dependent on the magnetic field applied to Cu_5FeS_4.

4.2 Introduction

At the nanoscale, plasmonic materials exhibit a strong localized surface plasmon resonance (LSPR) associated with the oscillation of the Fermi level carriers which induces a large electric field at the nanomaterial surface. Noble metals are the prototypical standard for research on LSPR[70,103,131,132] but are typically limited to the visible region.[133] Plasmonic semiconducting nanocrystals (PSNCs) exhibit a plasmon feature that can be systematically tuned from visible to

mid-IR frequencies by controlling the carrier density.[26] The tunability of the PSNC LSPR is advantageous for surface enhanced Raman scattering,[69] refractometric sensing,[129] and photocatalysis.[130] In PSNCs, the frequency of the LSPR is highly sensitive to the number of free carriers and the effective mass of the carriers, as modeled using the simplified Drude model, wherein the plasma resonance frequency (ω_{p}) (Eq. 4.1)

$$\omega_p = \sqrt{\frac{ne^2}{m^*\varepsilon_0}} \tag{4.1}$$

here we calculate to be ASd

is assumed to be primarily dependent on both the free carrier density (n) and carrier effective mass (m^*), where e is the elementary electron charge and ε_0 is the vacuum permittivity constant.[39] The carrier mass is dependent on orbital coupling, will be affected by interband levels, and is impacted by vacancies, surface scattering, and lattice defects. While high surface area in nanocrystals can influence the measured m^*, for simplicity, the carrier mass is typically assumed to be invariant, allowing the plasmon frequency to be predictive of carrier densities. This assumption is reasonable if the only variable is carrier density at a fixed composition and size. The relative difficulty of measuring m^* independently for PSNCs is likely what has led to using the assumption of a constant m^*.[160]

In a recent study, it was demonstrated using carrier titration methods that the Drude model underpredicts carrier levels, most likely due to the assumption that the carrier mass is unchanged by the nano-environment.[161] Incorporating a p- or n-type dopant into a semiconductor leads to changes in the Fermi level, often accompanied by perturbation of the electron-electron and electron-phonon interactions for a simple valence band (VB)-conduction band (CB) energy structure.[162,163] In such systems, the Drude model will produce a linear trend in LSPR frequency with carrier density, as long as vacancies or site occupation changes do not perturb the system. Results from Sn:In2O3 and M:ZnO (M = Al, Ga, In) show the flaw in ignoring the environment at high carrier concentrations, as site occupation effects lead to charge compensation and deviation from parabolic band theory.[32,33] In these studies, the role of a damping term (Γ), as described within the Jung and Pederson model, was proposed to account for the deviation and assumed to be dependent on energy level parabolicity, in analogy to the recently explored InN system.[48] A change in parabolicity will result in a change in carrier effective mass. A perturbation of carrier mass at small PSNCs size is

not surprising, as the carrier mass will be strongly influenced by scattering, vacancies, and changes in band structure due to surface termination of the nanocrystal.[160,164–167] Clearly, independently measuring m^* and n from experimental data is critical to evaluate the plasmonic field effects in PSNCs accurately.

While many of the PSNCs studied to date are binary or doped binary wide band gap materials,[26] a recent report on the ternary, p-type Cu_xFeS_4, otherwise referred to as bornite, has revealed deviation from the simple Drude approximation.[38] Cu_5FeS_4 is an intermediate band semiconductor (IBSC) where Fe d-levels occupy the intermediate band states. IBSC systems are increasingly being explored for their thermoelectric properties. They are typically viewed as indirect band gap materials and are expected to be useful for conversion between heat and electricity, photovoltaics, and LEDs.[135,137,168] The bornite family of PSNCs are of interest for plasmonic systems due to their low elemental cost, low toxicity,[123,138] and a biologically transmissive plasmon frequency that is preliminarily an ideal candidate for in-vivo biomedical applications.[78]

Early studies on nanocrystal bornites have shown the LSPR is invariant with Cu to Fe ratio. It was initially hypothesized that changes in the Cu to Fe ratio would tune the band filling and thus the LSPR frequency, but experimentally this is not observed. However, a significant LSPR frequency shift is observed by chemical titration, indicating the extinction features to be carrier density dependent as expected by the Drude model.[38] The experimental data suggests compensatory effects. These effects differ depending on the Cu to Fe ratio and are predicted through a frequency independent fitting of the Drude model. This results in quantitative damping terms and different effective masses calculated based on the Cu to Fe ratio. Cu_5FeS_4 (5:1) bornite nanocrystals exhibit a magneto-structural phase transition with a complex spin reorientation leading to antiferromagnetic (AFM) interactions.[143] The onset of the transition results in an anisotropic structure that impacts the plasmon properties of this PSNC.

The presence of carriers at an LSPR frequency matching the d-band levels influences the carrier effective mass by changing the electron-electron coupling between the LSPR and d-levels. To date, only limited studies on IBSCs have been reported, such as computational studies on Cu_3MCh_4 (M = V, Nb, Ta; Ch = S, Se, Te)[141,142] and experimental work on $CuFeS_2$[139,159] and Cu_3VS_4.[169] More extensive studies exist for LSPR behavior on Cu chalcogenide direct band gap systems such as $Cu_{1.96}S$ and $Cu_{2-x}Se$.[22,170] The perturbation of the carrier mass in nanocrystals has been reported

in p-type binary chalcogenides. In $Cu_{2-x}Se$ the effective mass is observed to be 0.39 m^*/m_e in bulk. However, 0.89 m^*/m_e is determined for nanodisks,[22] while Cu1.96S is observed to have an effective mass of 0.8 m^*/m_e also for nanodisks.[170] Why the carrier mass is perturbed in a nanocrystal has not been fully investigated, and neither has the impact of interband levels on carrier behavior experimentally. This highlights a large gap in understanding for ISBCs that remains to be filled. This work aims to contribute to filling the gap, as the carrier mass directly impacts carrier mobility for electronic applications and the dampening rate of the plasmon, which affects optoelectronic applications.

In this study, the value of m^* is evaluated for 5 + 1.4 nm spherical, oleic acid passivated Cu_5FeS_4 PSNCs, the stoichiometric bornite. Variable field (+10 T) magnetic circular dichroism (VH-MCD) experiments were performed at 40 K to evaluate m^* in the bornite nanocrystal, supplemented with variable temperature (VT-MCD) experiments from 1.8 – 75 K measured at 10 T on dropcast thin films of the Cu_5FeS_4. Fitting of the VH-MCD spectra revealed a larger than expected m^* for Cu_5FeS_4 of 2.73 m^*/m_e at 2 T. An unexpected change in m^* was observed with increasing field, with a nearly asymptotic value of 5.98 m^*/m_e found at 10 T. The observed value of m^* can be understood by the combined contribution of interband polaronic type coupling to the Fe d-bands, magneto-crystalline anisotropy, and light coupled magnetic anisotropy enhancement caused by direct excitation of the LSPR. The effects reduced the overall mean free path of the hole carriers, thereby resulting in the increased m^* value observed for Cu_5FeS_4. Additionally, magneto-crystalline anisotropy is expected to perturb the electronic and magnetic properties due to a low temperature Cu_5FeS_4 crystal structure.

4.3 Materials and Methods

Copper (II) acetylacetonate ($Cu(acac)_2$, 97%), iron (III) acetylacetonate ($Fe(acac)_3$, $\geq$ 99.9%), 1-dodecanethiol (DDT, $\geq$ 98%), oleic acid (OA, technical grade, 90%), oleylamine (OLA, technical grade, 70%), and poly (lauryl) methacrylate in toluene (PLMA, 25%) were purchased from Sigma-Aldrich. Tetrachloroethylene (TCE, 99.0%) was purchased from BeanTown Chemical. Quartz glass substrates were sourced from GM-Quartz while VGE-7031 varnish was sourced from Lake Shore Cryotronics, Inc. Size #4 gelatin capsules for SQUID measurements were obtained from Electron Microscopy Systems.

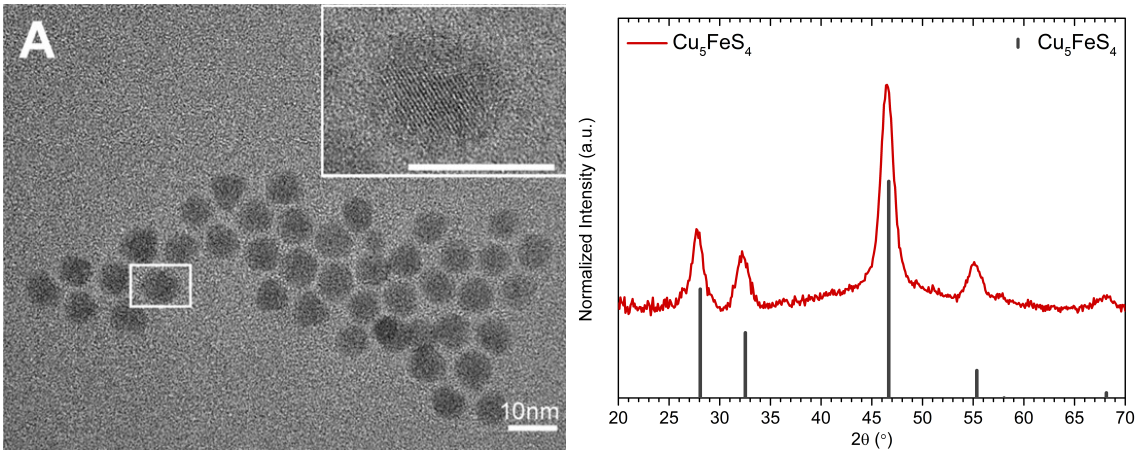

Figure 4.1: Transmission Electron Microscopy and Powder X-Ray Diffraction of Cu_5FeS_4.

Representative transmission electron microscopy (TEM) from Kays et al.[38] (**A**) and powder X-ray diffraction (pXRD) patterns (**B**) were collected using a Rigaku MiniFlex powder X-ray diffractometer equipped with a Cu-Kα source. Samples were dried, powdered, and loaded onto a Rigaku zero-background micropowder plate. Scans were acquired from 20-70° 2θ at a rate of 5°/min and a 0.1° step size. Whole powder pattern fitting and the Halder-Wagner method for Scherrer analysis were completed using the Rigaku SmartLab Studio software and performed for all NCs. The pXRD of Cu_5FeS_4 obtained indicates a good match with the high cubic bulk Bornite phase. (ICSD card number 24174)

Synthesis of Cu_5FeS_4 Nanocrystals. Cu_5FeS_4 PSNCs were prepared following previously reported methods.[38] Briefly, $Cu(acac)_2$ (261.8 mg, 1.0 mmol) and $Fe(acac)_3$ (70.63 mg, 0.2 mmol) (Cu:Fe ratio of 5:1) were dissolved in 6.7 mL of oleic acid in a three neck flask under Ar. After heating the solution to 180 ℃, 1.5 mL of dodecanethiol was rapidly injected, followed by a 5 min drop by drop addition of a solution of sulfur dissolved in oleylamine (0.2 M, 15 mL). The reaction was maintained at 180 ℃for 5 min and cooled to room temperature. The Cu_5FeS_4 was transferred to a glovebox after it had reached room temperature and stored under Ar atmosphere. ICP-MS analysis verified the 5:1 ratio of Cu to Fe. TEM analysis confirms formation of spherical 5 ± 1.4 nm nanoparticles and p-XRD analysis matches the high cubic bornite phase commonly seen at higher temperatures.[152] (Figure 4.1)

Linear Absorption Spectroscopy. Cu_5FeS_4 PSNCs were suspended in TCE and diluted until an LSPR absorption of approximately 1.0 absorbance is obtained. UV-vis-NIR measurements were collected in a 1 cm NIR optical cell (Spectrocell) on a PerkinElmer Lambda 950 spectropho-

tometer. Spectra were baseline corrected using neat TCE and normalized to the band edge absorption of the NCs. Additionally, samples were dropcast onto quartz substrates, checked by the Lambda 950 spectrophotometer at room temperature before cryostat insertion, and scanned via linear absorbance at 40 K within the cryostat.

MCD Sample Preparation. Thin films of Cu_5FeS_4 nanocrystals were prepared by drop-casting the colloidal TCE solution onto a quartz substrate. Poly(lauryl) methacrylate (PLMA) is added as a binder to assist with adhesion to the substrate. Concentration was controlled and monitored by checking the sample substrate using a Lambda 950 UV-vis-NIR spectrometer until an optimal absorbance of approximately 1.0 is obtained. Afterwards, VGE-7031 varnish was used to adhere the substrate onto an optical probe for use in the cryostat.

Variable Field (± 10 T at 40 K) Magnetic Circular Dichroism (VH-MCD). The variable field VH-MCD is performed on the Cu_5FeS_4 sample dropcast onto a 0.5 in quartz substrate. The sample was dried under vacuum prior to insertion into an Oxford Instruments 10 T HelioxTL Superconducting Spectromag. A Newport Quartz-Tungsten Halogen Lamp (Model 70050) with a monochromator (Model 69931) and optical chopper operating at a frequency of 211 Hz was used in combination with a ThorLabs Glan-Taylor linear polarizer (GLB-10) to linearly polarize incident light, followed by use of a HINDS Instruments photoelastic modulator (PEM-100) for subsequent circular polarization at 47 kHz. Two Stanford Research Systems SR830 Lock-In Amplifiers were phase-locked to the chopper and PEM frequencies to maximize the signal-to-noise for the DC detector spectrum (V_{DC}) and ΔA signal (V_{AC}) obtained, respectively.

A ThorLabs biased Si photodetector (DET10A) and biased InGaAs detector (DET20C2) were used interchangeably to select for visible and NIR regimes, respectively, and amplified with a Femto current amplifier (LCA-200K-20M). Temperature was monitored and controlled through a Keck-Clamp fiber cable routed through the sample probe and mounted adjacent to the sample substrate. A positive and negative field sweep scan from 0 - 10 T was performed for the bornite samples at 40 ± 1 K in 2 T intervals. The reported spectra were corrected by subtracting the 0 T scan, to eliminate artifacts from polarization effects, magnetic field inhomogeneity, and other disturbances that may arise during MCD measurement. To confirm polarization of the experimental setup, a 6.2 nm gold nanoparticle solution was compared to a cast film of Au NP measured in the sample cavity of the cryostat versus the fringe field (for reference the field reduction at the outer window

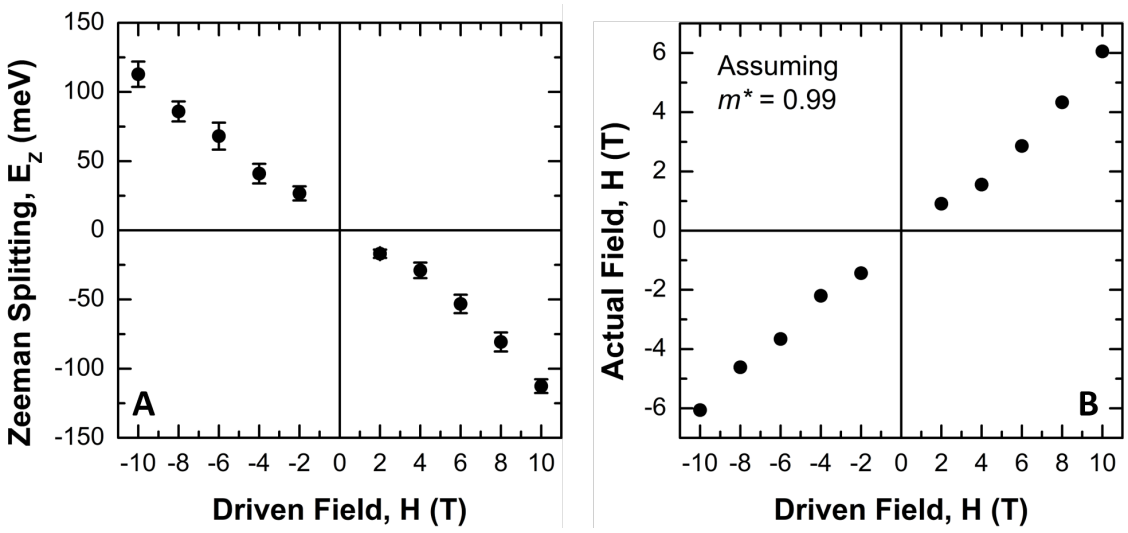

Figure 4.2: MCD Instrument Calibration Using Gold Nanoparticles.

6.2 nm gold nanoparticles were utilized as an external reference to calibrate the sign of dichroism of the MCD instrument and ensure that m^* is correctly calculated across the 10 T driven field sweep. (**A**) MCD spectra were collected for gold nanoparticles in toluene solution located in the stray field of the Cryostat at 298 K at the driven fields referenced. (**B**) Subsequently, the Zeeman splitting energy was calculated from the Python fitting routine, where the actual field experienced by the particles could be calculated utilizing 0.99 $\frac{m^*}{m_e}$ as a reference,[22] showcasing expected linear Zeeman splitting behavior from the applied stray field.

is 10 T to 6 T and follows an exponential decay with distance) of the cryostat. The experimental calibration results agree with published data[22] and confirm the experimental setup is properly corrected. (Figure 4.2). Positive and negative field magnetic vector directions were confirmed through the use of a right circularly polarized film to identify whether to subtract positive field data from negative, or negative from positive when performing the difference measurements in the Faraday configuration.

Variable Temperature (1.8 K – 75 K at 10 T) Magnetic Circular Dichroism (VT-MCD). The same experimental setup used for VT-MCD measurements: while holding the applied magnetic field at + 10 T, the temperature was swept from a minimum temperature of 1.8 K to 75 K, where three scans were taken at each temperature point and averaged, utilizing the InGaAs NIR detector to measure C_0 term contributions at and near the LSPR feature.

VH-MCD Effective Mass Fitting. From the spectra, experimental absorption spectra are used as the basis for a rigid-shift simulation of LCP and RCP absorption as a function of E_Z to fit the experimental VH-MCD spectra. The simulated MCD fit is optimized by a custom Python code at each field, allowing for the direct measurement of E_Z and m^* at every measured magnetic field, thereby increasing the accuracy and robustness of MCD measurements. The acquisition of m^* through MCD itself is not novel, however the acquisition through comparison by RS approximation of a corresponding absorption spectrum is non-trivial.[22] The novelty originates from the spectral range and standardization of data analysis, which allows for multiple collections of m^* from only one experimental MCD run which sweeps through various magnetic field strengths, and every field integer can subsequently be treated as its own experiment. Simulated MCD spectra are calculated using the Scipy.optimize.curve_fit() Python function, utilizing the Trust Region Reflective algorithm to provide a simulation of best fit, using E_Z as the dependent variable for minimization. The Python code used is publicly available at https://github.com/strouselabgithub/strouselab.

Superconducting Quantum Design MPMS SQUID Magnetometry. Field and Temperature sweep SQUID magnetometry was performed on Cu_5FeS_4 diluted in eicosane (1:10 mg) and loading as a powder in gel capsules. The dilution in eicosane is to minimize particle-particle interactions. Magnetization data was collected at 4 K from -50 to 50 kOe, while magnetic susceptibility data was recorded at 1 kOe for field sweep and no field for the zero field sweep measurements from 2 – 300 K.

Computational Details. DFT + U calculations were performed to simulate the projected density of states for Cu_5FeS_4 utilizing the open-source QuantumESPRESSO repository.[83] A single unit cell of Cu_5FeS_4 was initialized with lattice constants of 5.475 Å, similar to prior literature.[152] Plane augmented wave pseudopotentials were used in addition to unrestricted DFT + U, as was used previously for $CuFeS_2$.[139] Self-consistent field calculations were performed on a relaxed structure with a Monkhorst k-point mesh of 6 x 6 x 6 to maximize sampling across the dielectric field of the Brillouin zone.[153] This was followed by a non-self-consistent field calculation of 12 x 12 x 12 for the simulated projected density of states. Simulated absorption spectra and transitions of interest were acquired by diagonalizing and solving for allowed transitions after calculating the density of states (DOS). Magnetic anisotropy energy (MAE) was calculated using the Force Theorem method[171] by comparing total energy of the system under perpendicular and parallel magnetic orientations.

4.4 Results and Discussion

Bulk 5:1 bornite exhibits a second-order magnetic – structural phase transition at 67 K that is coupled with a structural phase transition from *Pbca* to $Pca2_1$ resulting in a loss of higher-order symmetry at T ¡ 67 K.[143,172] The second order transition in bulk sample is described as a RT paramagnetic -to-low-temperature antiferromagnetic (PM-AFM) transition, but can be thought as a spin glass transition due to spin reordering. The structural shift from *Pbca* to $Pca2_1$ will induce changes in g-factor tensors as shown in Figure 4.3A. The presence of the structural-magnetic phase transition leads to a complex spin ordering event causing increased magnetocrystalline anisotropy, reminiscent of a Bose-Einstein condensate.[173] The increased anisotropy will impact carrier mass, as seen in the anisotropic crystal structure of anatase TiO_2.[174] In the case of 5:1 bornite, this will be dependent on the strength of the applied magnetic field, leading to anomalous Zeeman splitting for the electronic transitions. This can be explained as resulting from the nonlinear g-factor changes occurring as a function of decreasing temperature and modeled after the changes in unit cell parameters observed by Rietveld refinement.[143]

4.4.1 Computational Predictions.

In Figure 4.3, the impact on the electronic levels of the *Pbca* to $Pca2_1$ structural change for 5:1 bornite (Figure 4.3A) can be evaluated by considering the anticipated splitting of the electronic levels in magnetic field (Figure 4.3B). The change in energy with field can be rewritten in terms of the anisotropic g-values (Eqn. 4.2):

$$g = (g_{xx}^2 \sin^2\theta \cos^2\phi + g_{yy}^2 \sin^2\theta \sin^2\phi + g_{zz}^2 \cos^2\theta)^{1/2} \tag{4.2}$$

In the case of the $Pca2_1$ structure when only considering lattice parameters, $g_{xx} \neq g_{yy} \neq g_{zz}$. Schematically, this is represented in Figure 4.3B and illustrates the importance of considering the evolution of g-factor contributions under magnetic field as a function of temperature. In the case of 5:1 bornite, as temperature decreases, the disparity in anisotropic g-values increases and directly correlates to a rise in magnetocrystalline anisotropy that should be observable experimentally.

Figures 4.3C and 4.3D present the predicted electronic structure and magnetocrystalline anisotropy as the calculated projected density of states (DOS) and magnetic anisotropy energy (MAE). The

MAE and DFT calculations were performed on a reduced unit cell (Figure 4.3A) using Quantum-mESPRESSO density functional theory (DFT) self-consistent field calculations.[83] Consistent with literature precedent,[140] the 5:1 bornite has a band gap of approximately 2.09 eV with two intermediate band gaps of 0.22 eV and 1.12 eV associated with Fe tetrahedral d-level splitting. The Fermi level beneath the valence band edge (Figure 4.3C) also agrees with the assignment of a p-type IBSC system. Hybridization between Cu-3d and S-2p is evident in the valence band in the DOS.

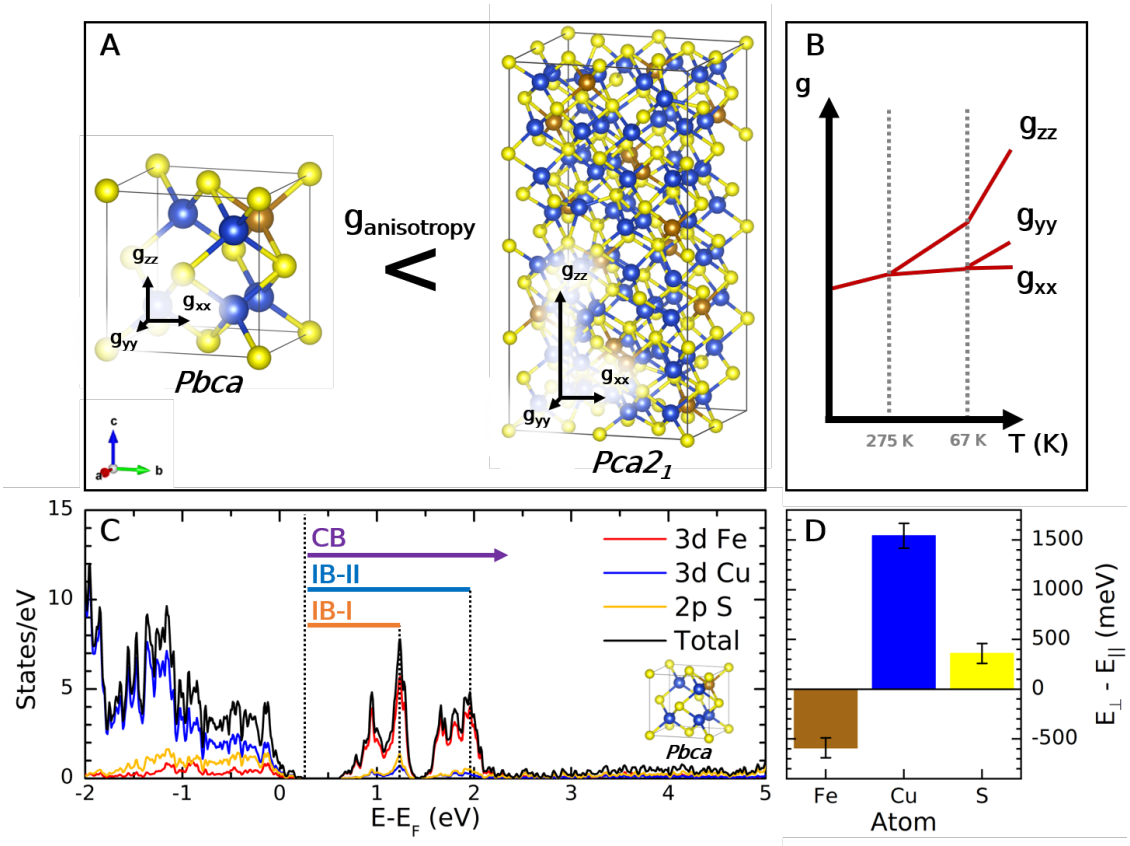

Figure 4.3: Theoretical Investigation of Cu_5FeS_4.

The cubic Cu_5FeS_4 unit cell used in calculations for this work is compared to the low temperature $Pca2_1$ phase[143] with expected g-factor vector differences. Sulfur atoms are yellow, copper is blue, and iron is brown. (**B**) Expected g-factor splitting behavior as a function of temperature with a breaking of symmetry initially occurring at 275 K for *Pbca* and then occurring again at 67 K for $Pca2_1$. (**C**) A representative DOS plot identifying high probability electronic transitions and showing the expected IBSC structure. (**D**) DFT calculations were used to calculate magnetic anisotropy energy (MAE) for perpendicular versus parallel magnetic moment orientations for the unit cell and broken down by atomic differences.

To calculate the MAE, QuantumESPRESSO uses ultrasoft pseudopotentials in the generalized-gradient approximation, selected through the standard solid-state pseudopotential library [175–177] to generate a semi-quantitative understanding of MAE utilizing the Force Theorem method. [171] This allows the total electronic band energy to be differentiated between perpendicular and parallel magnetic dipole moments. The value of the full MAE is 2.14 eV on average between the Fe(III) atom and the averaged Cu(I) atoms. Cu shows the greatest deviation in magnetic dipole moment, favoring a parallel magnetic dipole, while Fe favors a perpendicular magnetic dipole orientation. While S should possess no magnetic moment, it is hypothesized that a MAE is experienced for these atoms due to orbital hybridization of the Cu-3d with S-2p, as observed in the DOS. The observed hybridization is expected to introduce magnetic coupling between these two electronic states in the form of p-d exchange coupling. [178] As the observed extinction feature in an LSPR mode is reflective of the imaginary and real component crossing of the dielectric function, it is anticipated the LSPR mode will be impacted by the magnetic anisotropy, especially considering the carriers originate from Fe vacancies. [140]

4.4.2 Magnetic Properties.

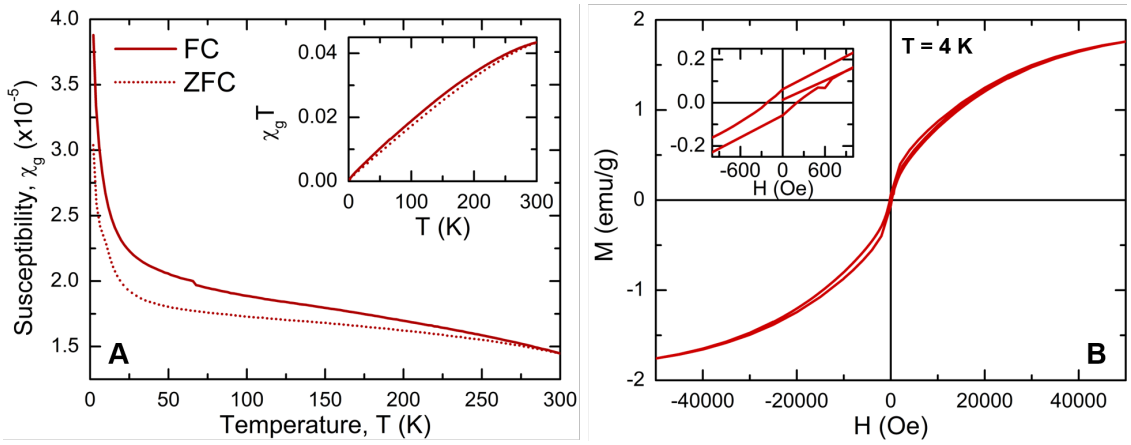

Figure 4.4: Magnetic Data of Cu_5FeS_4 PSNCs.

(**A**) Magnetic susceptibility measurements show a high degree of coercivity between FC and ZFC curves with the previously reported antiferromagnetic transition at 67 K41 observed as a discontinuity. Additionally, the majority linear behavior seen in χT (**A**, inset) indicates the presence of long-range antiferromagnetic ordering. (**B**) Magnetization measurements were performed at 4 K, showing a narrow hysteresis loop that indicates weak coercivity approaching the single domain, superparamagnetic regime for the Cu_5FeS_4 PSNCs.

In Figure 4.4A, the onset of antiferromagnetic (AFM) order is observed as a discontinuity at 67 K in temperature-dependent magnetic susceptibility (2 – 300 K) measurements using a superconducting quantum interference device (SQUID). The inset of 4.4A shows a strong linear trend up to 300 K for the χT data, indicating typical paramagnetic behavior associated with the DOS projected Fe-3d intermediate band level.[38,140] The field sweep data and zero field cooled (ZFC) vs. field cooled (FC) temperature sweep data reveals the 5:1 bornite is magnetic with increased coercivity as temperature decreases for Cu_5FeS_4. The assignment of an AFM magnetic transition at the magnetic susceptibility discontinuity agrees with prior bulk bornite experiments where collinear AFM ordering of spins, parallel and anti-parallel to the b-axis, was reported at T_N = 67.5 K. Ferrimagnetic order appearing below 35 K was associated with charge ordering.[172,179–181] In the bulk bornite, a fluctuation of the spins below 140 K associated with Fe and Cu is observed to produce a magnetic moment with spin orientation that changes due to valence fluctuations. The second-order phase transition at 67.5 K couples the magnetic and lattice (*Pbca* to $Pca2_1$) elements resulting in a structural dependence of electron exchange via the induced crystalline anisotropy following the transition. The structural transition results in a superparamagnetic relaxation leading to a loss of higher-order symmetry, increasing magnetocrystalline anisotropy in the 5:1 bornite.[179] The magnetic and structural properties are associated with temperature-dependent intervalence charge fluctuation ($Fe^{3+/2+}$, $Cu^{2+/1+}$) in the 5:1 stoichiometry below 140 K.

Consistent with the MAE and magnetic measurements, the 5:1 bornite PSNC is anticipated to have a large magnetocrystalline anisotropy caused by the loss of crystallographic symmetry. As the bornite PSNCs themselves are spherical, shape anisotropy is precluded from contributing significantly and is not considered here. The coercivity at 4 K is 200 Oe and saturated magnetization, M_{sat}, is 1.8 emu/g. However, this is likely due to nearing the superparamagnetic regime for these nanocrystals, as they are well within the typical size regime of <10 nm.[182] Utilizing Eqn. 4.3 and 4.4, the effective magnetic anisotropy, K_{eff}, and superparamagnetic diameter threshold, D, can be estimated utilizing the observed blocking temperature, T_b, of 299 K and calculating for the volume, V, of a typical 5 nm nanocrystal:

$$T_b = \frac{K_{eff} V}{25 k_B} \tag{4.3}$$

$$D = \sqrt[3]{\frac{31 k_{\mathrm{B}} T}{K_{\mathrm{eff}}}} \tag{4.4}$$

where k_{B} is the Boltzmann constant and T is the temperature. For Cu_5FeS_4, a K_{eff} of 0.197 MJ/m^3 and D of 1.58 nm at 4 K are predicted for Cu_5FeS_4, agreeing with the experimental data observed.

4.4.3 Optical Properties.

As shown in Figure 3, the p-type Cu_5FeS_4 PSNC exhibits a well-defined LSPR at 1.1 eV. Our previous publication evaluated the LSPR using the Drude model approximation. We concluded that the carriers arose from Fe vacancies with a Drude model predicted effective mass of 1.4 m^*/m_e at RT.[38] As the temperature decreases, carrier mass is expected to increase with the lattice valence ordering. Assuming the onset of AFM order is the same as the reported bulk bornite, charge fluctuation is anticipated to strongly influence the effective carrier mass and thus plasmon properties below 140 K, leading to nonlinear Zeeman effects.[180,183] The effect of magnetic field on the carrier mass can be evaluated using MCD below the magnetic phase transition to calculate the effective carrier mass (m^*) from the cyclotron resonance frequency,[22] as MCD exploits two magneto-optical phenomena in tandem, cyclotron resonance and the Zeeman effect, both of which are described in previous literature with respect to MCD.[9,50,81] Evaluating the field-dependent change in m^* above and below the AFM ordering temperature in the 5:1 bornite PSNC should allow carrier density changes, that are expected to occur with valence ordering in the anisotropic low-temperature 5:1 crystal lattice, to be simulated using the Drude model.

MCD is useful for its sensitivity to site-specific metal contributions in a given material.[184] MCD has been previously used to elucidate fine structure that may appear in optical features such as band gap absorption edges in semiconductors, intra-atomic transitions, and LSPRs.[185–187] The MCD spectra is plotted as the difference spectra (ΔA) of left circularly polarized light (LCP) absorption subtracted from right circularly polarized light (RCP) absorption, where LCP is selective for ΔM_{J}=$\pm$1 while RCP is selective for ΔM_{J}=-1. These selection rules allow for energy shifting in the LCP and RCP absorption spectra.[81] The difference in energy for LCP and RCP absorption for spin levels of the electronic system is termed the Zeeman effect. The magnitude of the Zeeman effect is contingent on the degree of splitting proportional to magnetic field strength, rather than

originating from a property intrinsic to the material itself such as chirality for circular dichroism. The Zeeman effect is represented by the splitting of the electronic energy level induced by the application of an external magnetic field, represented mathematically as (Eqn. 4.5):

$$E_{\mathrm{Z}} = g u_{\mathrm{B}} M_{\mathrm{J}} \vec{\mathbf{B}} \tag{4.5}$$

where g is the g-factor, μ_{B} is the Bohr magneton, M_{J} is the total angular momentum, and $\vec{\mathbf{B}}$ is the total magnetic flux in the material.[81] The Zeeman splitting energy (E_{Z}) is fundamental to magneto-optical spectroscopy and allows for the observation of electronic transitions that would otherwise be impossible for traditional optical techniques. The carrier type (n or p) is evaluated by inspection of the sign of the LCP absorption feature, with p-type showing a positive LCP and n-type exhibiting a negative LCP feature.

By assuming Born-Oppenheimer, Franck-Condon, and Rigid-Shift (RS) approximations, the ΔA MCD spectrum can be deconvoluted into three constituent shapes classified as A_1, B_0, and C_0 terms (Eqn. 4.6):[50]

$$A_1 : B_0 : C_0 = 1/\Gamma_{\mathrm{abs}} : 1/\Delta E : 1/(k_{\mathrm{B}} T) \tag{4.6}$$

where Γ_{abs} is the absorption feature linewidth magnitude, ΔE is the zero-field state separation magnitude, k_{B} is the Boltzmann constant, and T is temperature.[50] The A_1-term originates from the lifting of degeneracy in the nearest excited state due to Zeeman splitting directly proportional to the magnetic field applied to the sample. A_1-term effects are broadly identifiable from their derivative-shaped curve, where both a positive and negative feature will be present in the differential spectrum. A_1-terms are extremely useful for determining the precise energy level of an electronic orbital at zero field by examining where inflection points appear. The B_0-term is unique because it arises from the population mixing of neighboring, nondegenerate excited states at zero-field. As a magnetic field is applied, the change in the mixing of populated states accounts for differences observed in a B_0-term feature. C_0-term effects could be considered an opposite process relative to the A_1-term, as nondegeneracy arises in the ground state of an electronic transition under an applied magnetic field. In 5:1 bornite PSNCs, the magneto-structural phase transition will lead to crystalline anisotropy and a magnetic ground state, resulting in A_1- and C_0-term contributions to the MCD spectra. C_0-term contributions are typical in paramagnetic systems.[50]

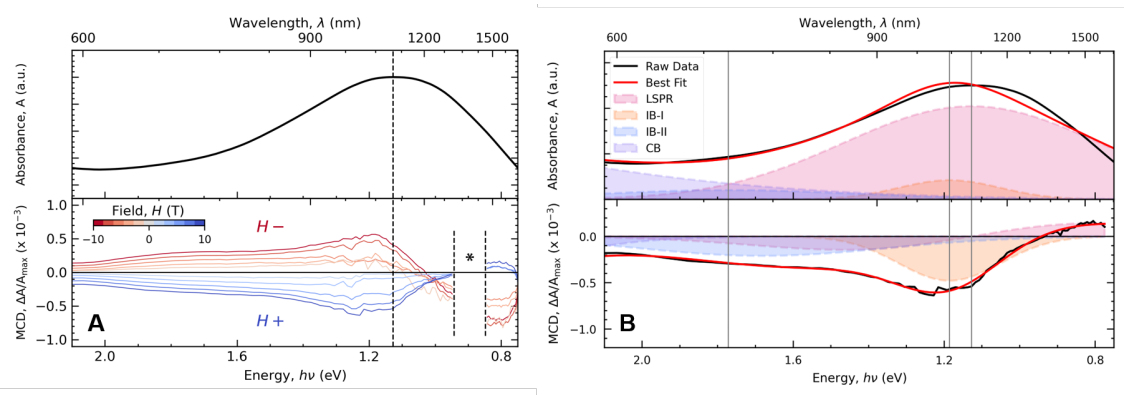

Figure 4.5: Magneto-optical data of Cu_5FeS_4 PSNCs.

(**A**, top) A characteristic 40 K linear absorption spectrum of 5 nm Cu_5FeS_4 is shown with an LSPR extinction feature observed at 1.1 eV and indirect band gap at 2.1 eV paired with (**A**, bottom) VH-MCD data taken for Cu_5FeS_4, where the VH-MCD data is merged from a visible Si detector and a near infrared InGaAs detector. The LSPR peak observed in linear absorption is slightly higher in energy compared to the inflection point observed in the VH-MCD spectra (1.1 vs. 1.0 eV as denoted by the dashed line). A discontinuity in data in the VH-MCD data is removed at 0.9 eV marked by the asterisk attributed to a characteristic transmission dip observable in Spectrosil B windows. The full, unmodified spectra can be found in Figure 4.6. (**B**, bottom) MCD Data at 10 T is deconvoluted by several probable electronic transitions observed in the previously performed DOS calculations. (**B**, top) Subsequently, the linear absorption is reconstructed utilizing the same transition energies and FWHM, letting the amplitude float as the spectra is fit with the Scipy.optimize.curve_fit() least squares fitting algorithm. Grey vertical lines mark the various transitions assigned.

In Figure 4.5, linear absorption and variable field MCD (VH-MCD) from +10 to -10 T are measured on dropcast films of Cu_5FeS_4 at 40 K between 600 and 1700 nm, seen in Figures 4.5A and 4.5B, respectively. The experimental data is collected on substrate cast films inserted into a He-cryostat and required separate data collection regions due to limits in spectral sensitivity of the detectors available. The MCD spectra are plotted as the measured difference ($\Delta A/A_{max}$) between LCP and RCP spectra. A transmission dip at 0.9 eV is attributed to a small absorption in Spectrosil B quartz which, while not visible in the linear absorption, is likely due to the lower signal and sensitivity of the VH-MCD data. In Figure 4.5A, the MCD inflection is not centered on the LSPR peak. The offset may be due to underlying overlapping transitions with different Zeeman energies or, more likely, inter-particle coupling in the cast film, as observed in gold plasmonic nanomaterials.[188,189]

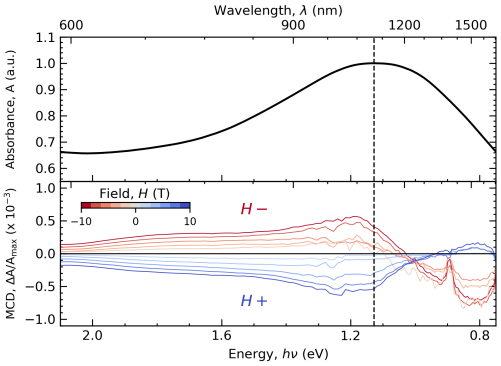

Figure 4.6: Full VH-MCD spectra of Cu_5FeS_4 PSNCs.

Table 4.1: Cu_5FeS_4 MCD and Absorption Fitting Parameters

Peak Assignment	**Energy (eV)**	A_1 (C_0)/D	B_0/D (eV^{-1})	**Abs FWHM (eV)**	**Abs Amplitude (a.u.)**
LSPR	1.12	-8.29E+02	–	0.8	0.409
IB-I	1.19	-3.89E+01	-9.76E+03	0.32	0.086
IB-II	1.77	2.02E+03	-8.52E+03	0.76	0.041
CB	3.44	3.70E+04	-9.18E-03	1.01	0.186

For the linear absorption compared with previously performed colloidal solution measurements,[38] an overall increase in inter-particle scattering is observed for Cu_5FeS_4, coincident with an increase in the FWHM. Across multiple samples prepared using various dropcasting methods, the observed thin-film spectra are consistent and reproducible, pointing to a real change in the dielectric function. Fitting the frequency-independent simplified Drude model utilizing the MATLAB code from Milliron and coworkers[39] was used to quantify these observed differences in terms of the plasma frequency (ω_p) and damping term (Γ) for Cu_5FeS_4, using 3.48 as the dielectric constant of Cu_5FeS_4,[183] shown in Figure 4.7. The changes in the frequency and damping contributions between temperatures are quantified by subtracting the room temperature fits from the 40 K results, where $Cu_5FeS_4(\Delta\omega_p)$ = 1201.7 cm^{-1}, $Cu_5FeS_4(\Delta\Gamma)$ = 5791.14 cm^{-3}. These results show that the damping observed in the dropcast Cu_5FeS_4 sample is significantly greater compared to the colloidal solution, supportive of an increase in overall inter-particle effects, donor level scattering65, or changes in the local dielectric.

The VH-MCD spectra in Figure 3A can be evaluated in terms of the A1- (Zeeman term), B0- (field-induced state mixing), and C0- (ground state degeneracy due to paramagnetic state) terms (Eqn. 4.7).

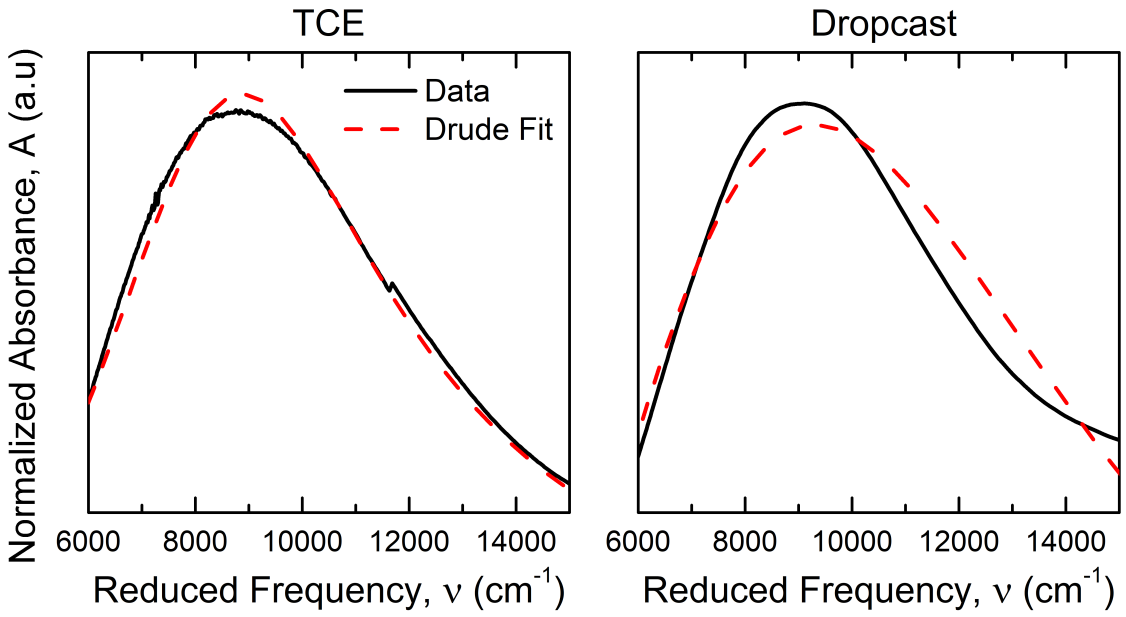

Figure 4.7: Frequency-independent Drude modelling of the Cu_5FeS_4 LSPR.

Cu_5FeS_4 nanocrystals either in TCE solution (left) or dropcast (right) are compared utilizing the frequency-independent Drude modelling MATLAB code as performed previously by Milliron and coworkers.[39]

$$\frac{\Delta D_{MCD}(E)}{E} = \gamma\{A_1(-\frac{df(E)}{dE}) + (B_0 + \frac{C_0}{k_B T})f(E)\}(\mu_B \mathbf{H})cz \tag{4.7}$$

where $\Delta D_{MCD}(E)$ is the MCD spectrum, $E = h\nu$ for photon energy, γ is an oscillator strength constant, $f(E)$ is the linear absorption spectra normalized by area, $k_B T$ is the Boltzmann constant and temperature product, μ_B is the Bohr magneton, $\mathbf{H}$ is the field strength, c is the concentration, and z is the pathlength.[9,82] The 5:1 bornite is magnetic and may have C_0-term contribution. The coupled structural and magnetic phase transition below 67 K may impact the value of C_0. It is anticipated that the ratio of A_1:B_0:C_0 is the same as in Eqn. 4.6 (1:10:200 for this experiment at 40 K).[190] The temperature dependence of the MCD signal for the LSPR band and IB-I was measured at 10 T from 75 K – 1.8 K to evaluate the magnitude of the C_0 contribution (Figure 4.8). As the second-order magneto-structural phase transition occurs at 67 K, it is anticipated that a temperature dependent MCD response may be observable from 75 – 1.8 K reflecting the onset of spin-carrier interactions. The lack of MCD spectral change with temperature in the phase transformation region at 10 T, suggests the MCD data is dominated by the A_1 (C_0) and B_0 terms in

Eqn. 4.7 for the 5:1 bornite due to the maximization of magnetic dipole orientation along the high m^* axis at 10 T. At lower magnetic field, a temperature dependence is expected, as the magnetic dipole is not maximized in one vector orientation, however further studies are needed to validate this hypothesis.

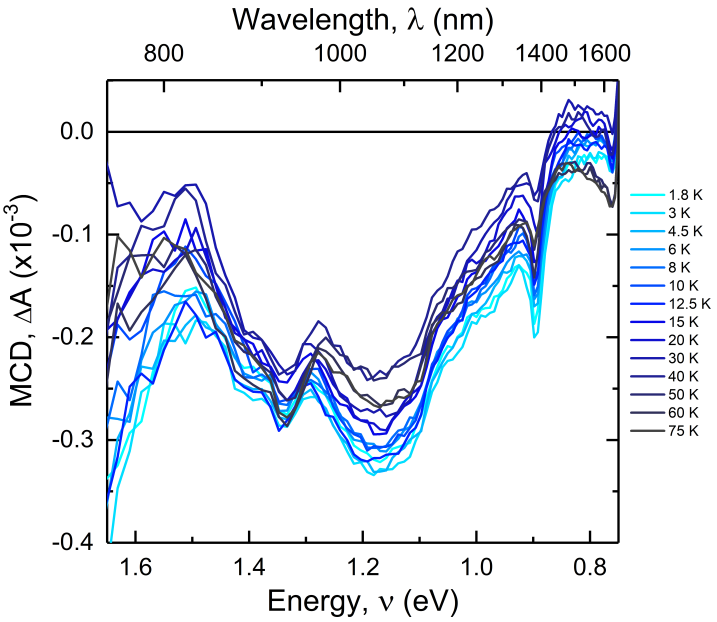

Figure 4.8: Cu_5FeS_4 VT-MCD at 10 T.

VT-MCD is performed on Cu_5FeS_4 PSNCs in the NIR regime. An overall change in the signal in the MCD is observed, however there does not appear to be obvious C_0 term behavior, rather only a slight temperature dependence on the overall signal is observable.

In Figure 4.5, the experimental data are fit to a convolved A_1 : C_0 and B_0 term. The deconvolution of peaks are formed by the summation of a Gaussian curve representing C_0 and B_0 terms and the derivative of a Gaussian curve representing the A_1 term, modeled after previous literature.[82] The assigned electronic transitions in the MCD at 1.12 (LSPR), 1.19 (IB-I), 1.77 (IB-II), and 3.44 (CB) eV are identified through second-order derivation of the linear absorption spectrum in tandem with the most probable computationally identified electronic transitions. For the fits, the normalized transition dipole moments were obtained as indicated previously by Safin et al.[82] The assumption of a B_0 contribution and a convolved A_1-: C_0-term reflect the known magnetic ground

state in 5:1 bornite and the difficulty to deconvolve the MCD spectra fully. MCD parameters for the identified transitions are listed in Table 1.

The LSPR and IB-I (VB $\rightarrow$ d-band (Fe-e_g)) transitions are dominated by the convoluted A_1:C_0 term contributions (referred to as A_1 term henceforth), while IB-II (VB $\rightarrow$ d-band (Fe-t_{2g})) and CB transitions have A_1 and B_0-term contributions, indicating that there is a high degree of mixing of energy levels present in these band regions. The B_0 contribution in IB-II reflects the low ΔE of the split t_{2g} level compared to IB-I (Figure 4.3). The CB exhibits the largest A_1-term reflecting the multitude of excited state transitions that can occur within the CB. The MCD fits show negative A1 term dichroism for the LSPR and IB-I transitions, while the IB-II and CB show positive dichroism. The negative A_1-term for the LSPR transition experimentally confirms the 5:1 sample is a p-type PSNC.[22,191] The observed opposite dichroism correlates to antiparallel magnetic moments for the Cu 3d and Fe 3d orbitals below the AFM ordering temperature in 5:1 bornite. Fe vacancies are theorized to be the source of free holes in chalcopyrite, $CuFeS_2$, and are suspected of having the same origin for the carriers generating the p-type LSPR for bornite-like semiconductors.[140,192] The observation of the same dichroism for LSPR and IB-I likely indicates that the carriers are in the IB-I Fe 3d (e_g) bands.

Effective Mass Calculation. From the MCD spectral assignments, m^* can be evaluated using the relationship in Eqns. 4.8 and 4.9,

$$m^* = \frac{eB}{\omega_c m_e} \tag{4.8}$$

$$\omega_c = \frac{2\pi E_Z}{c} \tag{4.9}$$

where ω_c is the cyclotron resonance frequency, e is the elementary charge, B is the magnetic field, m_e is the mass of an electron, E_Z is the Zeeman splitting, and c is the speed of light. Assuming the LSPR will obey the RS approximation, as previously reported by Gamelin and coworkers,[22] the LCP and RCP spectra will split equally about the LSPR frequency, resulting in the observed MCD spectrum (Figure 4.9). The field-dependent splitting yields a Zeeman splitting value (E_Z) as observed in Eqn. 4.5.[81,193] In Figure 4.10, the Zeeman term as a function of the applied field is plotted and exhibits asymptotic behavior. The asymptote reflects the field-driven spin orientation of the spin lattice in the 5:1 bornite, consistent with the model developed for bulk bornites.[172,180]

A plot of the field-dependent m^* for 5:1 bornite is shown in Figure 4.10. A complete description of the m^* calculation can be found in the Supporting Information. The m^* exhibits a field-dependent effective mass that can be fitted to a hyperbolic cotangent arising from the spin ordering saturation at high fields, consistent with the SQUID data. The value of m^* exhibits a minimum of 2.73 ± 0.041 m^*/m_e at 2 T and maximum of 5.98 ± 0.074 m^*/m_e at 10 T. The calculated value for m^* at 2 T is high, but not unreasonable for a p-type semiconductor system with intrinsic Fe vacancies present in the crystal structure. As the concentration of vacancies increases, the increase in scattering centers will dampen the carrier mobility and be reflected in the m^* value. Combined with the previously discussed DFT results, as the valence band is primarily composed of S-2p and Cu-3d and IB composed of Fe-3d, the field-dependent m^* behavior can be correlated and understood through the increased band overlap due to high field Zeeman splitting increasing the degree of the p-d exchange interaction.[178]

When compared to similar Cu-based p-type systems, the m^* values calculated are within reason.[105] For example, Kumar et al. observed an increase in carrier mobility and a subsequent decrease in effective mass through the doping of Se.[194] Although no bulk measurement of pure Cu_5FeS_4 could be obtained, the nearest ratio $Cu_5FeS_{3.9}Se_{0.1}$ was measured to have an m^* of 2.56. However, with the degree of carrier mobility shift due to Se doping, it is likely that the intrinsic m^* for Cu_5FeS_4 is much higher than what could be effectively measured using the Hall effect. With an observed significant increase in resistivity and decrease in carrier mobility, one would expect the m^* for bulk bornite to be higher than 2.56 m^*/m_e, which corresponds with the directly measured 2 T m^*/m_e from VH-MCD in this paper. Utilizing prior data from bulk Cu_5FeS_4, a constant carrier relaxation time approximation is used to extrapolate what the undoped Cu_5FeS_4 value may be, utilizing a Se doped system previously published shown in Figure 4.11. From a first order, linear approximation between m^* and the electron mobility, the predicted m^* for a bulk Cu_5FeS_4 is near 2.71 m^*/m_e under no applied magnetic field, matching surprisingly well to the MCD experimental data. Yet, it does not explain the asymptotic behavior seen as the effective mass rapidly increases with increasing field.

As reported by Pineider, a possibility for the increased m^* value is neighboring electronic interband transitions leading to variation in the local dielectric function.[46] From the DFT calculations and literature, interband coupling may impact the local dielectric function.[38] However, the inter-

band mixing alone would not account for the observed enhancement of m^*. Previous work with $Cu_{2-x}Se$, featuring very similar optical absorption and MCD A_1-term asymmetry, also reported differences in bulk versus nanocrystal m^* due to changes in carrier compensation.[22] The observation of a large m^* in anatase TiO_2 is thought to arise from crystalline anisotropy, resulting in differences in carrier mobility along separate axes of the crystal structure.[174] In Au/Co/Au film nanostructures, excitation of the LSPR under applied magnetic field resulted in a strengthening of magnetic anisotropy along a given crystallographic axis.[195] Similarly, the magneto-crystalline anisotropy is anticipated to impact the MCD spectra for 5:1 bornite due to the previously reported magneto-structural transition at 67 K[143] and photoexcitation from the MCD experiment itself.

The presence of the hyperbolic field-dependent m^* values suggests a major contributor to the large m^* value is the coupling of the spins on the iron and Cu center to the holes in 5:1 bornite. The stronger coupling at high magnetic field will lead to a greater degree of phonon-hole coupling to the lattice from the observed magnetocrystalline anisotropy and a greater degree of magnetically coupled carriers experiencing a reduction in mean free path from the applied magnetic field. Additionally, as previously observed in the linear absorption, increased inter-particle interactions between individual bornite PSNCs are expected to increase the degree of phonon-hole coupling and further enhance the theoretical m^*. The result is an increased value of 5.98 m^*/m_e at fields ¿8 T. Large g-values have also been reported in dilute magnetic semiconductors due to the carriers coupling to magnetic spin.[196] By analogy to dilute magnetic semiconductors where the carrier is coupled to spins in the lattice, the field-dependent response of m^* can be fit to a Brillouin function in Eqn. 4.10, assuming the relationship of the cyclotron resonance, E_Z, and LSPR, such that

$$m^* = \frac{1}{2} N g_s \mu_B \left[(2S+1) \coth\left((2S+1) \frac{g_s \mu_B B}{2 k_B T} \right) - \coth\left(\frac{g_s \mu_B B}{2 k_B T} \right) \right] \tag{4.10}$$

where N is a fitting parameter, g_s is the Lande' g-factor, μ_B is the Bohr magneton, S is the spin quantum number, B is magnetic field, k_B is the Boltzmann constant, and T is temperature. A large g-value (14.3) is extracted from the experimental data fit in Figure 4.10 assuming $S = \frac{1}{2}$ and T = 40 K. Similar magnetic dependence has been observed previously in dilute magnetic semiconductors[197] and recently in gold cluster interband transitions, where the thermally driven population of d-band carriers were reported to be involved.[198] The experimental data supports

the coupling of the d-band spins and hole carriers in the 5:1 bornite through the spin-ordering structural transition.

4.5 Conclusions

Cu_5FeS_4 PSNCs were examined by various optical, magnetic, and magneto-optical techniques in tandem to measure the effective mass of bornite directly and explain the origins of the observed field-dependent behavior. DFT and SQUID measurements highlighted that bornite exhibits an antiferromagnetic transition that leads to increased magneto-crystalline anisotropy and a coupling of the d-bands to the hole carriers in the conduction band via a p-d exchange mechanism. The exchange mechanism leads to a field-dependent m^* value that when fitted to a Brillouin function, yields a large g-value for the LSPR.

The Cu_5FeS_4 nanocrystal is confirmed to be a p-type semiconductor based on the VH-MCD data. The m^* of the LSPR at 1.12 eV in Cu_5FeS_4 was quantified as 2.73 m^*/m_e in the low field regime and 5.98 m^*/m_e in the high field regime utilizing high field VH-MCD. The observed field-dependent m^* behavior was attributed to a substantial decrease in the carrier mean free path due to magnetocrystalline anisotropy, polaronic type coupling with native defects, and LSPR-enhanced magnetic anisotropy. Further work should be done to experimentally validate the anisotropy of m^* proposed in Cu_5FeS_4, as was previously done for anatase. The observation of an external magnetic field directly influencing the electronic transport properties in Cu_5FeS_4 PSNCs, suggest the role of magneto-crystalline anisotropy on carrier transport in plasmonic and thermoelectric materials is under-investigated in nanomaterials.

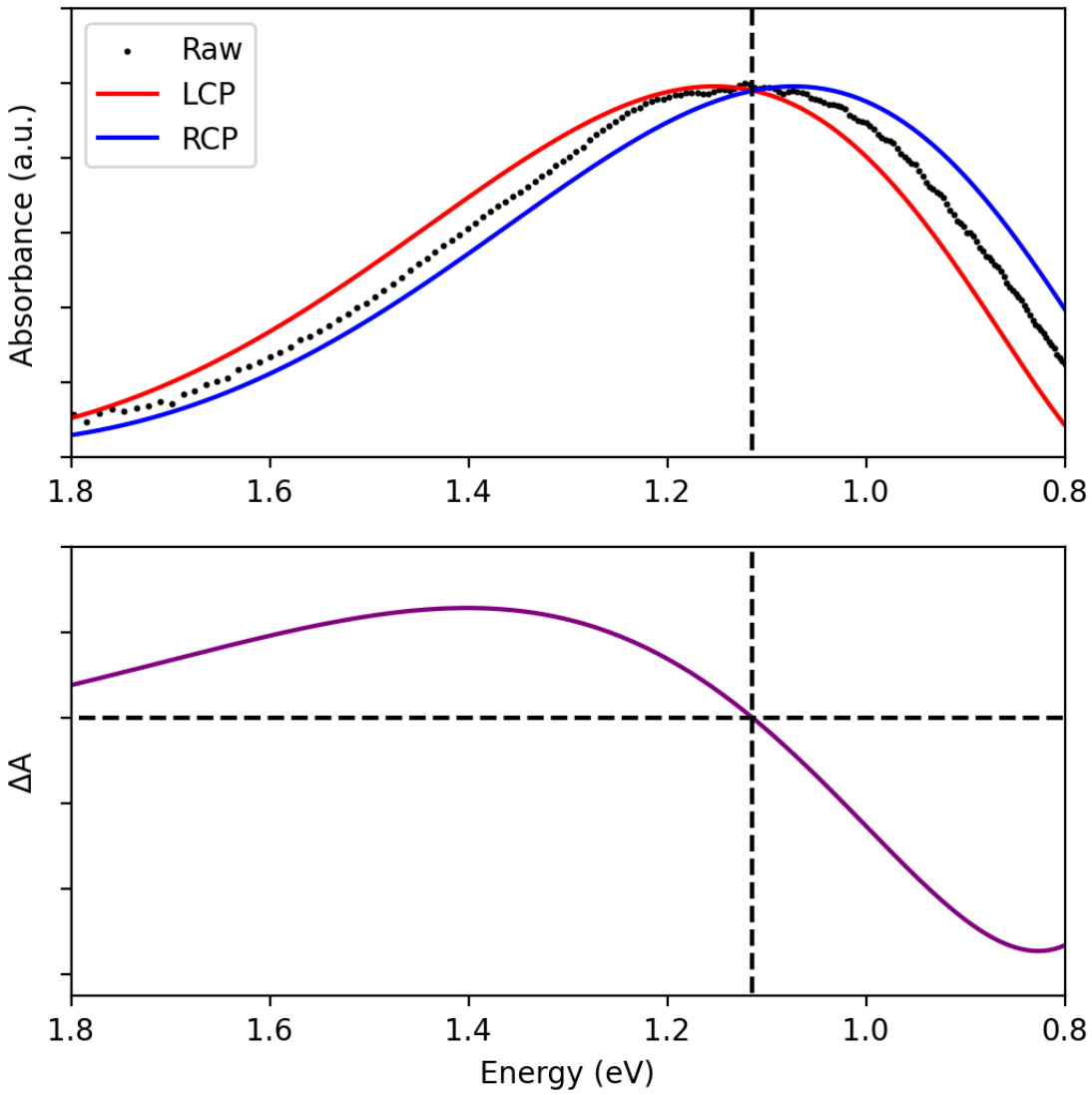

Figure 4.9: Zeeman Energy Fitting with associated effective mass.

Description of m^* Acquisition from VH-MCD. The linear absorption data for Cu_5FeS_4 was fit according to a combined version of Eqn. 4.6 and 4.7, where m^* can be directly solved utilizing $m^* = \frac{eBc}{2\pi E_Z m_e}$ after obtaining an experimental E_Z term. To obtain E_Z through an MCD spectrum, it is required to simulate separate LCP and RCP spectra shifted by some constant energy, assuming the rigid-shift approximation (top) utilizing a known experimental absorption spectrum. Once found, a custom least squares fitting program through the Scipy.optimize.curve_fit() python package was used in order to optimize the Zeeman energy difference separating the LCP and RCP spectra until the least squares fit was achieved, resulting in a simulated MCD spectrum (bottom). The source code can be found at https://github.com/strouselabgithub/strouselab.

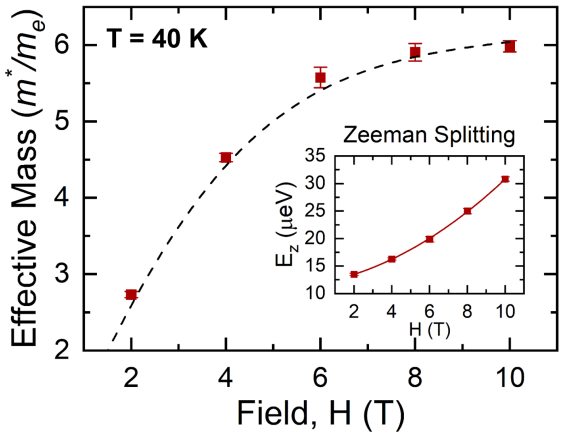

Figure 4.10: Effective Mass Behavior in Cu_5FeS_4 PSNCs.

VH-MCD for Cu_5FeS_4 were fit with simulated MCD spectra to obtain a Zeeman splitting energy (E_Z) for all collected fields at 40 K. Once E_Z is calculated, m^* is solved for utilizing a convolution of Eqn. 8 and 9, where a magnetic field dependent behavior is observed. A sigmoidal-like increase in m^* is observed until 10 T, where m^* approaches an asymptote of 5.98 m^*/m_e and is fit to a Brillouin function (dotted line) with S = $\frac{1}{2}$. The raw Ez fit data (inset) is shown to also increase in a non-linear fashion and is fit to a 5/3 power law.

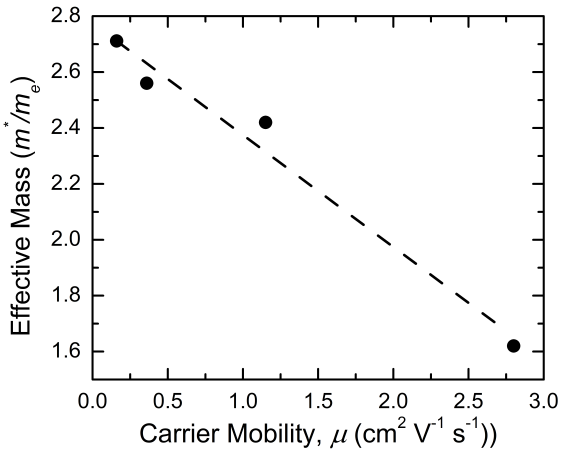

Figure 4.11: Effective Mass Approximation Utilizing Data from Kumar et al.

Utilizing the first principal relationship between the carrier effective mass, m^*, and the carrier mobility, μ, $m^* = \frac{\bar{\tau}q}{\mu}$, where $\bar{\tau}$ is the carrier scattering constant, and q is the electronic charge. Taking tabulated data from Kumar et al. in experimental doping of Se into Cu_5FeS_4,[194] Assuming this linear relationship, the m^* can be approximated to first order, giving a result of 2.71 m^*/m_e, remarkably similar to the 2.73 m^*/m_e value obtained through experimental MCD at 2 T.

CHAPTER 5

FUTURE WORKS

While much work has been done to further understand the relationship between semiconducting electronic band structure and plasmonic properties in PSNCs, there is still plenty left to be done. The following are very brief overviews of potential future directions for PSNC investigation and application development.

Experimental Validation of m^*

The experimental validation of m^* with changes in LSPR frequency is largely unexplored in literature with the exception of a key InN experiment showcasing how doping in the nonparabolic band regime can result in dramatic increases in m^* (0.06 - 0.3 m^*/m_e), resulting in an invariant LSPR frequency.[48] Considering that the parabolic band approximation fails in the limit of high carrier density or high doping level, MCD or optical hall effect techniques should be utilized to precisely evaluate LSPR frequency changes *via* the free electron model.

Additionally, there are still unanswered questions as to the degree of quantum confinement effects on m^*, *el-ph*, and *ph-ph* rates. fsTA experiments by Schaller and coworkers[120] showed negligible changes for hot carrier relaxation rates as a function of PSNC size, however the smallest size explored was 10 nm, much larger than the Bohr radius of CdO. Additionally, semiconductor quantum dot literature supports substantial increases in m^* as quantum confinement is reached depending on the parabolicity of the band.[199] It is also expected that an inverse relationship between Γ and m^* exists according to the Drude conductivity model,[42] but a thorough investigation is still lacking in present literature.

Preliminary studies on larger WO_{3-x} (2 - 10 nm) grown *via* the successive ionic layer adsorption and reaction (SILAR) method[200,201] shows a faster transition from photoinduced absorption of the V_O^{2+} state to stimulated emission observable in fsTA. These results are reminiscent of perovskite studies by Beard and coworkers which shows that hot carrier relaxation is dictated largely by the phonon density of states available for hot carrier relaxation *via* a hot phonon bottleneck.[202] MCD experiments should additionally be performed on the LSPR extinction as a function of WO_{3-x}

size to fully characterize m^* dependence as a function of size with chemical titration to monitor simultaneous changes in n. Investigating stoichiometry dependence such as in WO_{3-x} on emission energy and radiative relaxation rate with simultaneous effects on LSPR energy and damping is also of interest.

Plasmon-Intermediate Band Coupling

Exploring other IBSC systems such as $CuCrS_2$ as analogues to Cu_xFeS_4 to explore further plasmon overlap with IB to explore electric and magnetic field coupling via plasmon resonance. The Cu_5FeS_4 system appears to display unique high magnetic field dependence on the LSPR m^*, and it is suggested that work be performed to discover new plasmonic IBSC NCs which have LSPR and IB overlap to further explore this novel magnetic-field dependence.

The Future of Plasmonics for Electro-Optical Applications

Seminal work has been done by the Milliron group for the development of plasmonic gels,[203] while the Law group has done phenomenal work at characterizing nanocrystal superlattice structures for extended mini-band transport.[204] With the development of these materials, it may be possible to begin interrogate the current density, mobility, effective mass, and other parameters otherwise accessible through traditional hall type measurements in thin-film devices.

It is likely the field will either need to mature by improving the performance and fully characterizing PSNC assemblies for current use, or development of other scientific areas for example in all-optical computing must progress before colloidal PSNCs can be used reliably for solely optically driven applications.

BIBLIOGRAPHY

[1] Crookes, W. On radiant matter; a lecture delivered to the British Association for the Advancement of Science, at Sheffield, Friday, August 22, 1879. *Am. J. Sci.* **1879**, *s3-18*, 241–262.

[2] Langmuir, I. Oscillations in Ionized Gases. *Proc. Natl. Acad. Sci.* **1928**, *14*, 627–637.

[3] Pines, D. Collective Energy Losses in Solids. *Rev. Mod. Phys.* **1956**, *28*, 184–198.

[4] Kittel, C. *Introduction to solid state physics*, 8th ed.; Wiley: Hoboken, NJ, 2005.

[5] Reed, J. Light-matter Interactions Of Plasmonic Nanostructures. Ph.D. thesis, University of Central Florida, 2013.

[6] Chang-Ming, J. Charge Carrier Dynamics in Transition Metal Oxides Studied by Femtosecond Transient Extreme Ultraviolet Absorption Spectroscopy. Ph.D. thesis, UC Berkeley, 2015.

[7] Hartstein, K. H. Stabilizing Degenerate Dopants in Colloidal Semiconductor Nanocrystals. Ph.D., University of Washington, Ann Arbor, 2018.

[8] Agrawal, A.; Johns, R. W.; Milliron, D. J. Control of Localized Surface Plasmon Resonances in Metal Oxide Nanocrystals. *Annu. Rev. Mater. Res.* **2017**, *47*, 1–31.

[9] Han, B.; Gao, X.; Lv, J.; Tang, Z. Magnetic Circular Dichroism in Nanomaterials: New Opportunity in Understanding and Modulation of Excitonic and Plasmonic Resonances. *Adv. Mater.* **2020**, *32*, 1801491.

[10] Diroll, B. T.; Kirschner, M. S.; Guo, P.; Schaller, R. D. Optical and Phys. Probing of Thermal Processes in Semiconductor and Plasmonic Nanocrystals. *Annu. Rev. Phys. Chem.* **2019**, *70*, 353–377.

[11] Maxwell, J. C. VIII. A dynamical theory of the electromagnetic field. *Philosophical Transactions of the Royal Society of London* **1865**, *155*, 459–512.

[12] Lorentz, H. A. *The theory of electrons and its applications to the phenomena of light and radiant heat*, dover ed ed.; Dover Publications: New York, 1952.

[13] Colton, J. Lorentz Oscillator Model. 2020.

[14] Tipler, P. A. *Physics for scientists and engineers*, 4th ed.; W.H. Freeman/Worth Publishers: New York, 1999.

[15] Johnson, P. B.; Christy, R. W. Optical Constants of the Noble Metals. *Phys. Rev. B* **1972**, *6*, 4370–4379.

[16] Wooten, F. *Optical properties of solids*; Academic Press: New York, 1972.

[17] Battie, Y.; Resano-Garcia, A.; Chaoui, N.; Zhang, Y.; En Naciri, A. Extended Maxwell-Garnett-Mie formulation applied to size dispersion of metallic nanoparticles embedded in host liquid matrix. *J. Chem. Phys.* **2014**, *140*, 044705.

[18] Li, Y. *Plasmonic Opt. Theory and Applications*; SPIE PRESS, 2017.

[19] Hoddeson, L.; Baym, G.; Eckert, M. The development of the quantum-mechanical electron theory of metals: 1928—1933. *Rev. Mod. Phys.* **1987**, *59*, 287–327.

[20] Pérez, E.; Ibáñez, J. Indistinguishable elements in the origins of quantum statistics. The case of Fermi–Dirac statistics. *Eur. Phys. J. H* **2022**, *47*, 1.

[21] Reif, F. *Fundamentals of statistical and thermal physics*, 43rd ed.; McGraw-Hill series in fundamentals of physics; McGraw-Hill: New York, 1998.

[22] Hartstein, K. H.; Schimpf, A. M.; Salvador, M.; Gamelin, D. R. Cyclotron Splittings in the Plasmon Resonances of Electronically Doped Semiconductor Nanocrystals Probed by Magnetic Circular Dichroism Spectroscopy. *J. Phys. Chem. Lett.* **2017**, *8*, 1831–1836.

[23] Schimpf, A. M.; Thakkar, N.; Gunthardt, C. E.; Masiello, D. J.; Gamelin, D. R. Charge-Tunable Quantum Plasmons in Colloidal Semiconductor Nanocrystals. *ACS Nano* **2014**, *8*, 1065–1072.

[24] Murray, C. B.; Norris, D. J.; Bawendi, M. G. Synthesis and characterization of nearly monodisperse CdE (E = sulfur, selenium, tellurium) semiconductor nanocrystallites. *J. Am. Chem. Soc.* **1993**, *115*, 8706–8715.

[25] Mock, J. J.; Barbic, M.; Smith, D. R.; Schultz, D. A.; Schultz, S. Shape effects in plasmon resonance of individual colloidal silver nanoparticles. *J. Chem. Phys.* **2002**, *116*, 6755–6759.

[26] Agrawal, A.; Cho, S. H.; Zandi, O.; Ghosh, S.; Johns, R. W.; Milliron, D. J. Localized Surface Plasmon Resonance in Semiconductor Nanocrystals. *Chem. Rev.* **2018**, *118*, 3121–3207.

[27] Zandi, O.; Agrawal, A.; Shearer, A. B.; Reimnitz, L. C.; Dahlman, C. J.; Staller, C. M.; Milliron, D. J. Impacts of surface depletion on the plasmonic properties of doped semiconductor nanocrystals. *Nat. Mater.* **2018**, *17*, 710–717.

[28] Schubert, M.; Kühne, P.; Darakchieva, V.; Hofmann, T. Optical Hall effect—model description: tutorial. *JOSA A* **2016**, *33*, 1553–1568.

[29] Lanigan, D.; Thimsen, E. Contact Radius and the Insulator–Metal Transition in Films Comprised of Touching Semiconductor Nanocrystals. *ACS Nano* **2016**, *10*, 6744–6752.

[30] Greenberg, B. L.; Robinson, Z. L.; Ayino, Y.; Held, J. T.; Peterson, T. A.; Mkhoyan, K. A.; Pribiag, V. S.; Aydil, E. S.; Kortshagen, U. R. Metal-insulator transition in a semiconductor nanocrystal network. *Sci. Adv.* **2019**, *5*, eaaw1462.

[31] Staller, C. M.; Gibbs, S. L.; Gan, X. Y.; Bender, J. T.; Jarvis, K.; Ong, G. K.; Milliron, D. J. Contact Conductance Governs Metallicity in Conducting Metal Oxide Nanocrystal Films. *Nano Lett.* **2022**, *22*, 5009–5014.

[32] Conti III, C. R.; Quiroz-Delfi, G.; Schwarck, J. S.; Chen, B.; Strouse, G. F. Carrier Density, Effective Mass, and Nuclear Relaxation Pathways in Plasmonic Sn:In2O3 Nanocrystals. *J. Phys. Chem. C* **2020**, *124*, 28220–28229.

[33] Conti, C. R.; McBride, J. R.; Strouse, G. F. Examining the Effect of Dopant Ionic Radius on Plasmonic M:ZnO Nanocrystals (M = Al3+, Ga3+, In3+). *J. Phys. Chem. C* **2021**, *125*, 7772–7779.

[34] Shubert-Zuleta, S. A.; Tandon, B.; Roman, B. J.; Gan, X. Y.; Milliron, D. J. How to Quantify Electrons in Plasmonic Colloidal Metal Oxide Nanocrystals. *Chem. Mater.* **2023**, *35*, 3880–3891.

[35] Schimpf, A. M.; Ochsenbein, S. T.; Buonsanti, R.; Milliron, D. J.; Gamelin, D. R. Comparison of extra electrons in colloidal n-type Al3+-doped and photochemically reduced ZnO nanocrystals. *Chem. Comm.* **2012**, *48*, 9352–9354.

[36] Xiao, Z.; Drake, H. F.; Day, G. S.; Kuszynski, J. E.; Lin, H.; Xie, H.; Cai, P.; Ryder, M. R.; Zhou, H.-C. Photoinduced reversible phase transition in a phenothiazine-based metal-organic framework. *Cell Reports Phys. Science* **2022**, *3*, 101074.

[37] Dong, A.; Ye, X.; Chen, J.; Kang, Y.; Gordon, T.; Kikkawa, J. M.; Murray, C. B. A Generalized Ligand-Exchange Strategy Enabling Sequential Surface Functionalization of Colloidal Nanocrystals. *J. Am. Chem. Soc.* **2011**, *133*, 998–1006.

[38] Kays, J. C.; Conti, C. R.; Margaronis, A.; Kuszynski, J. E.; Strouse, G. F.; Dennis, A. M. Controlled Synthesis and Exploration of CuxFeS4 Bornite Nanocrystals. *Chem. Mater.* **2021**, *33*, 7408–7416.

[39] Mendelsberg, R. J.; Garcia, G.; Milliron, D. J. Extracting reliable electronic properties from transmission spectra of indium tin oxide thin films and nanocrystal films by careful application of the Drude theory. *J. Appl. Phys.* **2012**, *111*, 063515.

[40] Mergel, D.; Qiao, Z. Dielectric modelling of optical spectra of thin In_2O_3:Sn films. *J. Phys. D Appl. Phys.* **2002**, *35*, 794–801.

[41] Lounis, S. D.; Runnerstrom, E. L.; Bergerud, A.; Nordlund, D.; Milliron, D. J. Influence of Dopant Distribution on the Plasmonic Properties of Indium Tin Oxide Nanocrystals. *J. Am. Chem. Soc.* **2014**, *136*, 7110–7116.

[42] Gibbs, S. L.; Staller, C. M.; Agrawal, A.; Johns, R. W.; Saez Cabezas, C. A.; Milliron, D. J. Intrinsic Optical and Electronic Properties from Quantitative Analysis of Plasmonic Semiconductor Nanocrystal Ensemble Optical Extinction. *J. Phys. Chem. C* **2020**, *124*, 24351–24360.

[43] Tandon, B.; Shubert-Zuleta, S. A.; Milliron, D. J. Investigating the Role of Surface Depletion in Governing Electron-Transfer Events in Colloidal Plasmonic Nanocrystals. *Chem. Mater.* **2022**, *34*, 777–788.

[44] Agrawal, A.; Kriegel, I.; Milliron, D. J. Shape-Dependent Field Enhancement and Plasmon Resonance of Oxide Nanocrystals. *J. Phys. Chem. C* **2015**, *119*, 6227–6238.

[45] Roman, B. J.; Shubert-Zuleta, S. A.; Shim, G.; Kyveryga, V.; Faris, M.; Milliron, D. J. Facet-Enhanced Dielectric Sensitivity in Plasmonic Metal Oxide Nanocubes. *J. Phys. Chem. C* **2023**, *127*, 2456–2463.

[46] Pineider, F.; Campo, G.; Bonanni, V.; de Julián Fernández, C.; Mattei, G.; Caneschi, A.; Gatteschi, D.; Sangregorio, C. Circular Magnetoplasmonic Modes in Gold Nanoparticles. *Nano Lett.* **2013**, *13*, 4785–4789.

[47] Kuszynski, J. E.; Kays, J. C.; Conti, C. R.; McGill, S. A.; Dennis, A. M.; Strouse, G. F. Effective Mass for Holes in Paramagnetic, Plasmonic Cu_5FeS_4 Semiconductor Nanocrystals. *J. Phys. Chem. C* **2022**, *126*, 12669–12679.

[48] Liu, Z.; Beaulac, R. Nature of the Infrared Transition of Colloidal Indium Nitride Nanocrystals: Nonparabolicity Effects on the Plasmonic Behavior of Doped Semiconductor Nanomaterials. *Chem. Mater.* **2017**, *29*, 7507–7514.

[49] Kriegel, I.; Urso, C.; Viola, D.; De Trizio, L.; Scotognella, F.; Cerullo, G.; Manna, L. Ultrafast Photodoping and Plasmon Dynamics in Fluorine–Indium Codoped Cadmium Oxide Nanocrystals for All-Optical Signal Manipulation at Optical Communication Wavelengths. *J. Phys. Chem. Lett.* **2016**, *7*, 3873–3881.

[50] Stephens, P. J. Theory of magnetic circular dichroism. *J. Chem. Phys.* **1970**, *52*, 3489–3516.

[51] Rothman, T.; Boughn, S. The Lorentz force and the radiation pressure of light. *Am. J. Phys.* **2009**, *77*, 122–127.

[52] Holgate, S. A. *Understanding solid state physics*, second edition ed.; CRC Press: Boca Raton, 2021.

[53] Sebastian O. J. Long; Anthony V. Powell; Paz Vaqueiro; Stephen Hull High Thermoelectric Performance of Bornite through Control of the Cu(II) Content and Vacancy Concentration. *Chem. Mater.* **2018**, *30*, 456–464.

[54] Conti III, C. R. Localized Surface Plasmon Resonances in Semiconductor Nanocrystals. Ph.D. thesis, Florida State University, 2022.

[55] Wheeler, D. A.; Zhang, J. Z. Exciton Dynamics in Semiconductor Nanocrystals. *Adv. Mater.* **2013**, *25*, 2878–2896.

[56] Koch, S. W.; Kira, M.; Khitrova, G.; Gibbs, H. M. Semiconductor excitons in new light. *Nat. Mater.* **2006**, *5*, 523–531.

[57] Lee, S. Y.; Shim, G.; Park, J.; Seo, H. Tunable polaron-induced coloration of tungsten oxide *via* a multi-step control of the physicochemical property for the detection of gaseous F. *Phys. Chem. Chem. Phys.* **2018**, *20*, 16932–16938.

[58] Deb, S. K. Opportunities and challenges in science and technology of WO3 for electrochromic and related applications. *Sol. Energy Mater.* **2008**, *92*, 245–258.

[59] Caruso, F.; Lambert, H.; Giustino, F. Band Structures of Plasmonic Polarons. *Phys. Rev. Lett.* **2015**, *114*, 146404.

[60] Song, X.; Liu, J.; Shi, F.; Fan, C.; Ran, S.; Zhang, H.; Zou, Z. Facile fabrication of KmC-snWO3 with greatly improved near-infrared shielding efficiency based on W5+-induced small polaron and local surface plasmon resonance (LSPR) modulation. *Sol. Energy Mater.* **2020**, *218*, 110769.

[61] Varga, B. B. Coupling of Plasmons to Polar Phonons in Degenerate Semiconductors. *Phys. Rev.* **1965**, *137*, A1896–A1902.

[62] Wehrenberg, B. L.; Wang, C.; Guyot-Sionnest, P. Interband and Intraband Optical Studies of PbSe Colloidal Quantum Dots. *J. Phys. Chem. B* **2002**, *106*, 10634–10640.

[63] Achermann, M.; Bartko, A. P.; Hollingsworth, J. A.; Klimov, V. I. The effect of Auger heating on intraband carrier relaxation in semiconductor quantum rods. *Nat. Phys.* **2006**, *2*, 557–561.

[64] Pelton, M.; Ithurria, S.; Schaller, R. D.; Dolzhnikov, D. S.; Talapin, D. V. Carrier Cooling in Colloidal Quantum Wells. *Nano Lett.* **2012**, *12*, 6158–6163.

[65] Kuszynski, J. E.; Fabiano, C. J.; Nguyen, E. T.; Mao, K.; Ahuja, A. K.; Schaller, R. D.; Strouse, G. F. Plasmon-Induced Hot-Carrier Excited-State Dynamics in Plasmonic Semiconductor Nanocrystals. *J. Phys. Chem. C* **2023**, *127*, 22654–22661.

[66] Li, X.; Xiao, D.; Zhang, Z.; Zhenyu Zhang Landau damping of quantum plasmons in metal nanostructures. *New J. Phys.* **2013**, *15*, 023011.

[67] Brongersma, M. L.; Halas, N. J.; Nordlander, P. Plasmon-induced hot carrier science and technology. *Nat. Nanotechnol.* **2015**, *10*, 25–34.

[68] Diroll, B. T.; Schramke, K. S.; Guo, P.; Kortshagen, U. R.; Schaller, R. D. Ultrafast Silicon Photonics with Visible to Mid-Infrared Pumping of Silicon Nanocrystals. *Nano Lett.* **2017**, *17*, 6409–6414.

[69] Fleischmann, M.; Hendra, P.; McQuillan, A. Raman spectra of pyridine adsorbed at a silver electrode. *Chem. Phys. Lett.* **1974**, *26*, 163–166.

[70] Kelly, K. L.; Coronado, E.; Zhao, L. L.; Schatz, G. C. The Optical Properties of Metal Nanoparticles: The Influence of Size, Shape, and Dielectric Environment. *J. Phys. Chem. B* **2003**, *107*, 668–677.

[71] Monika Ahlawat; Mittal, D.; Rao, V. G. Plasmon-induced hot-hole generation and extraction at nano-heterointerfaces for photocatalysis. **2021**,

[72] Kumar, S.; Sushant Kumar; Habib, A.; Sundararaman, R. Plasmonic hot carriers scratch the surface. **2021**,

[73] Keene, J. D.; Freymeyer, N. J.; McBride, J. R.; Rosenthal, S. J. Ultrafast spectroscopy studies of carrier dynamics in semiconductor nanocrystals. *iScience* **2022**, *25*, 103831.

[74] Li, J.; Cushing, S. K.; Meng, F.; Senty, T. R.; Bristow, A. D.; Wu, N. Plasmon-induced resonance energy transfer for solar energy conversion. *Nat. Photonics* **2015**, *9*, 601–607.

[75] Yang, X.; Skrabalak, S. E.; Li, Z.-Y.; Xia, Y.; Wang, L. V. Photoacoustic Tomography of a Rat Cerebral Cortex in vivo with Au Nanocages as an Optical Contrast Agent. *Nano Lett.* **2007**, *7*, 3798–3802.

[76] Tian, Q.; Hu, J.; Zhu, Y.; Zou, R.; Chen, Z.; Yang, S.; Li, R.; Su, Q.; Han, Y.; Liu, X. Sub-10 nm Fe_3O_4@$Cu_{2-x}S$ Core–Shell Nanoparticles for Dual-Modal Imaging and Photothermal Therapy. *J. Am. Chem. Soc.* **2013**, *135*, 8571–8577.

[77] Yoo, S.; Hong, S.; Choi, Y.; Park, J.-H.; Nam, Y. Photothermal Inhibition of Neural Activity with Near-Infrared-Sensitive Nanotransducers. *ACS Nano* **2014**, *8*, 8040–8049.

[78] Yuan, L.; Hu, W.; Zhang, H.; Chen, L.; Wang, J.; Wang, Q. Cu5FeS4 Nanoparticles With Tunable Plasmon Resonances for Efficient Photothermal Therapy of Cancers. *Front. Bioeng. Biotechnol.* **2020**, *8*.

[79] Vincely, V. D.; Katakam, S. P.; Huda, K.; Zhong, X.; Kays, J.; Dennis, A.; Bayer, C. L. Biodegradable and biocompatible semiconductor nanocrystals as NIR-II photoacoustic imaging contrast agents. Photons Plus Ultrasound: Imaging and Sensing 2023. San Francisco, United States, 2023; p 137.

[80] Christopher, P.; Moskovits, M. Hot Charge Carrier Transmission from Plasmonic Nanostructures. *Annu. Rev. Phys. Chem.* **2017**, *68*, 379–398.

[81] Mason, W. R. *A Practical Guide to Magnetic Circular Dichroism Spectroscopy: Mason/MCD Spectroscopy*; John Wiley & Sons, Inc.: Hoboken, NJ, USA, 2007.

[82] Safin, F.; Maslov, V.; Gromova, Y.; Korsakov, I.; Kolesova, E.; Dubavik, A.; Cherevkov, S.; Gun'ko, Y. K. Investigation of Magnetic Circular Dichroism Spectra of Semiconductor Quantum Rods and Quantum Dot-in-Rods. *Nanomaterials* **2020**, *10*, 1059.

[83] Giannozzi, P. et al. QUANTUM ESPRESSO: a modular and open-source software project for quantum simulations of materials. *J. Condens. Matter Phys.* **2009**, *21*, 395502.

[84] Deslippe, J.; Samsonidze, G.; Strubbe, D. A.; Jain, M.; Cohen, M. L.; Louie, S. G. BerkeleyGW: A massively parallel computer package for the calculation of the quasiparticle and optical properties of materials and nanostructures. *Comput. Phys. Commun.* **2012**, *183*, 1269–1289.

[85] Lehtola, S.; Blockhuys, F.; Van Alsenoy, C. An Overview of Self-Consistent Field Calculations Within Finite Basis Sets. *Molecules* **2020**, *25*, 1218.

[86] Polman, A. Plasmonics Applied. *Science* **2008**, *322*, 868–869.

[87] Tang, H.; Zihui, T.; Bright, J.; Liu, B.; Botong Liu; Wang, X.; Meng, G.; Wu, N. Visible-Light Localized Surface Plasmon Resonance of WO3–x Nanosheets and Its Photocatalysis Driven by Plasmonic Hot Carriers. *ACS Sustainable Chemistry & Engineering* **2021**, *9*, 1500–1506.

[88] Hattori, Y.; Gutiérrez Álvarez, S.; Meng, J.; Zheng, K.; Sá, J. Role of the Metal Oxide Electron Acceptor on Gold–Plasmon Hot-Carrier Dynamics and Its Implication to Photocatalysis and Photovoltaics. *ACS Applied Nano Materials* **2021**, *4*, 2052–2060.

[89] Liu, Z.; Zhong, Y.; Shafei, I.; Borman, R.; Jeong, S.; Chen, J.; Losovyj, Y.; Gao, X.; Li, N.; Du, Y.; Sarnello, E.; Li, T.; Su, D.; Ma, W.; Ye, X. Tuning infrared plasmon resonances in doped metal-oxide nanocrystals through cation-exchange reactions. *Nat. Commun.* **2019**, *10*, 1394.

[90] Ghorai, N.; Ghosh, H. N. Ultrafast Plasmon Dynamics and Hole–Phonon Coupling in NIR Active Nonstoichiometric Semiconductor Plasmonic $Cu_{2-x}S$ Nanocrystals. *J. Phys. Chem. C* **2019**, *123*, 28401–28410.

[91] Zhou, D.; Dongming Zhou; Li, X.-F.; Zhou, Q.; Qiaohui Zhou; Qiaohui Zhou; Zhu, H.; Haiming Zhu Infrared driven hot electron generation and transfer from non-noble metal plasmonic nanocrystals. **2020**, *11*, 2944.

[92] Yin, H.; Kuwahara, Y.; Mori, K.; Louis, C.; Yamashita, H. Properties, fabrication and applications of plasmonic semiconductor nanocrystals. *Catal. Sci. Technol.* **2020**, *10*, 4141–4163.

[93] Cong, S.; Geng, F.; Zhao, Z. Tungsten Oxide Materials for Optoelectronic Applications. *Adv. Mater.* **2016**, *28*, 10518–10528.

[94] Manthiram, K.; Alivisatos, A. P. Tunable Localized Surface Plasmon Resonances in Tungsten Oxide Nanocrystals. *J. Am. Chem. Soc.* **2012**, *134*, 3995–3998.

[95] Prusty, G.; Lee, J. T.; Seifert, S.; Muhoberac, B. B.; Sardar, R. Ultrathin Plasmonic Tungsten Oxide Quantum Wells with Controllable Free Carrier Densities. *J. Am. Chem. Soc.* **2020**, *142*, 5938–5942.

[96] Salje, E.; Güttler, B. Anderson transition and intermediate polaron formation in WO_{3-x} Transport properties and optical absorption. *Philosophical Magazine B* **1984**, *50*, 607–620.

[97] O F Schirmer; E Salje Conduction bipolarons in low-temperature crystalline WO_{3-x}. *Journal of Physics C: Solid State Physics* **1980**, *13*, L1067–L1072.

[98] Kenny-Wilby, A.; Jaics, G.; Zhang, C.; Yin, P.; Radovanovic, P. V. Revisiting Plasmonic Properties of Complex Semiconductor Nanocrystals Using Magnetic Circular Dichroism Spectroscopy: A Cautionary Tale. *J. Phys. Chem. C* **2023**, *127*, 1087–1096.

[99] Villegas, C. E. P.; Leite, M. S.; Marini, A.; Rocha, A. R. Efficient hot-carrier dynamics in near-infrared photocatalytic metals. *Phys. Rev. B* **2022**, *105*, 165109.

[100] Liu, Q.; Wu, Y.; Zhang, J.; Chen, K.; Huang, C.; Chen, H.; Qiu, X. Plasmonic MoO3-x nanosheets with tunable oxygen vacancies as efficient visible light responsive photocatalyst. *Appl. Surf. Sci.* **2019**, *490*, 395–402.

[101] White, T. P.; Catchpole, K. R. Plasmon-enhanced internal photoemission for photovoltaics: Theoretical efficiency limits. *Applied Physics Lett.* **2012**, *101*, 073905.

[102] Jang, Y. H.; Jang, Y. J.; Kim, S.; Quan, L. N.; Chung, K.; Kim, D. H. Plasmonic Solar Cells: From Rational Design to Mechanism Overview. *Chem. Rev.* **2016**, *116*, 14982–15034.

[103] Amendola, V.; Pilot, R.; Frasconi, M.; Maragò, O. M.; Iatì, M. A. Surface plasmon resonance in gold nanoparticles: a review. *J. Condens. Matter Phys.* **2017**, *29*, 203002.

[104] Tang, H.; Chen, C.-J.; Chih-Jung Chen; Huang, Z.; Bright, J.; Meng, G.; Liu, R.-S.; Wu, N. Plasmonic hot electrons for sensing, photodetection, and solar energy applications: A perspective. *J. Chem. Phys.* **2020**, *152*, 220901–220901.

[105] Shen, Y.; Li, C.; Huang, R.; Tian, R.; Ye, Y.; Pan, L.; Koumoto, K.; Zhang, R.; Wan, C.; Wang, Y. Eco-friendly p -type Cu 2 SnS 3 thermoelectric material: crystal structure and transport properties. *Sci. Rep.* **2016**, *6*, 32501.

[106] Washington Ii, A. L.; Strouse, G. F. Microwave Synthesis of CdSe and CdTe Nanocrystals in Nonabsorbing Alkanes. *J. Am. Chem. Soc.* **2008**, *130*, 8916–8922.

[107] Luo, J. Y.; Xu, N. S.; Zhao, F. L.; Deng, S. Z.; Tao, Y. T. Ultraviolet superfluorescence from oxygen vacancies in WO3-x nanowires at room temperature. *J. Appl. Phys.* **2011**, *109*, 024312.

[108] Johansson, M. B.; Zietz, B.; Niklasson, G. A.; Österlund, L. Optical properties of nanocrystalline WO $_3$ and WO $_{3-x}$ thin films prepared by DC magnetron sputtering. *J. Appl. Phys.* **2014**, *115*, 213510.

[109] Wang, B.; Zhong, X.; He, C.; Zhang, B.; Shao, R.; Shvalya, V.; Cvelbar, U.; Ostrikov, K. Controlling oxygen vacancies of WO suboxides by ZnWO4 nanophase hybridization. *Materials Science and Engineering: B* **2020**, *262*, 114706.

[110] Wang, B.; Zhong, X.; He, C.; Zhang, B.; Cvelbar, U.; Ostrikov, K. Nanostructure conversion and enhanced photoluminescence of vacancy engineered substoichiometric tungsten oxide nanomaterials. *Mater. Chem. Phys.* **2021**, *262*, 124311.

[111] Camarda, P.; Messina, F.; Vaccaro, L.; Agnello, S.; Buscarino, G.; Schneider, R.; Popescu, R.; Gerthsen, D.; Lorenzi, R.; Gelardi, F. M.; Cannas, M. Luminescence mechanisms of defective ZnO nanoparticles. *Phys. Chem. Chem. Phys.* **2016**, *18*, 16237–16244.

[112] Galland, C.; Ghosh, Y.; Steinbrück, A.; Hollingsworth, J. A.; Htoon, H.; Klimov, V. I. Lifetime blinking in nonblinking nanocrystal quantum dots. *Nat. Commun.* **2012**, *3*, 908.

[113] Hodak, J.; Martini, I.; Hartland, G. V. Ultrafast study of electron–phonon coupling in colloidal gold particles. *Chem. Phys. Lett.* **1998**, *284*, 135–141.

[114] González-Borrero, P. P.; Sato, F.; Medina, A. N.; Baesso, M. L.; Bento, A. C.; Baldissera, G.; Persson, C.; Niklasson, G. A.; Granqvist, C. G.; Ferreira Da Silva, A. Optical band-gap determination of nanostructured WO3 film. *Applied Physics Lett.* **2010**, *96*, 061909.

[115] Link, S.; El-Sayed, M. A. Spectral Properties and Relaxation Dynamics of Surface Plasmon Electronic Oscillations in Gold and Silver Nanodots and Nanorods. *J. Phys. Chem. B* **1999**, *103*, 8410–8426.

[116] Johns, R. W.; Blemker, M. A.; Azzaro, M. S.; Heo, S.; Runnerstrom, E. L.; Milliron, D. J.; Roberts, S. T. Charge carrier concentration dependence of ultrafast plasmonic relaxation in conducting metal oxide nanocrystals. *J. Mat. Chem. C* **2017**, *5*, 5757–5763.

[117] Klochikhin, A. A.; Kochereshko, V. P.; Besombes, L.; Karczewski, G.; Wojtowicz, T.; Kossut, J. Plasmon mechanism of the trion emission band broadening in quantum wells. *Phys. Rev. B* **2011**, *83*, 235329.

[118] Arora, H.; Wang, S. Application of the polaron model to the F center. *J. Phys. Chem. Solids* **1969**, *30*, 1649–1660.

[119] Wang, F.; Di Valentin, C.; Pacchioni, G. Semiconductor-to-metal transition in WO3-x: Nature of the oxygen vacancy. *Phys. Rev. B* **2011**, *84*, 073103.

[120] Diroll, B. T.; Guo, P.; Chang, R. P. H.; Schaller, R. D. Large Transient Optical Modulation of Epsilon-Near-Zero Colloidal Nanocrystals. *ACS Nano* **2016**, *10*, 10099–10105.

[121] Reshef, O.; De Leon, I.; Alam, M. Z.; Boyd, R. W. Nonlinear optical effects in epsilon-near-zero media. *Nat. Rev. Mater.* **2019**, *4*, 535–551.

[122] Li, C.; Tian, X.; Yang, G.; Dev, S. U.; Allen, M. S.; Allen, J. W.; Harutyunyan, H. Invertible optical nonlinearity in epsilon-near-zero materials. *Phys. Rev. Res.* **2023**, *5*, 013198.

[123] Wang, D.; Zhang, Y.; Guo, Q. Sub-10 nm Cu5FeS4 cube for magnetic resonance imaging-guided photothermal therapy of cancer. *Int. J. Nanomedicine* **2018**, *13*, 7987–7996.

[124] Chen, Y.; Wang, M.; Zheng, K.; Ren, Y.; Xu, H.; Yu, Z.; Zhou, F.; Liu, C.; Qu, J.; Song, J. Antimony Nanopolyhedrons with Tunable Localized Surface Plasmon Resonances for Highly Effective Photoacoustic-Imaging-Guided Synergistic Photothermal/Immunotherapy. *Adv. Mater.* **2021**, 2100039.

[125] Runnerstrom, E. L.; Llordés, A.; Lounis, S. D.; Milliron, D. J. Nanostructured electrochromic smart windows: traditional materials and NIR-selective plasmonic nanocrystals. *Chem. Commun.* **2014**, *50*, 10555–10572.

[126] F. Carvalho, W. O.; Mejía-Salazar, J. R. Plasmonics for Telecommunications Applications. *Sensors* **2020**, *20*, 2488.

[127] Chernov, M.; Roe, A. W. Infrared neural stimulation: a new stimulation tool for central nervous system applications. *Neurophotonics* **2014**, *1*, 011011.

[128] Mott, M.; Koroshetz, W. Bridging the Gap in Neurotherapeutic Discovery and Development: The Role of the National Institute of Neurological Disorders and Stroke in Translational Neuroscience. *Neurotherapeutics: The Journal of the American Society for Experimental NeuroTherapeutics* **2015**, *12*, 651–654.

[129] Lodewijks, K.; Van Roy, W.; Borghs, G.; Lagae, L.; Van Dorpe, P. Boosting the Figure-Of-Merit of LSPR-Based Refractive Index Sensing by Phase-Sensitive Measurements. *Nano Lett.* **2012**, *12*, 1655–1659.

[130] Souza, M. L. d.; Santos, D. P. d.; Corio, P. Localized surface plasmon resonance enhanced photocatalysis: an experimental and theoretical mechanistic investigation. *RSC Adv.* **2018**, *8*, 28753–28762.

[131] Khanna, P. K.; Gaikwad, S.; Adhyapak, P. V.; Singh, N.; Marimuthu, R. Synthesis and characterization of copper nanoparticles. *Materials Lett.* **2007**, *61*, 4711–4714.

[132] Rycenga, M.; Cobley, C. M.; Zeng, J.; Li, W.; Moran, C. H.; Zhang, Q.; Qin, D.; Xia, Y. Controlling the Synthesis and Assembly of Silver Nanostructures for Plasmonic Applications. *Chem. Rev.* **2011**, *111*, 3669–3712.

[133] Gutiérrez, Y.; Brown, A. S.; Moreno, F.; Losurdo, M. Plasmonics beyond noble metals: Exploiting phase and compositional changes for manipulating plasmonic performance. *J. Appl. Phys.* **2020**, *128*, 080901.

[134] Luther, J. M.; Jain, P. K.; Ewers, T.; Alivisatos, A. P. Localized surface plasmon resonances arising from free carriers in doped quantum dots. *Nat. Mater.* **2011**, *10*, 361–366.

[135] Kovalenko, M. V. et al. Prospects of Nanoscience with Nanocrystals. *ACS Nano* **2015**, *9*, 1012–1057.

[136] Liu, W.-D.; Yang, L.; Chen, Z.-G.; Zou, J. Promising and Eco-Friendly Cu2X-Based Thermoelectric Materials: Progress and Applications. *Adv. Mater.* **2020**, *32*, 1905703.

[137] Shi, X.-L.; Zou, J.; Chen, Z.-G. Advanced Thermoelectric Design: From Materials and Structures to Devices. *Chem. Rev.* **2020**, *120*, 7399–7515.

[138] Guo, L.; Panderi, I.; Yan, D. D.; Szulak, K.; Li, Y.; Chen, Y.-T.; Ma, H.; Niesen, D. B.; Seeram, N.; Ahmed, A.; Yan, B.; Pantazatos, D.; Lu, W. A Comparative Study of Hollow Copper Sulfide Nanoparticles and Hollow Gold Nanospheres on Degradability and Toxicity. *ACS nano* **2013**, *7*.

[139] Ghosh, S.; Avellini, T.; Petrelli, A.; Kriegel, I.; Gaspari, R.; Almeida, G.; Bertoni, G.; Cavalli, A.; Scotognella, F.; Pellegrino, T.; Manna, L. Colloidal $CuFeS_2$ Nanocrystals: Intermediate Fe d-Band Leads to High Photothermal Conversion Efficiency. *Chem. Mater.* **2016**, *28*, 4848–4858.

[140] Lee, S.; Ghosh, S.; Hoyer, C. E.; Liu, H.; Li, X.; Holmberg, V. C. Iron-Content-Dependent, Quasi-Static Dielectric Resonances and Oxidative Transitions in Bornite and Chalcopyrite Copper Iron Sulfide Nanocrystals. *Chem. Mater.* **2021**, *33*, 1821–1831.

[141] Kehoe, A. B.; Scanlon, D. O.; Watson, G. W. The electronic structure of sulvanite structured semiconductors Cu_3MCh_4(M = V, Nb, Ta; Ch = S, Se, Te): prospects for optoelectronic applications. *J. Mat. Chem. C* **2015**, *3*, 12236–12244.

[142] Kehoe, A. B.; Scanlon, D. O.; Watson, G. W. Modelling potential photovoltaic absorbers Cu_3MCh_4 (M = V, Nb, Ta; Ch = S, Se, Te) using density functional theory. *J. Condens. Matter Phys.* **2016**, *28*, 175801.

[143] Martinelli, A.; Lepore, G. O.; Bernardini, F.; Giaccherini, A.; Di Benedetto, F. The puzzling structure of Cu5FeS4 (bornite) at low temperature. *Acta Crystallographica Section B: Structural Science, Crystal Engineering and Materials* **2018**, *74*, 405–415.

[144] Wiltrout, A. M.; Freymeyer, N. J.; Machani, T.; Rossi, D. P.; Plass, K. E. Phase-selective synthesis of bornite nanoparticles. *J. Mat. Chem.* **2011**, *21*, 19286.

[145] Gabka, G.; Bujak, P.; Ostrowski, A.; Tomaszewski, W.; Lisowski, W.; Sobczak, J. W.; Pron, A. Cu–Fe–S Nanocrystals Exhibiting Tunable Localized Surface Plasmon Resonance in the Visible to NIR Spectral Ranges. *Inorg. Chem.* **2016**, *55*, 6660–6669.

[146] Meulenberg, R. W.; Offen, H. W.; Strouse, G. F. Low Pressure Band Tuning in Wurtzite CdSe Quantum Dots. *MRS Online Proceedings Library (OPL)* **2000**, *636*.

[147] Meulenberg, R. W.; Strouse, G. F. Pressure-induced electronic coupling in CdSe semiconductor quantum dots. *Phys. Rev. B* **2002**, *66*, 035317.

[148] Kitagawa, Y.; Yao, H. Plasmon-Induced Polarity Inversion of Magnetic Circular Dichroism (MCD) Responses of Cu–Fe–S Bornite Nanodots upon Oxidation. *J. Phys. Chem. C* **2023**, *127*, 22149–22156.

[149] Lounis, S. D.; Runnerstrom, E. L.; Llordés, A.; Milliron, D. J. Defect Chemistry and Plasmon Physics of Colloidal Metal Oxide Nanocrystals. *J. Phys. Chem. Lett.* **2014**, *5*, 1564–1574.

[150] Runnerstrom, E. L.; Bergerud, A.; Agrawal, A.; Johns, R. W.; Dahlman, C. J.; Singh, A.; Selbach, S. M.; Milliron, D. J. Defect Engineering in Plasmonic Metal Oxide Nanocrystals. *Nano Lett.* **2016**, *16*, 3390–3398.

[151] Gibbs, S. L.; Staller, C. M.; Milliron, D. J. Surface Depletion Layers in Plasmonic Metal Oxide Nanocrystals. *Acc. Chem. Res.* **2019**, *52*, 2516–2524.

[152] Qiu, P.; Zhang, T.; Qiu, Y.; Shi, X.; Chen, L. Sulfide bornite thermoelectric material: a natural mineral with ultralow thermal conductivity. *Energy Environ. Sci.* **2014**, *7*, 4000–4006.

[153] Monkhorst, H. J.; Pack, J. D. Special points for Brillouin-zone integrations. *Phys. Rev. B* **1976**, *13*, 5188–5192.

[154] Ludwig, J.; An, L.; Pattengale, B.; Kong, Q.; Zhang, X.; Xi, P.; Huang, J. Ultrafast Hole Trapping and Relaxation Dynamics in p-Type CuS Nanodisks. *J. Phys. Chem. Lett.* **2015**, *6*, 2671–2675.

[155] Giannuzzi, R.; De Donato, F.; De Trizio, L.; Monteduro, A. G.; Maruccio, G.; Scarfiello, R.; Qualtieri, A.; Manna, L. Tunable Near-Infrared Localized Surface Plasmon Resonance of F, In-Codoped CdO Nanocrystals. *ACS Appl. Mater. Interfaces.* **2019**, *11*, 39921–39929.

[156] Lee, S. A.; Link, S. Chemical Interface Damping of Surface Plasmon Resonances. *Acc. Chem. Res.* **2021**, *54*, 1950–1960.

[157] Scotognella, F.; Della Valle, G.; Srimath Kandada, A. R.; Dorfs, D.; Zavelani-Rossi, M.; Conforti, M.; Miszta, K.; Comin, A.; Korobchevskaya, K.; Lanzani, G.; Manna, L.; Tassone, F. Plasmon Dynamics in Colloidal $Cu_{2-x}Se$ Nanocrystals. *Nano Lett.* **2011**, *11*, 4711–4717.

[158] Robie, R. A.; Seal, R. R.; Hemingway, B. S. Heat capacity and entropy of bornite (Cu5FeS4) between 6 and 760 K and the thermodynamic properties of phases in the system Cu-Fe-S. *The Canadian Mineralogist* **1994**, *32*, 945–956.

[159] Gaspari, R.; Della Valle, G.; Ghosh, S.; Kriegel, I.; Scotognella, F.; Cavalli, A.; Manna, L. Quasi-Static Resonances in the Visible Spectrum from All-Dielectric Intermediate Band Semiconductor Nanocrystals. *Nano Lett.* **2017**, *17*, 7691–7695.

[160] Faucheaux, J. A.; Stanton, A. L. D.; Jain, P. K. Plasmon Resonances of Semiconductor Nanocrystals: Phys. Principles and New Opportunities. *J. Phys. Chem. Lett.* **2014**, *5*, 976–985.

[161] Jung, J.; Pedersen, T. G. Analysis of plasmonic properties of heavily doped semiconductors using full band structure calculations. *J. Appl. Phys.* **2013**, *113*, 114904.

[162] Schimpf, A. M.; Gunthardt, C. E.; Rinehart, J. D.; Mayer, J. M.; Gamelin, D. R. Controlling Carrier Densities in Photochemically Reduced Colloidal ZnO Nanocrystals: Size Dependence and Role of the Hole Quencher. *J. Am. Chem. Soc.* **2013**, *135*, 16569–16577.

[163] Valdez, C. N.; Braten, M.; Soria, A.; Gamelin, D. R.; Mayer, J. M. Effect of Protons on the Redox Chemistry of Colloidal Zinc Oxide Nanocrystals. *J. Am. Chem. Soc.* **2013**, *135*, 8492–8495.

[164] Carroll, G. M.; Schimpf, A. M.; Tsui, E. Y.; Gamelin, D. R. Redox Potentials of Colloidal n-Type ZnO Nanocrystals: Effects of Confinement, Electron Density, and Fermi-Level Pinning by Aldehyde Hydrogenation. *J. Am. Chem. Soc.* **2015**, *137*, 11163–11169.

[165] Lakhwani, G.; Roijmans, R. F. H.; Kronemeijer, A. J.; Gilot, J.; Janssen, R. A. J.; Meskers, S. C. J. Probing Charge Carrier Density in a Layer of Photodoped ZnO Nanoparticles by Spectroscopic Ellipsometry. *J. Phys. Chem. C* **2010**, *114*, 14804–14810.

[166] Rinehart, J. D.; Schimpf, A. M.; Weaver, A. L.; Cohn, A. W.; Gamelin, D. R. Photochemical Electronic Doping of Colloidal CdSe Nanocrystals. *J. Am. Chem. Soc.* **2013**, *135*, 18782–18785.

[167] Cohn, A. W.; Janßen, N.; Mayer, J. M.; Gamelin, D. R. Photocharging ZnO Nanocrystals: Picosecond Hole Capture, Electron Accumulation, and Auger Recombination. *J. Phys. Chem. C* **2012**, *116*, 20633–20642.

[168] Liu, Z.; Gong, S.; Wang, Y.; Chen, T.; Niu, Y.; Xu, Y. Recognition of the Enzymatically Active and Inhibitive Oxygenous Groups on WO3–x Quantum Dots by Chemical Deactivation and Density Functional Theory Calculations. *ACS applied bio materials* **2020**, *3*, 1459–1468.

[169] Mantella, V.; Ninova, S.; Saris, S.; Loiudice, A.; Aschauer, U.; Buonsanti, R. Synthesis and Size-Dependent Optical Properties of Intermediate Band Gap Cu3VS4 Nanocrystals. *Chem. Mater.* **2019**, *31*, 532–540.

[170] Hsu, S.-W.; Ngo, C.; Tao, A. R. Tunable and Directional Plasmonic Coupling within Semiconductor Nanodisk Assemblies. *Nano Lett.* **2014**, *14*, 2372–2380.

[171] Li, D.; Barreteau, C.; Castell, M. R.; Silly, F.; Smogunov, A. Out- versus in-plane magnetic anisotropy of free Fe and Co nanocrystals: Tight-binding and first-principles studies. *Phys. Rev. B* **2014**, *90*, 205409.

[172] M. Borgheresi; F. Di Benedetto; Andrea Caneschi; Giovanni Pratesi; Maurizio Romanelli; Lorenzo Sorace An EPR and SQUID magnetometry study of bornite. **2007**, *34*, 609–619.

[173] Giamarchi, T.; Rüegg, C.; Tchernyshyov, O. Bose–Einstein condensation in magnetic insulators. *Nat. Phys.* **2008**, *4*, 198–204.

[174] Dahlman, C. J.; Agrawal, A.; Staller, C. M.; Adair, J.; Milliron, D. J. Anisotropic Origins of Localized Surface Plasmon Resonance in n-Type Anatase TiO_2 Nanocrystals. *Chem. Mater.* **2019**, *31*, 502–511.

[175] Prandini, G.; Marrazzo, A.; Castelli, I. E.; Mounet, N.; Marzari, N. Precision and efficiency in solid-state pseudopotential calculations. *npj Computational Materials* **2018**, *4*, 72.

[176] Garrity, K. F.; Bennett, J. W.; Rabe, K. M.; Vanderbilt, D. Pseudopotentials for high-throughput DFT calculations. *Computational Materials Science* **2014**, *81*, 446–452.

[177] Kucukbenli, E.; Monni, M.; Adetunji, B. I.; Ge, X.; Adebayo, G. A.; Marzari, N.; de Gironcoli, S.; Corso, A. D. Projector augmented-wave and all-electron calculations across the periodic table: a comparison of structural and energetic properties. *arXiv:1404.3015 [cond-mat]* **2014**,

[178] Ando, K.; Munekata, H. Magneto-optical study of spin-carrier interactions in (In,Mn)As. *J. Magn. Magn. Mater.* **2004**, *272-276*, 2004–2005.

[179] Oak, H. N.; Baek, K. S.; Jo, Y. Superparamagnetic relaxation in Cu5FeS4. *Solid State Communications* **1996**, *100*, 467–470.

[180] Jagadeesh, M. S.; Nagarathna, H. M.; Montano, P. A.; Seehra, M. S. Magnetic and Mössbauer studies of phase transitions and mixed valences in bornite ($Cu_{4.5}Fe_{1.2}S_{4.7}$). *Phys. Rev. B* **1981**, *23*, 2350–2356.

[181] M.G. Townsend; M. G. Townsend; J.R. Gosselin; R.J. Tremblay; R. J. Tremblay; L. G. Ripley; D.W. Carson; W.B. Muir A magnetic and Mössbauer study of magnetic ordering and vacancy clustering in Cu5FeS4. *J. Phys. Chem. Solids* **1977**, *38*, 1153–1159.

[182] Paunović, N.; Popović, Z. V.; Dohčević-Mitrović, Z. D. Superparamagnetism in iron-doped CeO2-y nanocrystals. *J. Condens. Matter Phys.* **2012**, *24*, 456001.

[183] Sil, S.; Datta, J.; Das, M.; Jana, R.; Halder, S.; Biswas, A.; Sanyal, D.; Ray, P. P. Bias dependent conduction and relaxation mechanism study of Cu5FeS4 film and its significance in signal transport network. *J. Mater. Sci.: Materials in Electronics* **2018**, *29*, 5014–5024.

[184] Radovanovic, P. R.; Gamelin, D. R. Magnetic circular dichroism spectroscopy of CO2+:CdS diluted magnetic semiconductor quantum dots. Nanoscale Opt. and Applications. 2002; pp 51–61.

[185] Ando, K.; Saito, H.; Agarwal, K. C.; Debnath, M. C.; Zayets, V. Origin of the Anomalous Magnetic Circular Dichroism Spectral Shape in Ferromagnetic Ga1-xMnxAs: Impurity Bands inside the Band Gap. *Phys. Rev. Lett.* **2008**, *100*, 067204.

[186] Ando, K.; Takahashi, K.; Okuda, T.; Umehara, M. Magnetic circular dichroism of zinc-blende-phase MnTe. *Phys. Rev. B* **1992**, *46*, 12289–12297.

[187] Shiratsu, T.; Yao, H. Magnetic circular dichroism (MCD) in silver nanocubes with different sizes. *Chem. Phys. Lett.* **2018**, *706*, 607–612.

[188] Sheikholeslami, S.; Jun, Y.-w.; Jain, P. K.; Alivisatos, A. P. Coupling of Optical Resonances in a Compositionally Asymmetric Plasmonic Nanoparticle Dimer. *Nano Lett.* **2010**, *10*, 2655–2660.

[189] Luo, Y.; Dube, L.; Zhou, Y.; Zou, S.; Zhao, J. Plasmonic coupling in single flower-like gold nanoparticle assemblies. *Progress in Natural Science: Materials International* **2016**, *26*, 449–454.

[190] Neese, F.; Solomon, E. I. MCD C-Term Signs, Saturation Behavior, and Determination of Band Polarizations in Randomly Oriented Systems with Spin $S \geq {}^{1}/_{2}$. Applications to $S = {}^{1}/_{2}$ and $S = {}^{5}/_{2}$. *Inorg. Chem.* **1999**, *38*, 1847–1865.

[191] Kasap, S. O. *Principles of electronic materials and devices*, fourth edition ed.; McGraw-Hill, a business unit of The McGraw-Hill Companies, Inc: New York, NY, 2018.

[192] Goh, S. W.; Buckley, A. N.; Lamb, R. N.; Rosenberg, R. A.; Moran, D. The oxidation states of copper and iron in mineral sulfides, and the oxides formed on initial exposure of chalcopyrite and bornite to air. *Geochimica et Cosmochimica Acta* **2006**, *70*, 2210–2228.

[193] Schneider, S. S. B. Piepho and P. Schatz: Group Theory in Spectroscopy With Applications to Magnetic Circular Dichroism, aus der Reihe: Wiley Interscience Monographs in Chemical Physics, John Wiley + Sons, New York, Chichester, Brisbane, Toronto, Singapore 1983. 634 Seiten, Preis: £ 65.75. *Berichte der Bunsengesellschaft für physikalische Chemie* **1984**, *88*, 1023–1023.

[194] V. Pavan Kumar; Tristan Barbier; Pierric Lemoine; Bernard Raveau; Vivian Nassif; Emmanuel Guilmeau The crucial role of selenium for sulphur substitution in the structural transitions and thermoelectric properties of Cu5FeS4 bornite. *Dalton Transactions* **2017**, *46*, 2174–2183.

[195] Kikuchi, Y.; Tanaka, T. Strengthen of magnetic anisotropy of Au/Co/Au nanostructure by surface plasmon resonance. *Sci. Rep.* **2019**, *9*, 8630.

[196] Magana, D.; Perera, S. C.; Harter, A. G.; Dalal, N. S.; Strouse, G. F. Switching-on Superparamagnetism in Mn/CdSe Quantum Dots. *J. Am. Chem. Soc.* **2006**, *128*, 2931–2939.

[197] Kamra, A.; Ghosh, B.; Ghosh, T. K. Spin relaxation due to electron–electron magnetic interaction in high Lande g-factor semiconductors. *J. Appl. Phys.* **2010**, *108*, 054505.

[198] Herbert, P. J.; Window, P.; Ackerson, C. J.; Knappenberger, K. L. Low-Temperature Magnetism in Nanoscale Gold Revealed through Variable-Temperature Magnetic Circular Dichroism Spectroscopy. *J. Phys. Chem. Lett.* **2019**, *10*, 189–193.

[199] Seino, K.; Bechstedt, F. Effective density of states and carrier masses for Si/SiO_2 superlattices from first principles. *Semicond. Sci. Technol.* **2011**, *26*, 014024.

[200] Nicolau, Y. Solution deposition of thin solid compound films by a successive ionic-layer adsorption and reaction process. *Applications of Surface Science* **1985**, *22-23*, 1061–1074.

[201] Carnevale, D. J.; Shatruk, M.; Strouse, G. F. Ligand Passivated Core–Shell FePt@Co Nanomagnets Exhibiting Enhanced Energy Product. *Chem. Mater.* **2016**, *28*, 5480–5487.

[202] Yang, Y.; Ostrowski, D. P.; France, R. M.; Zhu, K.; Van De Lagemaat, J.; Luther, J. M.; Beard, M. C. Observation of a hot-phonon bottleneck in lead-iodide perovskites. *Nat. Photonics* **2016**, *10*, 53–59.

[203] Kang, J.; Sherman, Z. M.; Conrad, D. L.; Crory, H. S. N.; Dominguez, M. N.; Valenzuela, S. A.; Anslyn, E. V.; Truskett, T. M.; Milliron, D. J. Structural Control of Plasmon Resonance in Molecularly Linked Metal Oxide Nanocrystal Gel Assemblies. *ACS Nano* **2023**, *17*, 24218–24226.

[204] Chu, X.; Abelson, A.; Qian, C.; Igouchkine, O.; Field, E.; Ma, K.; Law, M.; Moule, A. J. Atomic Lattice Resolved Electron Tomography of a 3D Self-Assembled Mesocrystal. *Adv Funct Materials* **2023**, *33*, 2301026.

BIOGRAPHICAL SKETCH

Jason E. Kuszynski
DoD SMART Scholar
Florida State University
102 Varsity Way

Web: https://www.chem.fsu.edu/ strouse/
ORCID: 0000-0002-9458-6940
Tallahassee, FL 32304

Education & Training

Florida State University	Tallahassee, FL	Chemistry	Ph.D., 2024
Texas A&M University	College Station, TX	Chemistry	B.S., 2019

Research & Professional Experience

2023 – present	Army Space and Missile Defense Command, Redstone Arsenal
2019 – present	Strouse Research Group, Florida State University
2021 – 2022	Air Force Research Laboratory, Kirtland Air Force Base
2018 – 2019	Zhou Research Group, Texas A&M University
2017 – 2019	Gladysz Research Group, Texas A&M University
2016 – 2019	North Research Group, Texas A&M University
2018 – 2018	Modifiers R&D, Kaneka North America LLC.

Publications

Most closely related

1. **Kuszynski, J. E.**; Zhong, X.; McGill, S. A.; Dennis, A. M.; Strouse, G. F., Iron Intermediate Band Governs Relaxation Kinetics of Bornite Plasmonic Semiconductor Nanocrystals. *Submitted to ACS Mater. Lett.*

2. **Kuszynski, J. E.**; Fabiano, C. J.; Nguyen E. T.; Mao, K.; Ahuja, A. K.; Schaller, R. D.; Strouse, G. F., Plasmon-Induced Hot-Carrier Excited-State Dynamics in Plasmonic Semiconductor Nanocrystals. *J. Phys. Chem. C* **2023**, 127 (46), 22654-22661

3. **Kuszynski, J. E.**; Kays, J. C.; Conti, C. R. III; McGill, S. A.; Strouse, G. F.; Dennis, A. M., Effective Mass for Holes in Paramagnetic, Plasmonic Cu5FeS4 Semiconductor Nanocrystals. *J. Phys. Chem. C* **2022**, 126 (30), 12669-12679

Other significant publications

1. **Kuszynski, J. E.**; Zhong, X.; Shirato, N.; Wieghold, S.; Rose, V.; Dennis, A. M.; Strouse, G. F., Plasmon Carrier Density Correlates with Cu L-edge Intensity. *In progress*

2. Ortega, R.; **Kuszynski, J. E.**; Smith, R.; Bayles, A.; McGill, S. A.; Halas, N. J.; Schurko, R.; Strouse, G. F., Evidence of Fermi Level Carriers in Highly Faceted Plasmonic Cd_2SnO_4 Inverse Spinel Nanocrystals. *Submitted to Adv. Mater.*

3. Sullivan, C. M.; **Kuszynski, J. E.**; Kovalev, A.; Siegrist, T.; Schaller, R. D.; Strouse, G. F.; Nienhaus, L., Cool carriers: triplet diffusion dominates upconversion yield. *Nanoscale.* **2023**, 15 (46), 18832-18841

4. Sullivan, C. M.; Bieber, A. S.; Drozdick, H. K.; Moller, G.; **Kuszynski, J. E.**; VanOrman, Z. A.; Wieghold, S.; Strouse, G. F.; Nienhaus, L., Surface Doping Boosts Triplet Generation Yield in Perovskite-Sensitized Upconversion. *Adv. Opt. Mater.* **2022**, 11 (1) 2201921

5. Nguyen, E. T.; Bertini, I. A.; Ritz, A. J.; Lazenby, R. A.; Mao, K.; McBride, J. R.; Mattia, A. V.; **Kuszynski, J. E.**; Wenzel, S. F.; Bennett, S. D.; Strouse, G. F., A Single Source, Scalable Route for Direct Isolation of Earth-Abundant Nanometal Carbide Water-Splitting *Electrocatalysts. Inorg. Chem.* **2022**, 61 (35), 13836-13845

6. Xiao, Z.; Drake, H. F.; Day, G. S.; **Kuszynski, J. E.**; Lin, H.; Xie, H.; Cai, P.; Ryder, M. R.; Zhou, H.-C., Photoinduced reversible phase transition in a phenothiazine-based metal-organic framework. *Cell Rep. Phys. Sci.* **2022**, 3 (10), 101074

7. Kays, J. C.; Conti, C. R. III; Margaronis, A.; **Kuszynski, J. E.**; Strouse, G. F.; Dennis, A. M., Controlled synthesis and exploration of Cu_xFeS_4 bornite nanocrystals. *Chem. Mater.* **2021**, 33 (18), 7408-7416

Synergistic Activities

1. Significant written and intellectual contributions for NSF DMR grant submission in 2024.

2. Primary author of accepted research proposals:

   - Center for Nanoscale Materials, Argonne National Laboratory 2022 – 2024
     - Proposal 83288: "Magneto-optical Hot Carrier Effects in Plasmonic Semiconductor Nanocrystals"
     - Proposal 81720: "Understanding the Role of W(V) versus Oxygen Vacancies on Hot Carrier Generation and Relaxation in Plasmonic WO_{3-x} Semiconductor Nanocrystals"

- Proposal 79606: "Quantification of Oxygen Vacancies and Hot Carrier Effects in Plasmonic Semiconductor Nanocrystals"

- Advanced Photon Source, Argonne National Laboratory 2022 – 2023
  - Proposals 81623, 78200, & 78191: "Optimizing Electronic Transport Properties of Cu_xFeS_4 (x = 3,4,5,6,7) Plasmonic Semiconductor Materials"
- Spallation Neutron Source, Oak Ridge National Laboratory 2022 – 2023
  - Proposal 29535: "Correlating Structural Changes to Magneto-optical Behavior of Cu_xFeS_4 (x = 3,4,5,6,7) Plasmonic Semiconductor Nanocrystals"

3. Mentoring undergraduate students:

- Mr. Jonathan Rider, Chemical Engineering Major 2023 – Present
  - Taught laboratory skills and techniques, leading to the development of an independent project
  - Training resulted in preparation of over 20 samples with characterization of UV-vis-NIR and pXRD
  - ACS Spring 2024 Poster Presentation: In progress
- Mr. Alex Trbovic, Computer Science Major 2022 – Present
  - Advising understanding of optical sciences with computer science software development
  - Coaching LabVIEW code writing with repeated walkthroughs and organization white-board meetings
  - Poster Presentation: Design and Implementation of LabVIEW-based Spectroscopy Software on an Ocean Optics Spectrometer
- Ms. Anoushka Ahuja, Computer Science Major 2021 – 2022
  - Trained rigorously in glovebox and microwave reactor synthesis procedure and safety
  - Mentored presentation skills in preparation for in-person symposia and academic presentations
  - Poster Presentation: Exploration of Plasmonic WO_{3-x} Nanocrystals Through Various Microwave Methods
- Mr. Jason King, Chemical Engineering Major 2020 – 2021
  - Taught hands-on techniques in electrical wiring and optical tabletop development
  - Supervised academic writing sessions towards the development of independent publication
  - Poster Presentation: Application of Magnetic Circular Dichroism and Data Processing